ALMA MATER STUDIORUM

UNIVERSITY OF BOLOGNA

PhD in Information Technologies

ING-INF/01

Design and Fabrication of MOMS-Based Ultrasonic Probes for Minimally Invasive Endoscopic Applications

by

Luca BELSITO

Coordinator:

Prof. Ing. Claudio FIEGNA

Supervisor:

Prof. Ing. Guido MASETTI

As. Supervisor:

Ing. Alberto RONCAGLIA

Academic year 2010-11

Contents

4.   Ultrasounds Emission and Detection by Highly Miniaturized MOMS Devices Self-Standing on Optical Fiber

5.   Conclusion

1

Use of Laser Sources for the Emission and Detection of Ultrasounds

1.1 Introduction

Ultrasounds are widely used for diagnostic and therapeutic purposes in many fields of modern medicine. In low power form, for instance, they have been successfully employed in diagnostic imaging for many years, assuring excellent temporal resolution thanks to their low propagation velocity. Furthermore, high power ultrasonic waves can be used to induce the controlled heating of tissues for therapeutic aims such as eradicating microorganisms and curing rheumatisms. However, the importance of ultrasonic waves is not constrained to the medical field, since ultrasounds are also used in many other applications, such as high frequency vibration control in industrial plants and Non Destructive Evaluation (NDE) of materials and structures [1].

The use of ultrasonic systems has considerably increased in the last decades thanks to the sensible improvements achieved in their performances and disposability, made possible by technological advancements, and to the numerous novel applications investigated in scientific research. As far as ultrasound imaging is concerned, the frequencies exploited in currently used systems are generally limited to 10 MHz. This limitation essentially derives from two problems.

The first one depends on the technology used to generate/detect ultrasonic waves in such systems, which is normally based on PZT materials like lead titanate zirconate for emission and detection or, alternatively, piezoelectric polymers like PVDF (Poly-Vinyl-DiFluoride) for detection only. Since, owing to their mechanical resonant nature, piezoelectric devices show a peaked emission in frequency, they must be miniaturized in order to be operated at high

frequencies, and this leads to a remarkable decrease in sensitivity. This limitation cannot be fully overcome with design optimization of the transducers since it is closely related to the physical principle exploited in piezoelectric transduction. As a consequence of that, it is extremely difficult to fabricate conventional ultrasound arrays operating at high frequencies and characterized by good sensitivity, even if examples of piezoelectric devices operating at frequencies as high as 45 MHz have been reported in the literature [2]. Moreover, the peaked emission in frequency of piezoelectric transducers, even when designed for high-frequencies, makes them essentially unsuited for broadband operation [3], which is considered important in many cases [4].

The second problem is related to the strong attenuation of high-frequency ultrasound waves in living tissues, which leads to a decreasing penetration depth with increasing frequencies of operation and is typically limited to few centimetres at frequency levels as high as 30 MHz. This effect represents a severe limitation to the applicability of conventional ultrasonic arrays at high frequencies to the imaging of living tissues in vivo, since the normally used setup consists of an array of ultrasonic transducers, used for both emission and detection of the ultrasound waves, which is placed on the external surface of the living organism under examination. Using this array externally, even though in contact with skin, demands to have a sufficient penetration of ultrasound towards the interior of the body in order to scan the desired target. While this system is perfectly appropriate for low frequency ultrasounds, it does not fit to high-frequency waves due to their limited penetration in tissues.

Despite these fundamental limitations, the in vivo imaging performed with high frequency ultrasounds has been the focus of an intense research work during the last few years, and several possible applications have been proposed, particularly in the field of tissue analysis, such as intravascular imaging [5], analysis of cancer tissues [6], corneal imaging [7], investigation of cancer evolution in small animal models [8], photoacoustic tomography of vasculature [9]. In all these applications, the use of high-frequency ultrasonic waves for scanning has given promising results basically for their capability of achieving higher spatial resolution due to their smaller wavelengths with respect to those of conventional systems. Moreover, the more pronounced interaction of high-frequency ultrasonic waves with tissues due to the strong attenuation experimented by the waves during propagation has been proposed as a mean to investigate biological properties that may be of concern for clinical aims (such as recognition of cancer formations by their high-frequency ultrasonic signature

as proposed in [10] that might enable a "virtual biopsy" procedure through ultrasound imaging). It must be said, however, that this fascinating possibility has not yet been demonstrated in practice and no experimental data supporting the validity of this method seem to be available in the scientific literature, to date.

Another application connected to the interaction of ultrasonic waves with living tissues which is being intensely investigated at present is photoacoustic imaging (see for instance [9]). In this technique, the tissues are directly excited by a light pulse (usually implemented with a medium power laser) and the ultrasonic waves emitted by the thermoelastic expansion of the biological material hit by the light are detected by an ultrasonic detector array. In this way, the imaging is sensitive to the properties of tissues, not only related to ultrasound propagation but also to light absorption and thermoelastic emission, and this opens a door to novel possibilities for minimally invasive diagnostic techniques. In this respect, it is worth noting that photoacoustic imaging (which is not yet a clinical technique but is considered very promising for future diagnostic applications) inherently requires a high-frequency ultrasound detection system to fully exploit its potential, since ultrasound waves emitted by thermoelastic expansion from short laser pulses (typically in the nanosecond regime) naturally present widebands extended up to several tens of MHz. However, photoacoustic emission is directly performed by optical excitation of tissues in this technique and consequently no ultrasonic source is needed.

Due to the problem of attenuation of high-frequency ultrasounds in biological tissues, all the applications mentioned above have been limited to cases in which the reduced penetration of high-frequency waves in biological tissues is not important (like analysis of superficial organs such as skin and eye or ultrasound imaging of small animals in which the reduced size of the living organism under examination helps overcome the problem) or performed with endoscopic tools (but in this case the trade-off between sensitivity and band in piezoelectric transducers proved to be extremely challenging, see for instance [2]).

Since, in principle, a high performance ultrasound imaging system able to operate on a broad spectral range (up to several tens on MHz) is required in high-frequency ultrasound imaging (of both purely ultrasonic and photoacoustic type), piezoelectric transduction is generally avoided, and optoacoustic generation and/or detection of ultrasounds is preferred in order to avoid the fundamental physical limitations concerning the sensitivity/frequency trade-off mentioned earlier.

In particular, the thermoelastic generation mechanism is generally exploited for broadband emission of ultrasounds, using thin absorbing films excited by pulsed laser beams in the nanosecond regime. In this way, the sudden heating of the film and its consequent thermal expansion produces waves whose spectrum is typically fairly flat up to frequencies around 50 MHz or even more, depending on the features of the laser pulse and the characteristics of the absorbing film. The research work related to this field, initially focused on thin metal films such as chrome as laser absorbers [11], has recently evolved towards the use of heavily absorbing non-metallic films like graphite/epoxy mixtures [12], PDMS with the addition of carbon black [13] or gold nanoparticles [14], achieving ultrasound emission on bands extended beyond 60 MHz and much better generation efficiency than metallic films, as will be discussed in greater detail in the following section.

Considering the problem of detection, the most promising devices investigated so far for broadband ultrasound waves are polymer Fabry-Perot, that can provide a quite flat spectral response over a band extended from low frequencies up to 50 MHz and beyond, and high sensitivity [15]. Quite interestingly, an example of integrated fabrication of a photoacoustic emitter and detector obtained by overlapping a carbon black added PDMS layer for ultrasound emission on a SU-8 Fabry-Perot has been recently reported in [16].

The main limitations of the technologies developed so far for photoacoustic ultrasound generation and detection is certainly the lack of miniaturization, particularly concerning arrays of detectors or emitters. Actually, both emitter and detector arrays have been demonstrated using the solutions described above, but only on bulk substrates (like fused silica wafers) and using free-propagation lasers to operate the array [14], a solution necessarily constrained to imaging applications in which the optoacoustic ultrasonic array can be operated from the exterior of the living organism in vivo, as discussed before.

In this respect, miniaturization would be extremely valuable for high-frequency ultrasound imaging, since the strong attenuation of acoustic waves at these frequencies could be in principle overcome by the use of a miniaturized broadband imaging system suited to minimally invasive endoscopic operation.

Since, as widely demonstrated by recently reported results in the scientific literature, the intrinsic limitations of piezoelectric ultrasound transducers can be fully overcome by exploiting optoacoustic ultrasound generation and detection, this technological advancement could be achieved by exploiting known physical principles implemented with

an innovative fabrication technology suitable for realizing the ultrasound generation and detection system at the micro scale.

This subject is closely related to the main objective of the present thesis, in which the development a novel Micro-Opto-Mechanical (MOMS) technology for the fabrication of highly miniaturized fiber optic transducers suitable for wideband ultrasonic generation/detection and potentially usable in arrays will be described.

In the following sections of this introduction, the state of the art of optoacoustic methods for ultrasound generation and detection considered for application in the proposed technology will be briefly reviewed, starting from thermoelastic generation.

1.2 Optoacoustic Generation

The thermo elastic generation mechanism has been widely studied for ultrasound generation in solids, liquids and gases [17]. Ultrasound emission by thermoelastic expansion is based on the conversion of optical power into heat that takes place when a pulsed laser beam hits the surface of an absorbing material, leading to rapid and localized temperature increase. This results in a sudden thermal expansion of the heated part of the material, which generates ultrasound waves. If the incoming optical power is not exceedingly high, neither melting nor ablation of the material takes place and a pure thermoelastic generation is obtained.

The emission of acoustic waves by means of pulsed laser beams was demonstrated for the first time by White [18] in 1963. Since then, the interest in generation of ultrasonic waves by laser irradiation of a solid increased steadily. In the early eighties, Rose [19] gave a fundamental contribution to the understanding of the phenomenon by deriving a closed-form mathematical model of the physics involved in a point-source representation of the opto-acoustic generation. In the cited paper, in particular, the author demonstrated that laser generated ultrasounds can be effectively approximated by considering a *surface center of expansion* equivalent to the shear stress dipole source model proposed by Scruby [20], but rigorously derived by means of a Green's function formalism. Subsequently, more detailed investigations were undertaken, and increasingly accurate mathematical modeling was carried out in order to investigate the opto-acoustic generation mechanism in deeper detail.

Experimental research in this field initially focused on thin metal films such as chrome as laser absorbers [11], which were functional but showed poor generation efficiency. More recently, new achievements concerning the use of heavily absorbing non-metallic films have demonstrated that much better emission efficiency is possible using materials different than thin metals, with band width extended beyond 60 MHz and acoustic pressures up to 800 kPa at a distance of 10 mm from the generating film [21]. Many of the various materials employed as non-metallic absorbing films in these experiments were carbon based, often composed by graphite or amorphous carbon particles embedded within a polymeric matrix, like graphite/epoxy mixtures [12] or PDMS with the addition of carbon black [13]. In [14], instead of carbon, gold nanoparticles mixed with a polymeric material have been used for optoacoustic emission, using the proper particle size to maximize the optical power absorption in the nanostructured film. However, pure graphite films obtained by sputtering from a bulk target have also been tested as thermoelastic generators, providing good ultrasonic emission when excited with a nanosecond laser pulse [12].

Laser-generated ultrasounds have also been successfully applied to not destructive mechanical characterization of materials and structures in which, differently than the conventional piezoelectric transducers, they can be used without any mechanical contact with the inspected surface allowing for higher speed in the analysis.

In all these applications, the efficiency of the opto-acoustic conversion process is important. Such efficiency depends on several parameters, such as the optical absorption and thermal expansion coefficients, the thermal capacity of the absorbing layer, and the mechanical and thermal boundary conditions imposed on it.
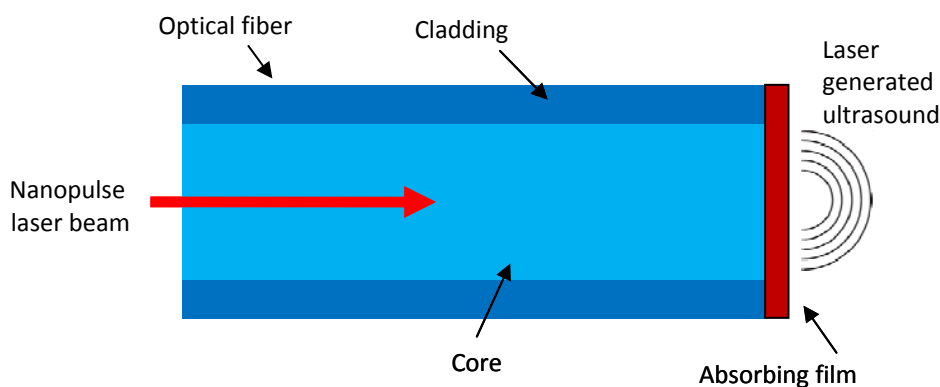
Fig. 1.1. Optoacoustic emitter on optical fiber

In order to obtain an efficient ultrasonic generation, a possible solution can be guiding the laser beam up to the absorbing material through an optical fiber, as shown in Fig. 1.1. This method has been similarly proposed for instance in [22].

As may be verified by solving the heat diffusion equation to calculate the temperature distribution in the domain of interest and using the Green-Naghdi relation to compute the displacement, the bandwidth of the generated signal is limited by the laser pulse duration and by its power [12]. In particular, it is interesting to observe that, according to theoretical calculations and experimental results, the bandwidth increases when a shorter laser pulse is used. Moreover, the amplitude of the ultrasonic wave and its bandwidth also depend on the thickness of the absorbing layer [21].

The thermoelastic effect is, actually, mainly concentrated immediately below the surface of the absorbing film exposed to the laser pulse because of the exponential power reduction that takes place while the electromagnetic radiation propagates across the absorbing film. As a consequence of that, when highly absorbing materials like graphite are employed, the thermoelastic effect is limited to a thickness of few hundreds of nanometers below the surface. As a consequence of that, the remaining part of the film does not contribute to the optoacoustic generation giving rise to an undesired attenuation of the acoustic waves and therefore to a decrease in conversion efficiency. This detrimental effect could be virtually eliminated by developing a fabrication technology enabling the deposition of absorbing films with high thickness control. It must be said, however, that, on the other hand, when the film thickness becomes comparable to the optical penetration length, part of the electromagnetic energy is transmitted beyond the layer and does not take part in the optoacoustic conversion process, so the thickness must be carefully chosen in order to reach the best trade-off between these two effects.

Besides the laser pulse dynamics and the film properties, the laser power is quite obviously important in determining the amplitude of the generated ultrasonic waves, since a straightforward relation between laser power and thermoelastically generated ultrasound amplitude exists, in principle. However, the film ablation threshold has to be taken into account as an upper limit in order to avoid damaging the device.

1.3   Optoacoustic Detection

The conventional method adopted in ultrasound detection is based on the piezoelectric effect, according to which an electric charge is produced when a mechanical stress generated by the incoming ultrasound wave is applied on a piezoelectric element. The piezoelectric technology can be used in general for both emission and detection of ultrasounds in a rather similar way, often using the same array of transducers in sensing or actuation mode, even if the actuation efficiency is closely related to the properties of the material used (e. g. soft piezoelectric polymers like PVDF are quite efficient for sensing but not suitable for actuation due to their limited mechanical stiffness, while inorganic PZT materials are generally used for both purposes with good performances).

As discussed before, one of the main limitations of piezoelectric technology for ultrasounds is the marked sensitivity (or emission efficiency) reduction with decreasing element areas and thickness, which prevents from easy fabrication of high-frequency transducers with good performances. Furthermore, the integration of many piezoelectric detectors needed for the fabrication of arrays is very complex because it requires a pair of connections for each transducers and complex readout electronics that should be placed close to the sensing pixel for signal preamplification, which makes the system rather sophisticated and in some cases not easy to miniaturize. Moreover, the treatment of electric signals coming from closely packed, individually addressed pixels can lead to crosstalk problems (mainly coming from capacitive coupling between adjacent connections) that need to be carefully addressed in designing the systems, and may limit the maximum number of detectors that can be integrated on the array. As far as biological applications of ultrasounds are concerned, the acoustic impedance matching of the transducer with water is important because of its preponderant presence in almost all biological tissues. In this respect, piezoelectric ceramics are not favoured because they show a poor acoustic impedance matching to liquids due to their high stiffness, resulting in a non uniform frequency response. On the contrary, PVDF-based transducers feature a low acoustic impedance ($\cong$4 Mrayl), assuring a better acoustic matching and giving a more uniform frequency response, but they present a lower electromechanical coupling than piezoceramics devices [23].

The research concerning the development of technological solutions for optical-fiber ultrasound sensors has considerably increased in the last decades. Among the various possible alternatives, extrinsic Fabry-Perot interferometric detectors are probably the most promising technology proposed to date for wideband ultrasound detection [24] [15] providing adequate signal-to-noise ratio, operation band extended from low frequencies to beyond 50 MHz and high miniaturization levels, but only on an individual pixel at the present state of the art. The operating principle of the fiber-optic extrinsic Fabry-Perot detector is the following. A continuous laser beam is guided by an optical fiber up to an interferometric cavity, constituted by a sensitive material (generally a polymer) and two metallizations (Fig. 1.2).
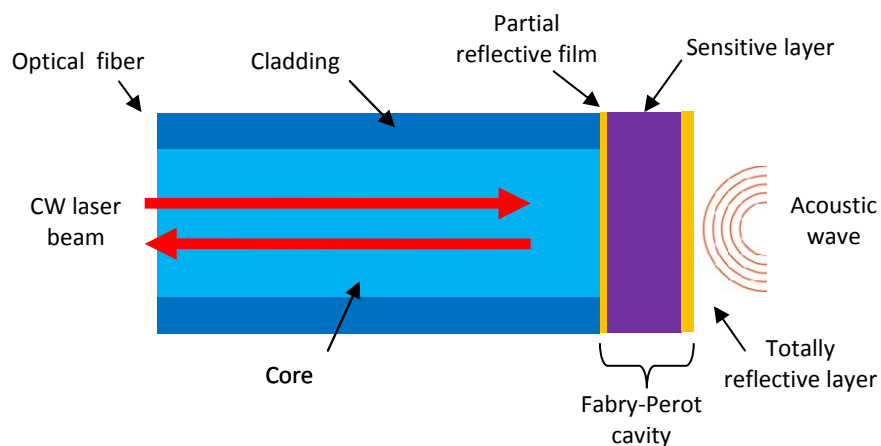
Fig. 1.2. Extrinsic Fabry-Perot ultrasound detector on optical fiber

When an acoustic wave hits the interferometer, the thickness of the sensitive film changes, resulting in an alteration of optical interference conditions within the cavity defined by the space between the two metallic mirrors. As a consequence of that, the optical power reflected by the cavity, which depends, in general, on the optical properties of the different thin layers involved, and in particular on the thickness of the polymeric spacer located between the mirrors, is modulated by the incoming pressure wave. In this way, the amplitude spectrum of the ultrasound wave is transferred to the reflected light transmitted in backward direction and can be measured at the opposite end of the fiber using an optoelectronic detector, such as a photodiode.

An adequate choice of the material used as a sensitive film in the interferometer is of primary importance for optimization of the detection performance. In particular, an ideal

material should be completely transparent to the operation wavelength of the laser and should present acoustic impedance close to the one of the material under inspection. In this way, the electromagnetic radiation would not attenuate during its propagation within the cavity, while the acoustic wave would be fully transmitted to the Fabry-Perot detector from the inspected medium.

Thanks to their low Young's modulus (typically 0.1-5 GPa), polymers are perfect candidates for this sensing scheme, assuring high detection sensitivity due to their low stiffness that allows for a significant variation of the layer thickness even in the presence of weak acoustic waves. Furthermore, many polymers have acoustic impedance close to that of water, resulting in uniform response if the sensor is used for tissue characterization. Moreover the employment of single-mode optical fibers for delivering the light limits the active area to the few square microns occupied by the core diameter within the fiber cross section and, consequently, high spatial resolution and low directional sensitivity can be reached.

A truly miniaturized fiber-optic device has been already reported [25], but with a single pixel, and consequently not usable for imaging. In this respect, miniaturization would be extremely valuable particularly if applied to high-frequency ultrasound detector arrays, potentially usable for minimally invasive endoscopic imaging of both photoacoustic and ultrasonic types in medical applications.

1.4 MOMS-Based Ultrasonic Transducers

In this thesis, the development of a MOMS technology suited to fabricate wideband ultrasound generators and detectors with high miniaturization level will be described. The basic structure chosen for the MOMS opto-acoustic ultrasonic emitters and receivers and their operating principles are schematically represented in Fig. 1.3.

In the emitter, the pulsed laser beam generates ultrasound waves by thermoelastic effect through the local heating of a carbon layer deposited on the silicon frame represented in the figure. This carbon film is fabricated by pyrolysis of a photoresist layer, providing the possibility to obtain the desired pattern for the emitters before the thermal treatment using a plain lithographic process. In this way, since the photoresist layer is deposited through spinning, a very good thickness control is possible, which represents an important variable in the optoacoustic generation process, as discussed earlier.
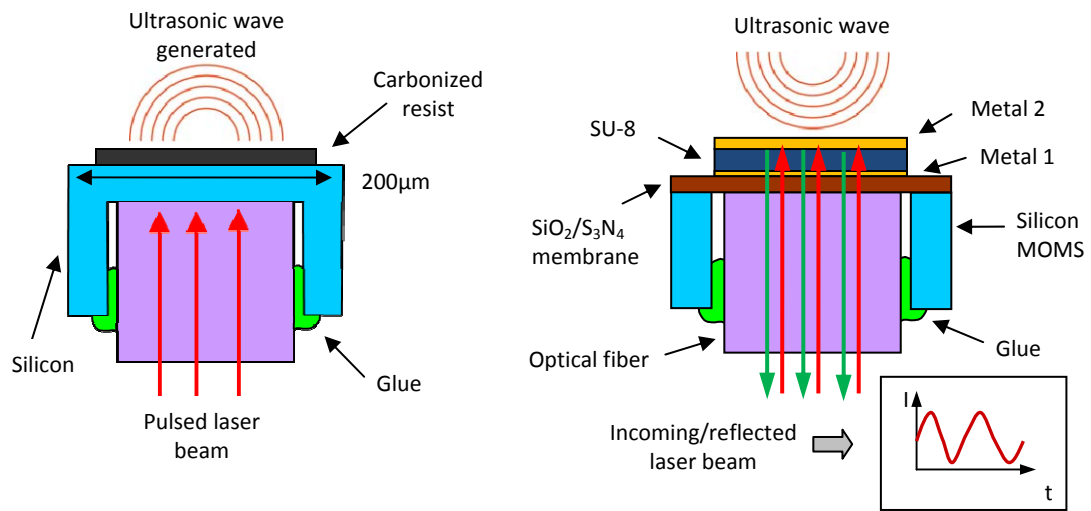
Fig. 1.3. Design and operating principle of the MOMS fiber-optic ultrasonic source (left) and detector (right)

In the MOMS detector, instead, a polymer interferometer is realized on a similar micromachined silicon frame, and used to modulate the reflected intensity of a continuous laser beam by interference effects as a function of the thickness of a SU-8 photoresist spacer (a low stiffness MEMS material [26] that can be geometrically patterned by lithography as pyrolytic carbon in the emitters).

As may be inferred from Fig. 1.3, both devices exploit silicon micromachined structures in order to enable the placement of the fibers close to the optical layers used for ultrasound generation and detection. A similar silicon microstructure is used in the two cases, which, once fixed to the fiber tip, permits to obtain freestanding, highly miniaturized devices that can be potentially used as ultrasound probes in a broad range of applications.

The adoption of silicon as a structural material in the proposed technology is strategic because it permits to take advantage of high performance micromachining techniques available at the present state of the art (Deep Reactive Ion Etching – DRIE in particular [27]) and is fully compatible with the use of lasers operating at wavelengths above 1 μm, since silicon is transparent in this infrared range. In addition, the use of lithographic techniques for the patterning of the optically active layers, performed on planar substrates, assures micrometric control of the layout geometry, while the high aspect ratio provided by DRIE

micromachining is ideal for the fabrication of highly miniaturized probes like those represented in Fig. 1.3.

In the following chapters, the development of fiber-optic ultrasonic probes constituted by detector and emitter arrays integrated on the same cylindrical micromachined support with minimum diameter smaller than 300 μm, will be illustrated. As a result of the miniaturization levels obtained with the novel fabrication technology presented, the ultrasonic probes demonstrated within this thesis may be suitable for minimally invasive endoscopic applications like the one depicted in Fig. 1.4, in which the fiber-optic ultrasonic emitters and detectors might be inserted in a thin syringe needle or in a catheter.
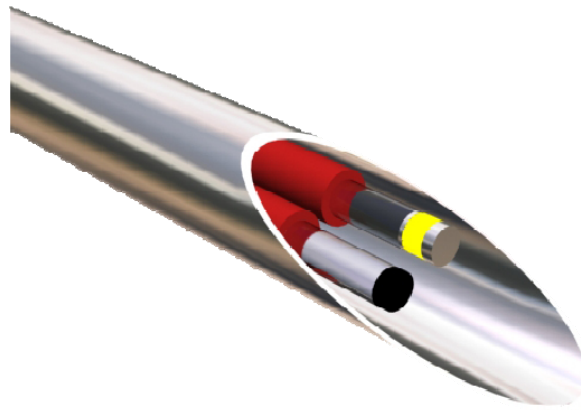
Fig. 1.4 Possible use of fiber-optic acoustic probes within a syringe needle

The description of the research activity carried out in order to reach the technical objectives described above will be organized as follows.

In chapter 2 the development of wideband ultrasonic emitters based on patterned carbon layers obtained by carbonization of photoresist on micromachined silicon structures obtained on a silicon chip will be illustrated. In chapter 3, a similar research will be described concerning polymeric Fabry-Perot detectors realized with patterned SU-8 on silicon micromachined structures obtained at the die level, while chapter 4 will be devoted to the integration of the two fabrication processes on the same substrate introducing proper modifications in the flow in order to obtain freestanding devices on optical fiber.

Finally, in chapter 5, some conclusions and possible future developments of the research work presented will be outlined.

Bibliography

[1] C.B. Scruby and L.E. Drain , *Laser Ultrasonics: Techniques and Applications*, 1990.

[2] K. A. Snook, C.-H. Hu, T. R. Shrout, and and K. K. Shung, "High-Frequency Ultrasound Annular-Array Imaging. Part I: Array Design and Fabrication", *IEEE Transactions on Ultrasonics, Ferroelectrics, and Frequency Control*, vol. 53, no. 2, pp. 300-308, 2006.

[3] H. Lamela, D. Gallego, and Oraevsky, "Optoacoustic imaging using fiber-optic interferometric sensors", *Optics Letters*, vol. 34, no. 23, 2009.

[4] E. Z. Zhang, J. G. Laufer, R.B. Pedley, and P. C. Beard, "In vivo high-resolution 3D photoacoustic imaging of superficial vascular anatomy", *Physics in Medicine and Biology*, vol. 54, no. 4, 2009.

[5] Y. Haga, M. Fujita, K. Nakamura, C. J. Kim, and M. Esashi, "Batch fabrication of intravascular forward-looking ultrasonic probe", *Sensors and Actuators A: Physical*, vol. 104, no. 1, pp. 40-43, 2003.

[6] J. Mamou, A. Coron, M. Hata, J. Machi, et al., "High-Frequency Quantitative Ultrasound Imaging of Cancerous Lymph Nodes", *Japanese Journal of Applied Physics*, vol. 48, 2009.

[7] A. Denoyer, F. Ossant, B. Arbeille, F. Fetissof, et al., "Very-high-frequency ultrasound corneal imaging as a new tool for early diagnosis of ocular surface toxicity in rabbits treated with a preserved glaucoma drug," *Ophthalmic Res.*, vol. 40, no. 6, pp. 298–308, 2008.

[8] K. C. Graham, L. A. Wirtzfeld, L. T. MacKenzie, C. O. Postenka, et al., "Three-dimensional High-Frequency Ultrasound Imaging for Longitudinal Evaluation of Liver Metastases in Preclinical Models", *Cancer Research*, vol. 65, pp. 5231-5237, 2005.

[9] S. Hu and L. V. Wang, "Photoacoustic imaging and characterization of the microvasculature", *Journal of Biomedical Optics*, vol. 15, no. 1, 2010.

[10] A. Acquafresca, E. Biagi, L. Masotti, and D. Menichelli, "Toward virtual biopsy through an all fiber optic ultrasonic miniaturized transducer: a proposal", *IEEE Transactions on Ultrasonics, Ferroelectrics, and Frequency Control*, vol. 50, no. 10, pp. 1325-1335, 2003.

[11] E. Biagi, M. Brenci, S. Fontani, L. Masotti, and M. Pieraccini, "Photoacoustic Generation: Optical Fiber Ultrasonic Sources for Non Destructive Evaluation and Clinical Diagnosis", *Optica Review* , vol. 4, no. 4, pp. 481-483, 1997.

[12] E. Biagi, F. Margheri, and D. Menichelli, "Efficient Laser-Ultrasound Generation by Using Heavily Absorbing Films as Targets", *IEEE Transactions on Ultrasonics, Ferroelectrics, and Frequency Control*, vol. 48, no. 6, pp. 1669-1680, 2001.

[13] T. Buma, M. Spisar, and M. O'Donnell, "High-frequency ultrasound array element using thermoelastic expansion in an elastomeric film", *Applied Physics Letters*, vol. 79, no. 4, 2001.

[14] Y. Hou, J.-S. Kim, S. Ashkenazi, M. O'Donnell, and L. J. Guo, "Optical generation of high frequency ultrasound using two-dimensional gold nanostructure", *Applied Physics Letters*, vol. 89, no. 9, 2006.

[15] Y. Hou, S. Huang, S. Ashkenazi, R. Witte, and M. O'Donnell, "Thin polymer etalon arrays for high-resolution photoacoustic imaging", *Journal of Biomedical Optics*, vol. 13, no. 6, 2008.

[16] Y. Hou, S. Ashkenazi, S. Huang, and M. O'Donnell, "An integrated optoacoustic transducer combining etalon and black PDMS structures", *IEEE Transactions on Ultrasonics, Ferroelectrics, and Frequency Control*, vol. 55, no. 12, pp. 2719 -2725, 2008.

[17] D.A. Hutchins, "Ultrasonic generation by pulsed lasers", in *Physical Acoustics, Vol XVIII*, Academic Press New York, Ed.: W.P. Mason and R.N. Thurston, pp. 21-123, 1988

[18] R.M. White, "Elastic Wave Generation by Electron Bombardment or Electromagnetic Wave Absorption", *Journal of Applied Physics*, vol. 34, 1963.

[19] L.R.F. Rose, "Point-source representation for laser-generated ultrasound", *J. Acoust. Soc. Am.*, vol. 75, no. 3, pp. 723-732, 1984.

[20] C.B. Scruby, R.J. Dewhurst, D.A. Hutchins, and S.B. Palmer, "Quantitative studies of thermally generated elastic waves in laser irradiated metals", *J. Appl. Phys.*, vol. 51, no. 12, pp. 6210-6216, 1980.

[21] Y. Hou, S. Ashkenazi, S. Huang, and M. O'Donnell, "Improvements in optical generation of high-frequency ultrasound," *IEEE Transactions on Ultrasonics, Ferroelectrics, and Frequency Control*, vol. 54, no. 3, pp. 682-686, 2007.

[22] R.J. von Gutfeld, "Thermoelastic generation of elastic waves for non-destructive testing and medical diagnostics", *Ultrasonics*, vol. 18, no. 4, pp. 175-181, 1980.

[23] F. S. Foster, K. A. Harasiewicz, and M. D. Sherar, "A history of medical and biological imaging with polyvinylidene fluoride (PVDF) transducers", *IEEE Transactions on Ultrasonics, Ferroelectrics, and Frequency Control*, vol. 47, no. 6, pp. 1363-1371, 2000.

[24] P.C. Beard, F. Perennes, and T.N. Mills, "Transduction mechanisms of the Fabry-Perot polymer film sensing concept for wideband ultrasound detection", *IEEE Transactions on Ultrasonics, Ferroelectrics and Frequency Control,* vol. 46, no. 6, pp. 1575-1582, 1999.

[25] P. Morris, A. Hurrell, A. Shaw, E. Zhang, and P. Beard, "A Fabry–Pérot fiber-optic ultrasonic hydrophone for the simultaneous measurement of temperature and acoustic pressure", *J. Acoust. Soc. Am.*, vol. 125, no. 6, pp. 3611-3622, 2009.

[26] S. Wang, P. Campistron, J. Carlier, D. Callens-Debavelaere, et al., "SU-8-based nanocomposites for acoustical matching layer", *IEEE Transactions on Ultrasonics, Ferroelectrics, and Frequency Control*, vol. 56, no. 7, pp. 1483-1489, 2009.

[27] H. V. Jansen, M. J. de Boer, S. Unnikrishnan, M. C. Louwerse, and M. C. Elwenspoek, "Black silicon method X: a review on high speed and selective plasma etching of silicon with profile control: an in-depth comparison between Bosch and cryostat DRIE processes as a roadmap to next generation equipment", *Journal of Micromechanics and Microengineering*, vol. 19, no. 3, 2009.

[28] P.A. Fomitchov, A. K. Kromine, and S. Krishnaswamy, "Photoacoustic Probes for Nondestructive Testing and Biomedical Applications", *Applied Optics*, vol. 41, no. 22, pp. 4451-4459 , 2002.

2 *Optoacoustic Generation of Ultrasounds: Design and Fabrication of MOMS-Based Emitters*

2.1 Introduction

Generation and detection of high-frequency ultrasounds is considered a valuable mean for many applications. Initially investigated for Non Destructive Evaluation (NDE) of materials, using pulsed laser light for straightforward generation of wideband ultrasound waves in bulk structures [1], photoacoustic ultrasound generation has recently been considered as a possible principle to realize broadband ultrasonic emission in use in different fields, with potential applicability to biomedical imaging [2]. Since, actually, spatial resolution in ultrasound imaging depends on wavelength, the use of high-frequency ultrasound waves (above 10 MHz) has been studied in recent years for several possible medical applications [3] [4]. The main issues involved in the design and fabrication of the optoacoustic ultrasonic sources will be analyzed in this section. After a short description of the thermoelastic effect, the fabrication process adopted for the MOMS based emitters will be discussed, focusing on the advantages of the developed technology and pointing out the high miniaturization enabled. Different models for the optical characterization of thin films will be introduced to determine the absorption properties of the carbon layers used as thermoelastic emitters and calculate the temperature profile within the layers during operation. Once described the fabrication of the devices, their functional characterization will be presented through the measure of a generated acoustic field performed by means of an experimental setup provided by the University of Florence.

The thermoelastic ultrasonic sources, realized by silicon micromachining, are depicted in Fig. 2.1. A carbon film with high optical absorption is deposited and patterned on the MOMS upper surface and an optical fiber is used for guiding the laser radiation up to the device. In

this way, thermo-elastic ultrasound generation takes place when the laser pulse hits the thin carbon layer and the induced thermal expansion generates a mechanical shock wave.

A process flow that allows for the simultaneous fabrication of emitters on silicon (on the left, in the figure) and dielectric (on the right) membranes with well-controlled and homogeneous features has been defined and implemented experimentally. In the process, the former type of membrane assures a faster cooling of carbon because of its high thermal conductance and provides higher stiffness. In the latter, instead, the absorbing layer can be directly irradiated, eliminating the optical power loss due to absorption in silicon and maximizing the opto-acoustic conversion efficiency. The dielectric membrane is constituted by several layers of silicon oxide and nitride, where the thicknesses are appropriately chosen in order to balance the tensile and compressive stresses in the different films.

In both the devices described, silicon micromachining is used to permit the housing of the optical fiber as close as possible to the absorbing layers.
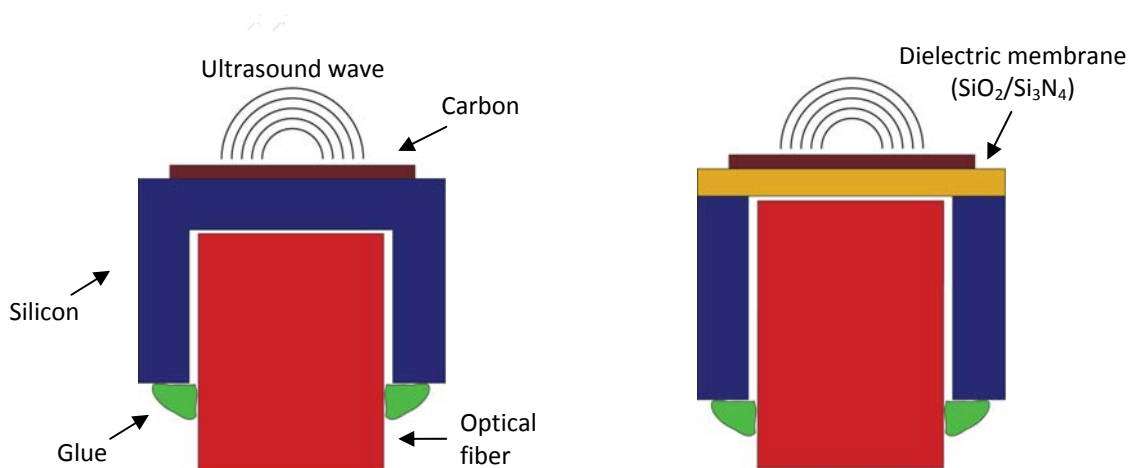
Fig. 2.1. Ultrasound sources with absorbing layer deposited respectively on silicon (left) and dielectric (right) membranes

2.2 Theory of Optoacoustic Generation

Thanks to the increasing interest devoted by the scientific community to opto-acoustic generation, the thermo elastic effect has been exhaustively studied and several models have been proposed [5] [6] [7]. An analytical solution of the problem, which permits an accurate description of acoustic propagation, is possible only for particular geometries and often finite element methods are preferred to describe the physical phenomena involved in

thermoelastic generation. However, independently of the solution method adopted, the acoustic waves generated by optical absorption can be calculated by solving a multiphysics problem in a spatial domain Ω, where an elastic solid (Ω_s) is immersed in a fluid (Ω_f). The optical absorption in the elastic body can be determined by applying the Fresnel and Snell equations at the interfaces of the films that constitute the irradiated solid. The thermal absorption within the elastic solid produces heat transfer effects dominated by thermal conduction in both the solid and liquid-phase domains, and therefore the Fourier's law has to be considered to determine the temperature profile in the material. The heat diffusion equation that should be solved to calculate the temperature profile within the emitter to a first-order approximation is reported below

$$\nabla^2 T - \frac{1}{D}\frac{\partial T}{\partial t} = -\frac{1}{k}Q \tag{2.1}$$

where Q is the heat source (W/m^3) dependent on optical absorption, D and k the thermal diffusivity and conductivity respectively (supposed as constants within the integration domain). Sometimes, a modified Fourier's law has been considered to keep into account the finite speed of heat flux propagation, resulting in a hyperbolic heat equation [8]. Nevertheless the temperature profiles predicted by the two different theories are similar and considerable variations can be noticed only for time scales much shorter than 1 ns. A more complete representation of the phenomenon, which also considers the heat produced by mechanical deformation, is given by [9]:

$$\nabla^2 T - \frac{1}{D}\frac{\partial T}{\partial t} = -\frac{1}{k}Q + \underbrace{\frac{K\beta T_0}{k}\nabla \cdot \frac{\partial \boldsymbol{u}}{\partial t}}$$

Transformation of mechanical energy in
thermal energy

where K is the Bulk modulus, β the volumetric thermal expansion coefficient and T_0 the ambient temperature. However, in the thermoelastic regime, it has been shown that the heat produced by mechanical deformation can be neglected [9].

In the MOMS device described previously, the heat source Q (expressed by the spatial derivative of the optical intensity I with respect to the direction of electromagnetic

propagation) can be determined by considering a Gaussian distribution of the laser beam. Furthermore the use of cylindrical coordinates is particularly convenient for the geometry considered and allows reducing the tridimensional problem to two-dimensional domain (with axial radial coordinates *z* and *r*). In this way the heat source can be calculated as

$$Q = \frac{\partial I}{\partial z} = -\alpha_o(1 - R) \exp{(-\alpha_o z)} f(t) g(r) \tag{2.2}$$

with

$$f(t) = I_0 \frac{t}{t_0} \exp{\left(-\frac{t}{t_0}\right)}$$

$$g(r) = \exp{\left(-\frac{r^2}{a_0^2}\right)}$$

In eq. (2.2), f(t) and g(r) are the temporal and spatial distributions of the pulsed laser line, respectively dependent on the rise time of the laser pulse t_0 and on the core diameter of the optical fiber a_0. Moreover, α_o and *R* are respectively the optical absorption coefficient and the reflectance of the carbon layer. Once determined the temperature distribution through eq. (2.1), the strain induced from the thermoelastic volumetric change in the solid and the consequent acoustic propagation in the fluid can be calculated by using a Fluid-Structure interaction model. In order to do that, the time-harmonic Helmholtz equation (2.3) can be used for calculating the acoustic pressure in the fluid, while the Green-Naghdi model (2.4) [10] can be adopted to describe thermoelastic effect in the solid film.

$$\nabla^2 p + \frac{\omega^2}{c_s^2} p = 0 \ \ \text{in } \Omega_f \tag{2.3}$$

$$\mu \nabla^2 \boldsymbol{u} + (\lambda + \mu)\nabla\nabla \cdot \boldsymbol{u} - \gamma\nabla T = -\rho \, \omega^2 \boldsymbol{u} \ \ \text{in } \Omega_s \tag{2.4}$$

In these equations, *p* is the acoustic pressure, ω the angular frequency, c_s the speed of sound, **u** the displacement vector, ρ the mass density, λ and μ the Lamé constants, with γ given by

$$\gamma = (3\lambda + 2\mu)\alpha = K\beta \tag{2.5}$$

where α and β are respectively the linear and volume thermal expansion coefficients.

The stress tensor associated with the displacement and the temperature change calculated by eqs. (2.1), (2.3) and (2.4) is expressed by [11]

$$T_S = \lambda(\nabla \cdot \boldsymbol{u})I_T + \mu \left(\nabla\boldsymbol{u} + \nabla\boldsymbol{u}^{\mathrm{T}}\right) - \gamma(T - T_0)I_T \tag{2.6}$$

where I_T is the identity tensor and T_0 the ambient temperature.

The description of the opto-acoustic generation phenomenon is then completed by applying the boundary conditions at the solid-liquid interface, as reported below:

$$\frac{\partial p}{\partial n} = \omega^2 \rho_f \boldsymbol{u} \cdot \boldsymbol{n} \tag{2.7}$$

$$\boldsymbol{T}^{(n)} \cdot \boldsymbol{n} = -p \tag{2.8}$$

$$\boldsymbol{T}^{(n)} \cdot \boldsymbol{t} = 0 \tag{2.9}$$

where $\boldsymbol{T}^{(n)}$ is the stress vector (equal to $T_S \cdot \boldsymbol{n}$). The (2.7) guarantees the continuity of the normal displacement component, while the (2.8) and (2.9) allow satisfying the continuity of tangential and normal components of traction, where the vanishing tangential condition is obtained by neglecting the shear force in the fluid.

As can be observed by (2.4) and (2.6), two different kinds of acoustic source exist. The temperature profile is taken into account by the temperature gradient in the Green-Naghdi equation and, at the same time, a force source proportional to the temperature change is expressed by the stress tensor in the boundary condition (2.8). Moreover, the thermoelastic effect in water is neglected in eq. (2.3), assuming the ultrasonic generation to be mainly due to the thermal expansion of the thin layer. The correctness of this hypothesis depends on properties of thin absorbing film. Anyway, even without complicating the model too much, the thermal expansion in water can be taken into account by also considering the well known Green-Naghdi equation in the fluid. As demonstrated by Helmholtz theory [12], every continuous vector field can be represented as the sum of the gradient of a scalar potential plus the curl of a vector potential. This useful representation allows writing the elastic displacement as

$$\boldsymbol{u} = \nabla\phi + \nabla \times \boldsymbol{\psi} \tag{2.10}$$

where $\nabla\phi$ is often called lamellar potential and $\nabla \times \boldsymbol{\psi}$ rotational potential, with $\boldsymbol{\psi} = (0,0,\psi)$. By substituting the displacement in the Green-Naghdi equation and exploiting (2.10), the longitudinal and shear acoustic waves can be determined separately, yielding

$$\nabla^2\phi - \frac{1}{c_L{}^2}\frac{\partial^2\phi}{\partial t^2} = \frac{\gamma(T-T_0)}{c_L{}^2\rho} \tag{2.11}$$

$$\nabla^2\psi - \frac{1}{c_S{}^2}\frac{\partial^2\psi}{\partial t^2} = 0 \tag{2.12}$$

in which c_L and c_S are the longitudinal and shear wave speeds, respectively. Considering that only longitudinal acoustic waves propagate in a fluid, the determination of acoustic pressure is further simplified, requiring the solution of the only scalar potential equation. Finally, the pressure is related to the scalar potential by

$$p = -K\,\nabla^2\phi \tag{2.13}$$

In conclusion, the acoustic waves generated by absorption of a nanosecond pulsed laser can be calculated by first solving the heat equation (2.1) in order to determine the temperature profile, and, successively, by calculating the pressure from eq. (2.4) with adequate boundary conditions. In fact, neglecting the thermal variations induced from the mechanical deformation, the two equations are uncoupled and can be solved separately.

Anyway, particular attention has to be posed to the derivation of the energy absorbed from the carbon film, expressed by the heat source term in eq. (2.1), in order to predict the correct temperature distribution. This can be done by developing proper test structures in order to estimate the optical constants of the thin films involved in thermoelastic generation and correctly model the light propagation through multilayer structures. Since a thermo-elastic principle is exploited in the emitter, the mechanical and thermal properties of the carbon layer (Young's modulus, Poisson ratio and thermal conductivity) should also be determined to accurately predict the acoustic generation.

2.3 Process Flow

The fabrication process of the thermoelastic MOMS sources has been defined as follows.

Starting from 500 μm thick <100> oriented Double Side Polished (DSP) silicon substrates, a thermal oxidation step is carried out at 1000 °C in wet environment, yielding a roughly 700 nm thick silicon oxide layer on both sides of the wafer (step 2, Fig. 2.2). Stoichiometric silicon nitride is then deposited by Low-Pressure Chemical Vapor Deposition (LPCVD) from dichlorosilane and ammonia at 780 °C on both sides of the substrate, as well (step 3). Afterwards, a 1 μm thick low-temperature silicon dioxide layer (LTO) which completes the stress-compensate membrane, is deposited by LPCVD from silane at 420 °C (step 4) and thickened up to 3 μm on the back side only with an additional deposition, performed after covering the wafer front with a dummy substrate in order to prevent LTO deposition on that side (step 5). The thick LTO layer obtained in this way is needed as an etch mask in the final Deep Reactive Ion Etching (DRIE) step of the process, as will be explained in the following.

After completion of the stress-compensated membrane, a roughly 100 nm thick standard CMOS LPCVD polysilicon layer is deposited by CVD from silane at 585 °C and patterned by near-UV contact lithography and wet etching performed with an HNO_3:HF:Deionized Water (DI) solution (steps 6-7). This polysilicon layer will be used as an adhesion layer for the carbon emitters realized on dielectric membrane, as will be explained in deeper detail later on.

The SiO_2/Si_3N_4 thick layer obtained on the back side of the wafer is then patterned with back-front alignment by means of an ICP (Inductively Coupled Plasma) SiO_2/Si_3N_4 Deep Reactive ion etching chemistry based on C_4F_8, showing a rate of roughly 0.5 μm/min on SiO_2 and 0.2 μm/min on Si_3N_4 (step 8) in order to define the MOMS geometry for the final silicon DRIE micromachining. Since, in the completed devices, both carbon emitters on thin SiO_2/Si_3N_4 membranes and on thicker bulk Si membranes have to be fabricated, the backside micromachining process has been defined in order to allow differentiated etching depths on lithographically defined geometries on the wafer backside. In order to do that, a 4 μm thick photoresist (OiR 908-35) is spun on the wafer backside, and patterned by exposure and development in order to selectively uncover the areas in which the final silicon DRIE etching must reach the dielectric membranes on the wafer front side. In this operation, the use of a relatively thick resist is needed in order to provide good coverage on the high steps created by the ICP etching of the roughly 4 μm thick dielectric stack on the backside.

After the OiR patterning, a silicon DRIE time etching step is performed, yielding a roughly 100 μm deep etching (actually slightly variable with the diameter of the etched area) on the defined geometries selected for "deeper" etching. The DRIE is performed by means of a SF_6/C_4F_8 Bosch process providing an average silicon etch rate around 5 μm/min.

After this first backside DRIE step, a procedure similar to the one illustrated before for the backside patterning of the SiO_2/Si_3N_4 stack (but using a capacitively coupled RIE CHF_3 etching instead of the ICP) is utilized on the front side for removing the stress compensated membrane on selected regions, in which the carbon layers on bulk silicon membranes will be subsequently realized (step 10). Then, the fabrication of the carbon layers needed in the ultrasonic emitters is started by spinning a 4 μm thick OiR 908-35 photoresist layer on the wafer front side at 3000 rpm. The spun resist is subsequently carbonized by means of an annealing step performed at 800 °C in argon atmosphere for 40 minutes (step 12). In this way, thanks to the properties of resist, the desired pattern is quite smoothly obtained before the carbonization step by operating a simple exposure and lithographic development procedure, with micrometric control of the geometry.

After completion of carbon layer fabrication, a further DRIE time etching process is performed to complete the devices before fiber insertion (step 14), carefully controlling the etching time in order to realize both the thick (around 100 μm) bulk silicon membranes by stopping the etching properly and the dielectric membranes in the areas already etched within the previous backside DRIE step.

1. Silicon Bulk (500 μm)	2. Thermal Oxide (700 nm)	3. Nitride (300 nm)

4. Low Temperature oxide (LTO,1μm)	5. Back LTO deposition (2 μm)	6. Polysilicon deposition (100nm)

7. Wet Poly patterning

8. SiO$_2$/Si$_3$N$_4$ patterning

9. Back photoresist mask

9. Deep reactive ion etching (100μm) and resist stripping

10. Dielectric membrane patterning

11. Photoresist

12. Resist carbonization

13. Silicon DRIE (400 μm)

14. Fiber insertion

Fig. 2.2. Process flow for the fabrication of ultrasonic sources on silicon and dielectric membranes

As discussed previously, the optical attenuation coefficient of carbon is of special concern for the emitter performances, since the ultrasound emission band is, to a first approximation, inversely proportional to the optical penetration depth of the laser in the emitting material [13]. As a consequence of that, in order to achieve a wideband emission, it is useful to optimize the carbonization process in order to have high optical absorption per unit length on the carbon layer. This problem will be investigated in sections 2.5 and 2.6 by taking into consideration process parameters that may influence the optical absorption properties of the produced carbon (e.g. employing different annealing temperatures to obtain carbon with a higher graphitization level).

2.4 Fabrication of MOMS-Based Emitters

In the experimental tests carried out to define the appropriate process parameters for the fabrication of the MOMS emitters, the first relevant photolithographic patterning was realized at step 8, after silicon oxide and nitride deposition, by using OiR 908-35 photoresist as a mask layer and SiO_2/Si_3N_4 ICP etching. Some optical images taken after the dielectric stack etching from the backside are shown in Fig. 2.3. For every geometry, a peripheral donut etching shape was designed in order to allow the separation of devices by modifying the previously introduced process flow, as will be described in deeper detail in the last chapter of this thesis. As may observed in the figure, various shapes have been obtained, which may be used to fabricate devices with different geometry.

On the left side of the figure, for instance, the LTO patterning needed for the fabrication of 5 ultrasound emitters is reported. The central structure, instead, was conceived for coupling the MOMS probe with a multicore fiber, and designed in order to minimize its size and enable the fabrication of an array of 4 ultrasonic sources with overall diameter smaller than 300 μm. A particular geometry is finally depicted on the right, in which several circular etched shapes are joined to each other in order to allow the use of an optical fiber bundle.
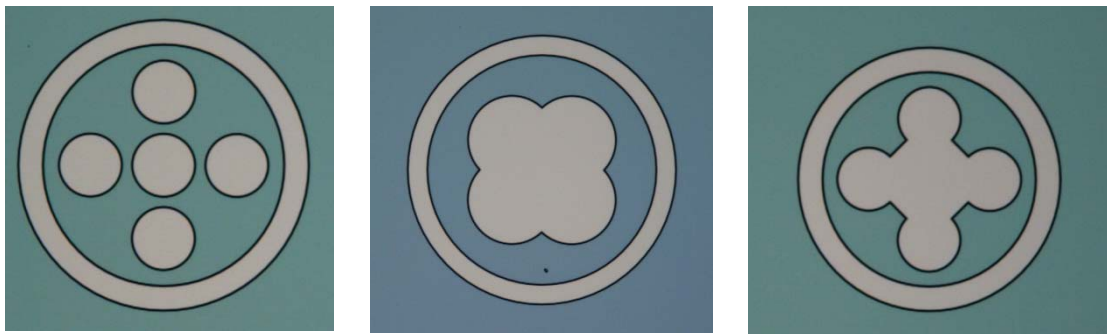
Fig. 2.3. Optical Images after SiO2/Si3N4 (back side patterning, step 8)

Thanks to the process flow described, the realization of several prototypes of ultrasonic emitters was possible, but the experimental tests put into evidence a few critical aspects in the process that were not fully foreseen in its initial design. The first challenging issue emerged during these first tests was the strong dependence of the DRIE etching rate on the etched feature size, particularly for very deep etching steps like those adopted in the process under examination. As can be observed in the SEM cross-sectional image of Fig. 2.4, actually, where a silicon deep reactive ion etching with the low frequency Bosch recipe employed in

the process is performed on structures of different sizes, the etching rate is strongly dependent on the geometry and this makes the simultaneous fabrication of ultrasound sources with diameter from 100 μm to 600 μm quite challenging. In this respect, it is worth noting that the smallest structures visible in figure have a diameter of 50 μm and an etching rate of roughly 4 μm/min against the 5.5 μm/min of the larger structures.   Despite the different rates observed, the Bosch DRIE process used yielded a satisfying wall profile, which allowed for maintaining the designed mask patterning during the long etching step, with only a slight and in the end acceptable widening of the etched shape.
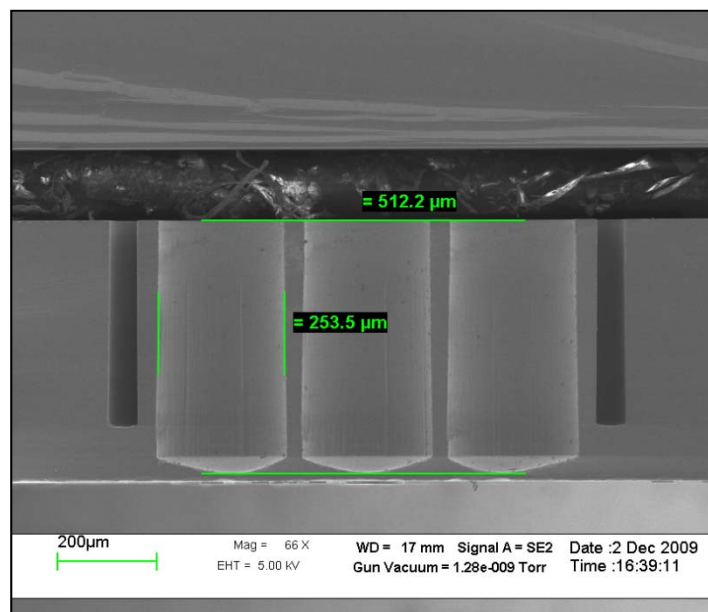
Fig 2.4. SEM image of a silicon wafer subjected to 92 min deep reactive ion etching.

Coming back to the fabrication process, in order to realize the double depth silicon etching described earlier, the backside was masked with a thick photoresist at step 9. In order to perform the lithography correctly, in this step the exposure time had to be increased up to 15 sec rather than nominal 9.6 sec reported by the constructor for the OiR 908-35. In the exposure of a positive resist, in fact, the regions that are exposed to light become soluble to the photoresist developer. Taking into account the presence of thick micromachining on the backside, a longer exposure time allows removing the resist close to the high steps, where light diffraction, interference effects and shadowing phenomena do not permit a perfect exposure. Naturally, this longer exposure time results also in a shrinking of the patterned

regions that turned out to be small enough to preserve process feasibility. Once checked the resist mask by optical observation at the microscope, silicon was etched for 15 min using the DRIE process. Afterwards, the dielectric membrane was removed on the front side in correspondence to the location of the silicon membranes through resist masking and reactive ion etching. The dielectric multistack, constituted by silicon oxide and nitride and covered with a thin polysilicon layer, in fact, is not needed on the bulk silicon membranes and its presence might be detrimental for the emission performances because it would introduce additional optical interfaces, leading to a reduction of the incoming optical power on the absorbing film. As may be easily verified by means of optical simulations, the transmittance of the membrane would be sensibly reduced for the presence of the polycrystalline silicon adhesion layer, which cannot be eliminated when resist carbonization is performed on silicon dioxide for the poor adhesion of the carbon layer on it.

In the first tests, differently from the process flow described previously, the photoresist OiR 908-35 was spun before completing the final backside silicon DRIE etching and the carbonization was realized as a final step, providing the possibility to anneal in a different way samples cut from various parts of the same wafer, as will be more thoroughly described in the next section. Some optical images taken after the silicon deep etching from the backside are reported by way of example in Fig. 2.5, where arrays of respectively 9 and 5 ultrasonic sources are shown (with 800 and 400 µm overall diameters of the entire MOMS, respectively).
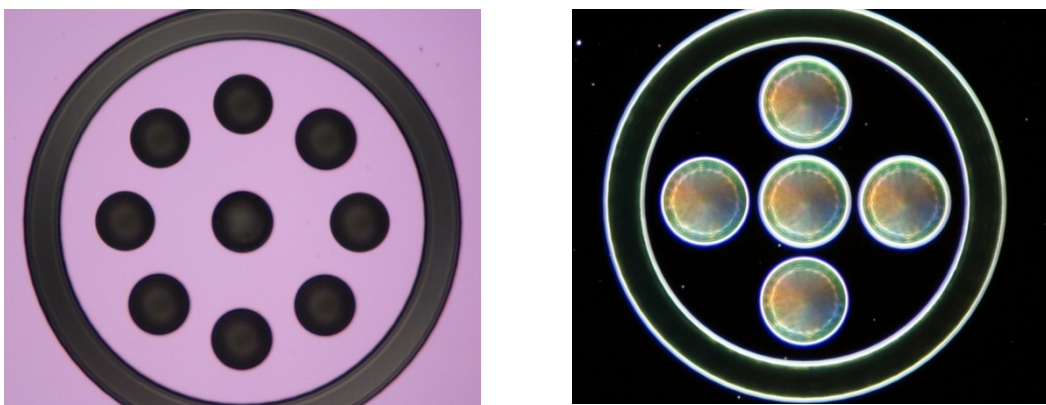
Fig. 2.5. Backside views of micromachined structures after 15 min silicon deep reactive ion etching. A dark field image is reported on the right.

In the figure, a dark field image is shown on the right. In this particular acquisition, the sample under observation is not illuminated frontally, since the light comes along the sides of the microscope stage. As a consequence of this particular illumination, the background of the image appears dark because the observer can only see the scattered light from the vertical features existing on the specimen, providing high contrast on the micromachined parts of the sample, and putting into evidence all the vertical walls with a bright tone.

Other optical observations performed on carbon emitters realized on silicon and dielectric membranes are reported in Fig. 2.6a before the carbonization process. As expected from theoretical considerations about the transparency of the dielectric SiO_2/Si_3N_4 stack, the dielectric membrane appears bright when illuminated from the backside at the microscope, since the silicon beneath has been completed removed and visible light is allowed to cross the silicon oxide and nitride films without remarkable attenuation.

In Fig. 2.6b an example of carbon layer, obtained on dielectric membrane thanks to annealing process, is finally shown. The dark color confirms the high optical absorption of the carbon layer in the visible frequency range, a property that should make it suitable for opto-acoustic generation.
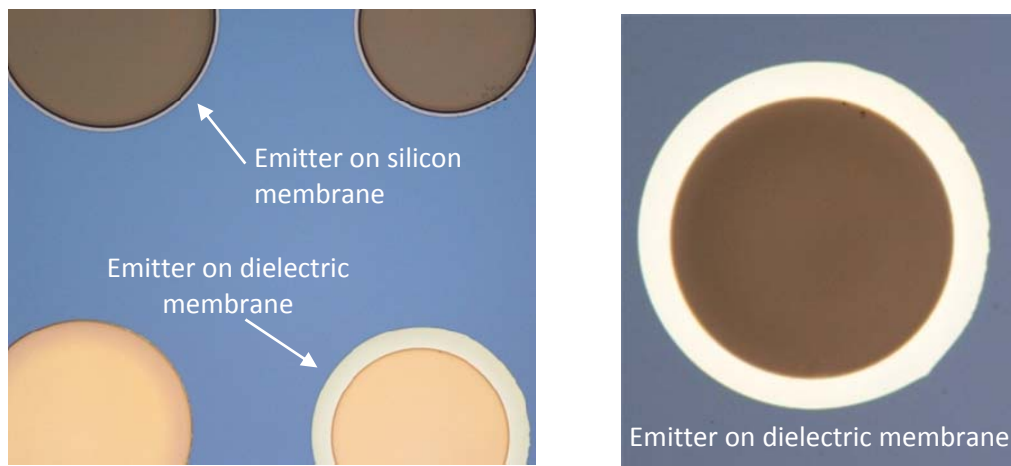
Fig. 2.6. Front side views before (a, left) and after (b) the carbonization process

A SEM image of carbon films patterned with circular shapes is also shown in Fig. 2.7. As may be observed, the boundary appears slightly notched because of the volume reduction of the layer during annealing and, furthermore, some particulate is visible on the top. The darker

color in the central region is due to a not perfectly plane border profile owing to the thickness variation induced by carbonization close to the boundary of the patterned feature, as will be cleared in the next section. The three emitters reported in the image were realized on dielectric membrane.
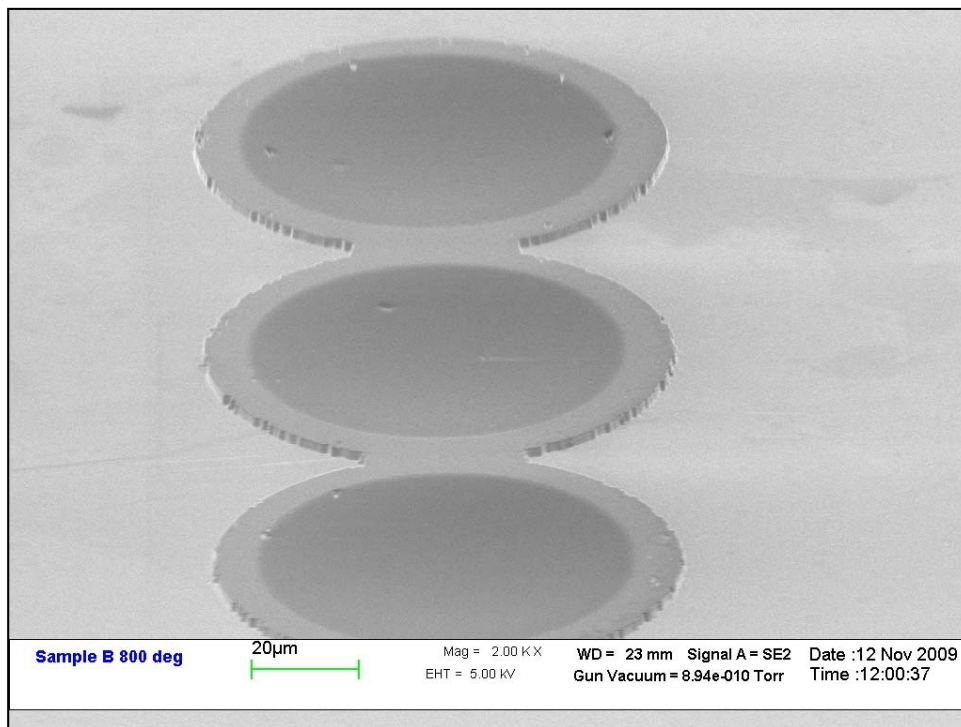
Fig. 2.7 SEM image of amorphous carbon layer

The appearance of the back side silicon micromachined cavities obtained in the experimental tests can be observed in the SEM image reported in Fig 2.8a. The good quality of the etching profile obtained in these tests has to be mainly ascribed to the characteristics of the Bosch process, where etching and passivation cycles are alternated to achieve highly anisotropic vertically etched structures. In this process, the chemical deposition of an inert passivation layer (C_4F_8) is alternated to a sulfur hexafluoride (SF_6) plasma isotropic etching step, allowing for etching in the vertical direction. The deposition/etching steps are automatically alternated many times during the process, in order to preserve anisotropy.

Anyway the alternation of these two different phases leads to the typical scalloping of deep reactive ion etching, which created a controlled undulation of the sidewalls characterized by average amplitude of a few hundreds of nanometers, depending on the duration of the passivation/etching steps. In case the sidewall scalloping represents a problem, the

frequency of these cycles can be opportunely set to reduce this effect. In Fig. 2.8b a detail of the etching sidewall is shown by way of example, in which the scalloping is quite clearly visible due to the low passivation/etching cycle frequency employed (7 s SF_6 and 2 s C_4F_8). Other examples of back side silicon micromachining observed by SEM are reported in Figs. 2.9 and 2.10. These images have been taken on MOMS based arrays of ultrasonic emitters, designed to demonstrate the potentiality of the developed technology concerning integration density. As may be seen in the figures, several individual emitters can be rather easily realized on the same MOMS, in order to constitute ultrasonic sources with more complex structure with respect to a plain single emitter. In these arrays, every ultrasonic generator can be, in principle, independently controlled by using more laser sources or switching a single laser beam among the different fibers. In this way, the emission performances could be considerably increased, resulting in a wider spatial distribution of the acoustic field. In the micromachining tests, it was verified that, once fixed a minimum thickness for the silicon spacer between two adjacent cavities (which was 50 µm in the process implemented), the maximum integration is only limited by the minimal fiber size useful to propagate a sufficient optical energy up to the carbon emitter. In order to overcome this limitation, some MOMS in the test mask set have been designed for use with multicore fibers, which could permit the integration of tens of emitters on circular silicon areas with diameter smaller than 500 µm.
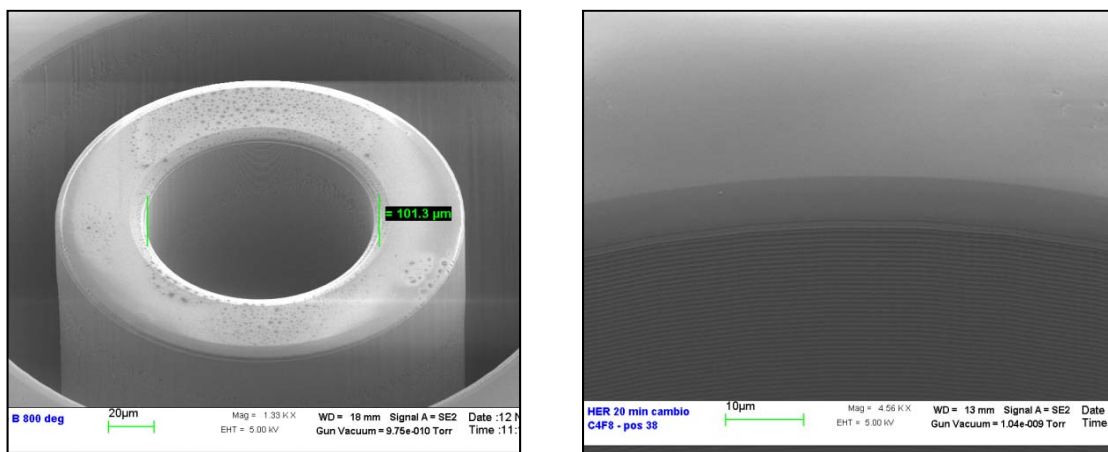
Fig. 2.8. Backside DRIE micromachining for the fiber housing (a) and typical scalloping of the etching (b)
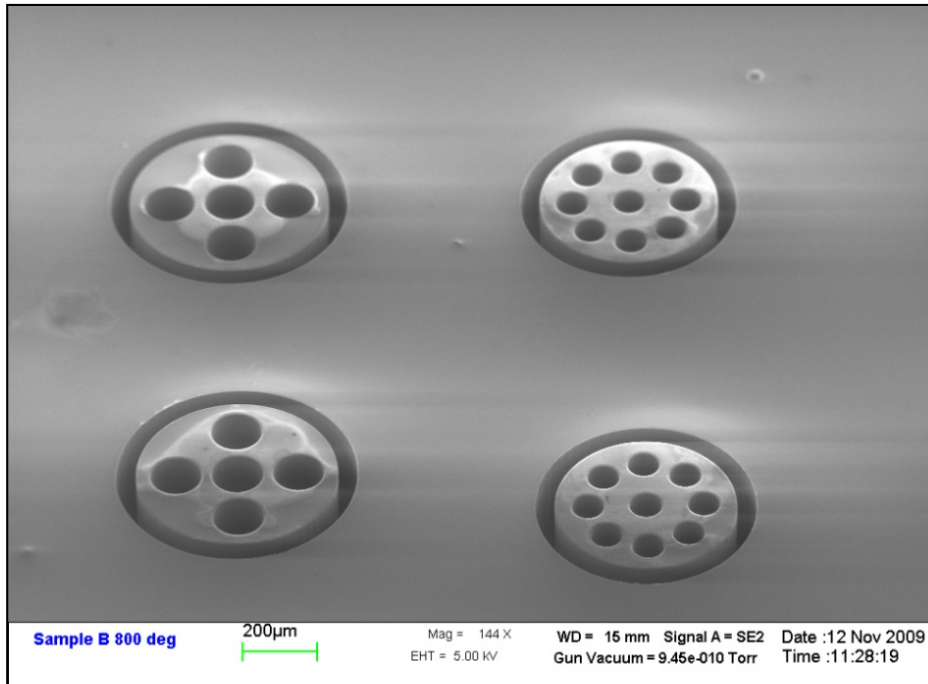
Fig. 2.9. SEM image of MOMS-based arrays of ultrasonic emitters (back side view)
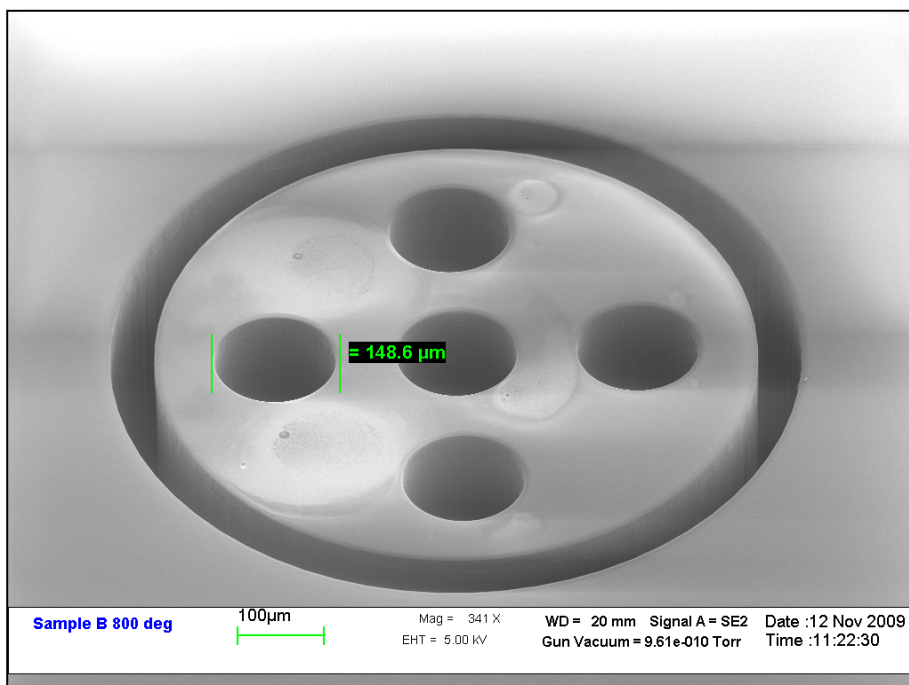
Fig. 2.10. View of a 5-emitters array of roughly 650 μm overall diameter

2.5. Photoresist Carbonization

As discussed before, the employment of photoresist as a starting material for the fabrication of carbon layers is very convenient since it allows easy patterning of optically absorbing microstructures by photolithography techniques. Carbon films have been produced by other groups by the pyrolysis of AZ4330 [14] and SU-8 [15] photoresists with possible applications as electrode materials in chemical sensing and in electrochemically based MEMS devices. In this thesis, differently than the examples available in the literature, the use of carbon layers obtained by carbonization of OiR 908-35 photoresist has been studied for efficient optoacoustic conversion.

In order to investigate the carbonization process, some first tests were performed in preliminary experiments, which put into evidence the necessity to dip the silicon wafers in a dilute hydrofluoric solution to etch the native silicon dioxide before photoresist spinning in order to enhance carbon adhesion on silicon. This step proved to be very important in carbonization of photoresist layers on silicon, since the adhesion of carbon on silicon dioxide, even few nanometers thick like native oxide, was very poor, as verified by scratch tests performed by M3 Scotch Brite (Glass 270 syrom). In fact, as shown in Fig. 2.11, when the HF dip was not performed before carbonization, the carbon layer was completely stripped in the scratch test, while with the correct procedure adhesion evaluated with the same method was very good. As a result of these tests, the 100 nm thick polysilicon adhesion layer was inserted in the process flow presented in section 2.3 (steps 6 and 7 in Fig. 2.2), in order to allow a sufficient adhesion of carbon in the emitters realized on dielectric membrane.
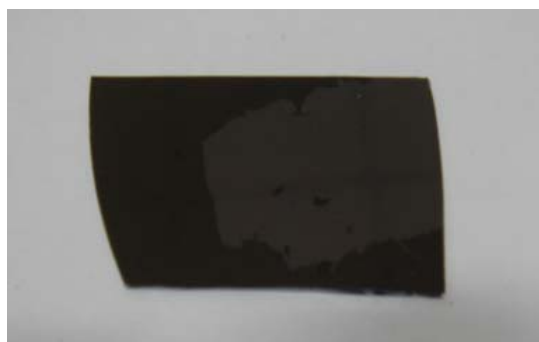
Fig. 2.11 Scratch test on a carbonized resist (without HF dip before spinning)

For the same reason, the silicon wafers, at step 11 of the process previously described, were cleaned by dilute hydrofluoric solution and furthermore treated with hexamethyldisilazane

(HMDS), which is a common primer used before resist spin coating to promote adhesion. OiR 908-35 resist was then spun at 3000 rpm for 30 s, leading to 4 μm thick layer, which was soft baked in hot plate at 110 °C for 1 min. Afterwards, the photoresist films were carbonized in both inert and reducing environment by annealing the samples at several temperatures. In particular, carbon properties were investigated as a function of four annealing temperatures (800°C, 900°C, 1000°C and 1100°C) and considering two different pyrolysis atmospheres: Argon and Forming gas (90% N_2 and 10% H_2).

All the samples were heated with a ramp performed from the room temperature to the plateau value adopting a fixed rise time of 15 min, annealed for 10 min and cooled to room temperature in the pyrolysis atmospheres before exposure to air. The different carbonization processes were realized by both a J.I.P.ELEC and a Rapid Thermal Processing (RTP) equipment. The former is an induction furnace specially developed for the ultra-high-temperature processing of silicon carbide, where samples are annealed in an inductively heated graphite chamber. The latter, instead, is a lamp-based heating system in which the sample can be heated and cooled rapidly within a water cooled quartz chamber.

In order to determine the thicknesses of the carbon layers and to investigate the carbonization process dependence on the planar geometry of annealed structure, the thickness profile of the annealed films was measured before and after pyrolysis, using a stylus profilometer. These measurements put into evidence a marked volume reduction of the film after carbonization, consistently with other results reported in the literature, with a thickness reduction around 75% with respect to the original 4 μm thick resist layer. As shown in Fig. 2.12, the thickness reduction after carbonization turned out to be strongly dependent on the diameter of circular shape carbonized. Besides thickness reduction, a small shrinking in lateral dimension was observed on the patterned geometries resulting in a slight increase in thickness close to structure boundaries. This effect was particularly marked on structures with diameter smaller than 200 μm, in which the pyrolysis led to convex structures because of the gathering of the thicker border regions, resulting in a higher average thickness of the pattern (see the measurements reported in the figure below). In the larger structures, instead, a wide flat profile was observed in the central region of the pattern.
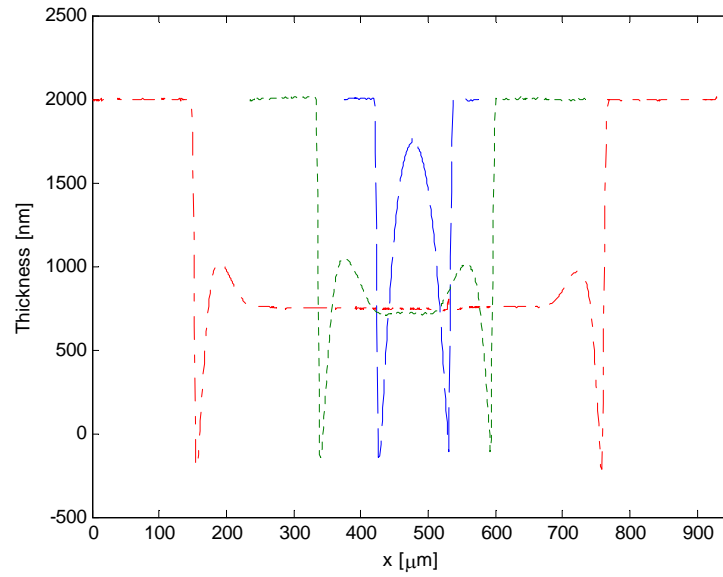
Fig. 2.12 Carbon thickness profiles as a function of diameter (900°C annealing temperature)

In Figs. 2.13, 2.14, 2.15 and 2.16, the thicknesses of the carbon layers as a function of the diameter of the original patterned structures are reported for annealings performed at the temperatures of 800°C, 900°C, 1000°C and 1100°C. In this case, the carbonization process was realized in Argon atmosphere by using the J.I.P.ELEC furnace.
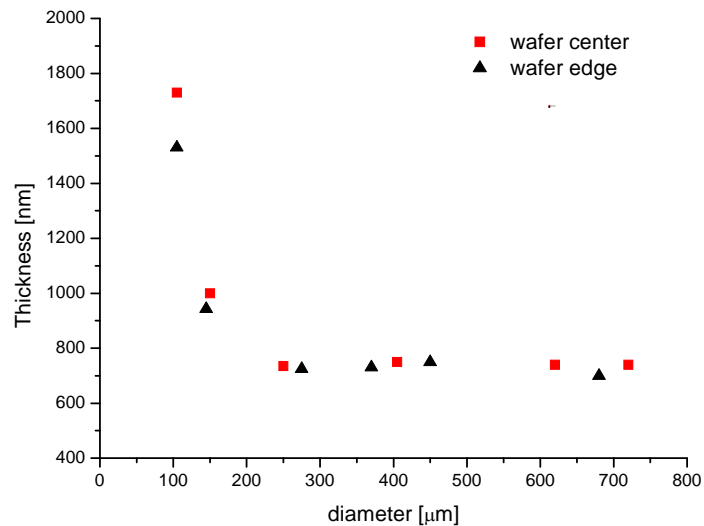
**Fig. 2.13. Thicknesses of patterned carbon as a function of diameter
(800°C annealing temperature)**

In order to calculate the values reported in the plot, several measurements were performed on similar circular structures in various regions of the annealed samples and averaged. The measurements put into evidence that, although a good uniformity was noticed before annealing (the spun photoresist was roughly 4 μm thick in the whole region of interest), the carbonization process induced a thickness reduction that was slightly lower in the central region of the wafer, confirming the theoretical expectations concerning temperature distribution in the annealing chamber. In fact, in the J.I.P.ELEC furnace, which is based on induction heating, the annealing temperature has a radial profile, decreasing from the chamber wall towards its center.
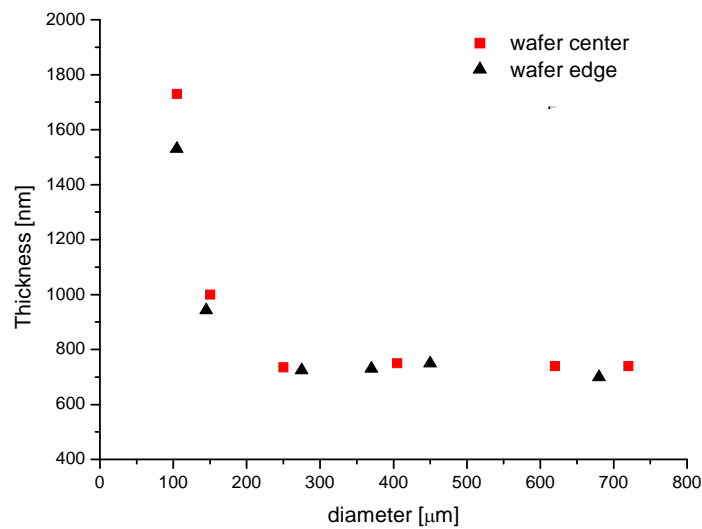
**Fig. 2.14. Thicknesses of patterned carbon as a function of diameter
(900°C annealing temperature)**

Moreover, by comparing the data obtained at different annealing temperatures, it was found that, for the largest structures, the shrinking due to pyrolysis increased with the annealing temperature. In particular, the relative reductions in the films thickness were respectively 79%, 82%, 84% and 85% for the considered carbonization temperatures, from the lowest to the highest.
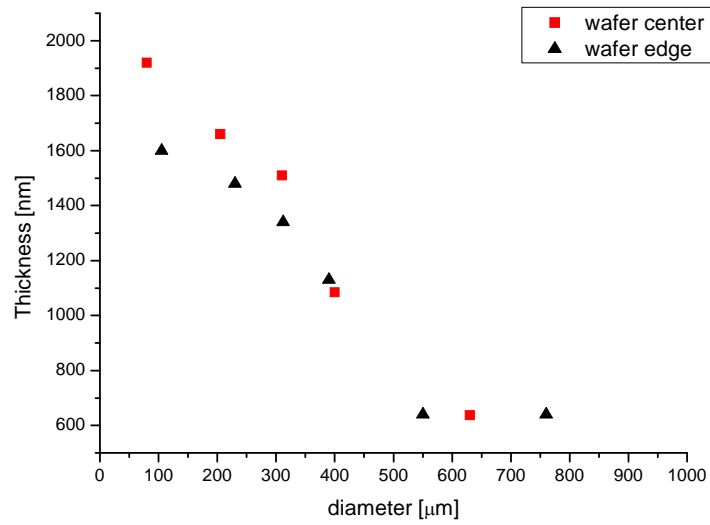
Fig. 2.15. Thicknesses of patterned carbon as a function of diameter (1000°C annealing temperature)
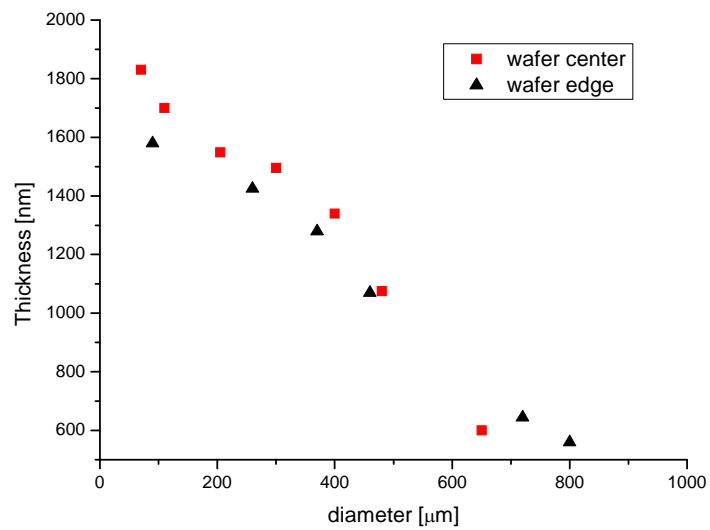
Fig.2.16. Thicknesses of patterned carbon as a function of diameter (1100°C annealing temperature)

However, as can be shown in Fig. 2.17, high temperature annealing allowed better control of the shrinking reduction on small and medium sized circular patterns.

From these results, it is quite clear that, within certain limitations determined by the initial thickness of the resist layer and by the unavoidable thickness reduction during carbonization,

the carbon thickness can be in principle tuned by appropriately patterning the photoresist and performing the annealing at the right temperature, even if the pattern planar geometry if often constrained by other considerations in the application described. This can be useful for optimizing the optoacoustic emission performances of the carbon layers, since, as discussed previously, the possibility to control the thickness of the absorbing layer is of primary importance in optoacoustic generation.
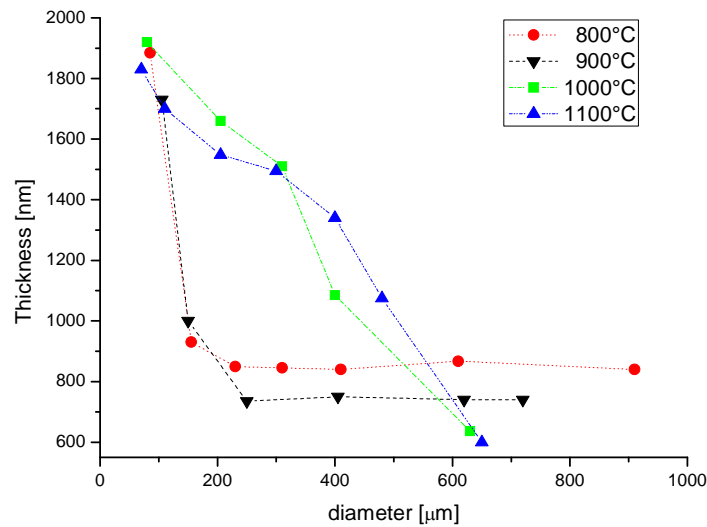
Fig. 2.17. Thicknesses of carbon films against the diameters for the several annealing temperatures

The structural characterization of the carbon layers obtained by resist pyrolysis was completed by cross-sectional SEM observations, which allowed for investigating the roughness of the upper surface of the layers and the appearance of the single crystal silicon/carbon interface. In Fig 2.18 two cross sectional SEM images performed on unpatterned carbon samples obtained with two different pyrolysis atmospheres are reported by way of example. In particular, the resist in Fig. 2.18a was annealed in Forming gas atmosphere (90% N_2, 10% H_2) using the RTP furnace at a temperature of 750°C, leading to a roughly 1.3 μm thickness. The other sample, instead, was pyrolyzed in Argon by J.I.P.ELEC at the same temperature, resulting in a thinner carbon film, as may be seen in Fig. 2.18b.
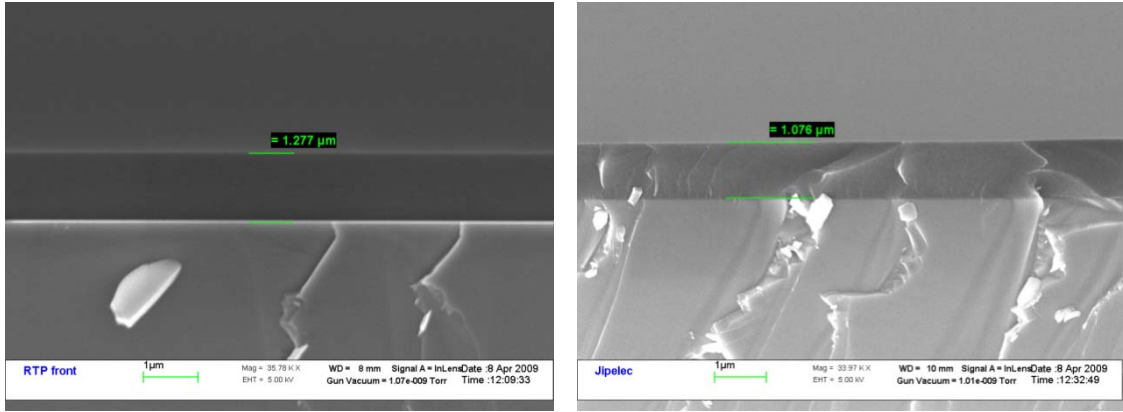
Fig. 2.18. SEM image of the pyrolyzed resists, annealed in Forming gas (left, 1.3 μm thick) and Argon (right, 1 μm thickness).

2.6 Optical Characterization

2.6.1 Introduction

The problem of optical characterization of a thin film in a multilayer structure has been extensively investigated in the literature [16] [17] and several techniques have been proposed. Some of them are based upon multiple reflection and transmission measurements, whereas other ones rely on single reflectance data. Generally speaking, every technique presents peculiar advantages and drawbacks and often the choice of the characterization procedure is mainly determined by the available experimental setup. Most common approaches employ optimization algorithms based on classical oscillators and empirical relations or, alternatively, Kramers-Kronig analysis [18]. The latter method, according to which the characterization is operated by solving an integral expression, requires some approximations in order to take into account the contribution on reflectance (or transmittance) outside the experimental measurement range and consequently some errors may arise. As can be observed by the Kramers-Kronig relation reported below,

$$\varphi(\omega') = \frac{\omega'}{\pi} P \int_0^\infty \frac{\ln R(\omega)}{\omega'^2 - \omega^2} d\omega$$

the phase shift of the electromagnetic wave φ is related to the reflectance measurement R, where P is the principal value of the integral, but its exact value cannot be calculated

because this would require an optical measurement realized over an infinite frequency range. Anyway, several techniques have been proposed in order to realize the best approximation of the Kramers-Kronig relation [19].

The classic oscillator approach, on the contrary, allows for a correct refractive index determination and its use has been preferred in this type of characterizations. In order to perform the optical characterization of thin layers by photometric and infrared spectrometric measurements, a new stand alone software application has been developed within this thesis (Fig. 2.19). The optimization algorithm implemented in the application allows for the simultaneous fitting on more experimental results and for the management of several unknown layers in the same multi-layer structure. Various theoretical models (Lorentz, Drude, Cauchy, etc.) have been utilized in the extraction routines for reducing the solution numbers and satisfying the Kramers-Krong relation between real and imaginary parts of complex refractive index. The software has been designed for working as a Matlab tool as well and can be easily optimized for every particular application.

Thanks to minimization of an error function, proportional to the mismatch between experimental measurements and optical simulations, unknown refractive indexes and thicknesses are determined by first using a simulated annealing minimization algorithm and, subsequently, gradient based methods to refine the solution. The minimization function used in the extraction procedure is reported below for a single experimental measure:

$$E(t, n_i, k_i, i = 1,2, \ldots \ldots, m) = \sqrt{\sum_1^m (M_i - S_i)^2}$$ (2.14)

where M_i is the value measured at the ith wavelength, S_i the one simulated by means of the complex refractive index ($n_i + jk_i$) and the thickness t, while m is the number of frequencies considered. Following eq. (2.14), the overall error function is obtained by summing all the contributions of the individual experimental measurements involved in the extraction.

In this minimization procedure, the optical constants are expressed by theoretical and/or empirical dispersion equations, which have to be chosen appropriately depending on the material type. The Cauchy and Sellmeier equations, for example, are suitable to model transparent materials like silicon oxide and nitride, whereas classic and damped Lorentz oscillators are often used for dielectric materials in the infrared region in order to describe

their vibrational modes at those frequencies. Unlike the Cauchy and Sellmeier equations, the oscillators based models are theoretically consistent with the Kramers-Kronig relation.

In applying this method, the number of oscillators is generally determined from the acquired spectrum, often using its frequency derivative to roughly determine the needed number of oscillators and estimate their frequencies.
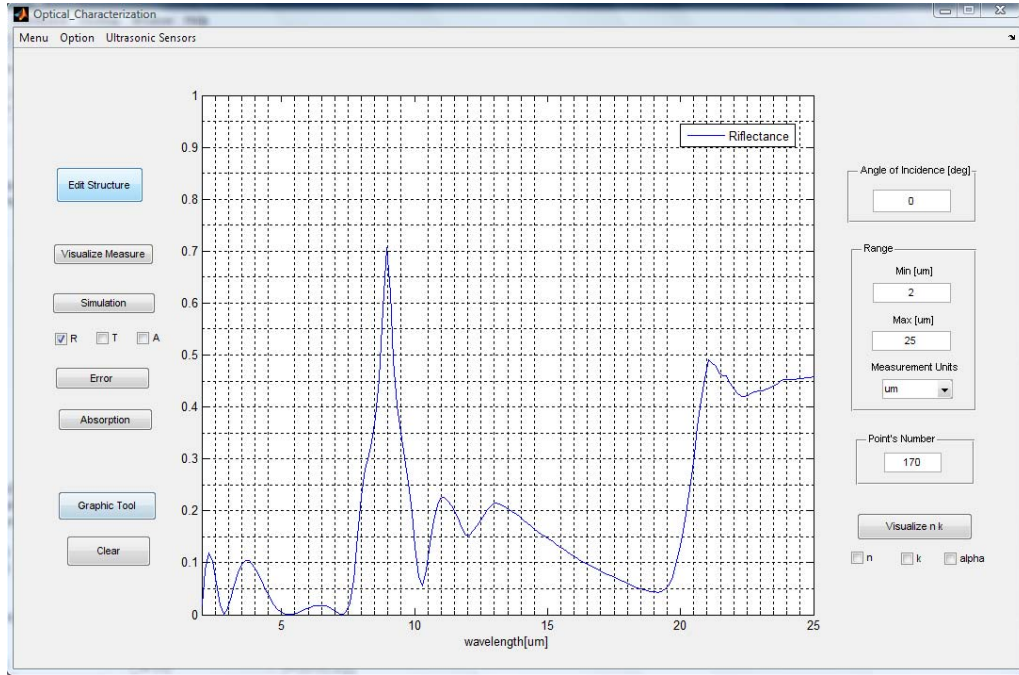
Fig. 2.19. Stand Alone application for the optical characterization of thin layer

For the particular case of amorphous carbon layers, several dispersion relations have been tested and the most interesting results have been obtained by employing the Forouhi-Bloomer equations [20], where the complex index of refraction is derived as a function of photon energy. In this way, the extinction coefficient is rigorously calculated on theoretical bases and the refractive index is subsequently determined by applying the Kramers-Krong analysis. Thanks to these characteristics, the Forouhi-Bloomer model allows for an excellent optical characterization of both amorphous semiconductors and amorphous dielectrics. The model is based on the following equations:

$$k(E) = \frac{A(E - E_g)^2}{E^2 - BE + C}$$

$$n(E) = n(\infty) + \frac{B_0 E + C_0}{E^2 - BE + C}$$

where

$$B_o = \frac{A}{Q}\left(-\frac{B^2}{2} + E_g B - E_g{}^2 + C\right)$$

$$C_o = \frac{A}{Q}\left(\left(E_g{}^2 + C\right)\frac{B}{2} - 2E_g C\right)$$

$$Q = \frac{1}{2}\sqrt{(4C - B)}$$

in which *A*, *B*, *C* and $n(\infty)$ are positive constants that depend on the film characteristics, and E_g is the optical energy band gap. Initially introduced to model the interband region (photon energies higher than band gap), these equations have been also applied to lower energies and good results have been obtained in the characterization of amorphous hydrogenated and unhydrogenated carbon layers [21].

2.6.2 Optical Constants of Amorphous Carbon Layers

The optical properties of carbonized photoresists were estimated by using the Forouhi-Bloomer dispersion relations using the extraction procedure introduced above. The optical constants have been expressed by five variables that, together with the thickness, represent the real parameters of the optimization algorithm, resulting in a fast convergence of the fitting. Several measurements were performed in the visible and infrared frequency ranges by using respectively an UV-Visible Spectrophotometer (Avantes) and a Fourier Transform Infrared Spectrometer (Nicolet). In order to ease optical characterization, the OiR 908-35 photoresist was spun on double side polished wafers that were subsequently cut in quarters before annealing at the four temperatures. As in the process described previously for the patterned structures, the silicon wafer was dipped in a dilute hydrofluoric acid solution before photoresist spinning and, subsequently, carbonization was executed by using the J.I.P.ELEC furnace.

The reflectance measures, obtained on the annealed samples by maintaining the carbonized part of the wafer towards the optical source, are reported in Figs. 2.20 and 2.21 for normal and 30 degrees incident angles respectively.
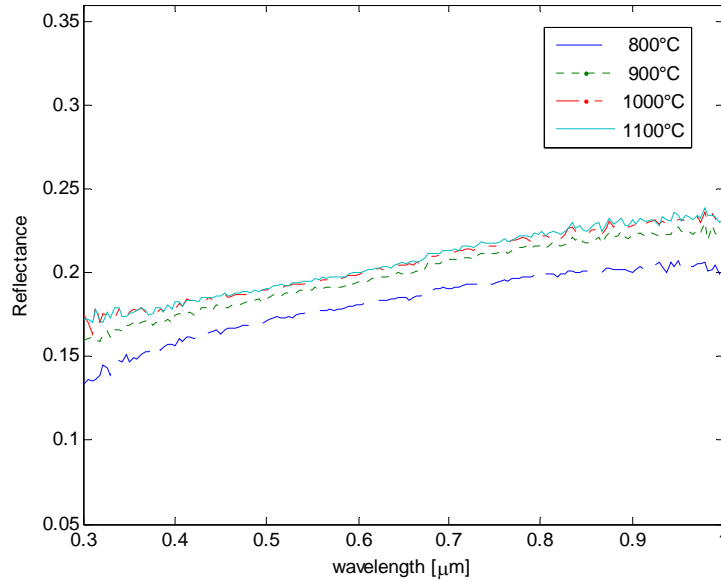
Fig. 2.20. Reflectance measurements realized by Avantes Spectrophotometer
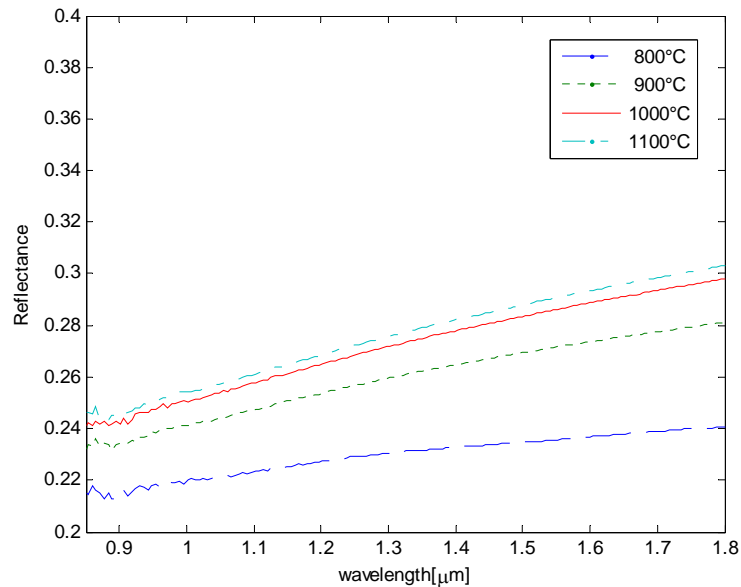
Fig. 2.21. Reflectance measurements realized by Fourier Transform Infrared Spectrometer

As may be seen from the plots, the reflectance increases slightly with the annealing temperature as observed more clearly on the FTIR measurements. Due to the high absorption coefficient of the carbon layer in the frequency range of interest, the transmittance of the double side polished silicon wafer is reduced to zero when the carbon layer is present on one side of it (Fig. 2.22).
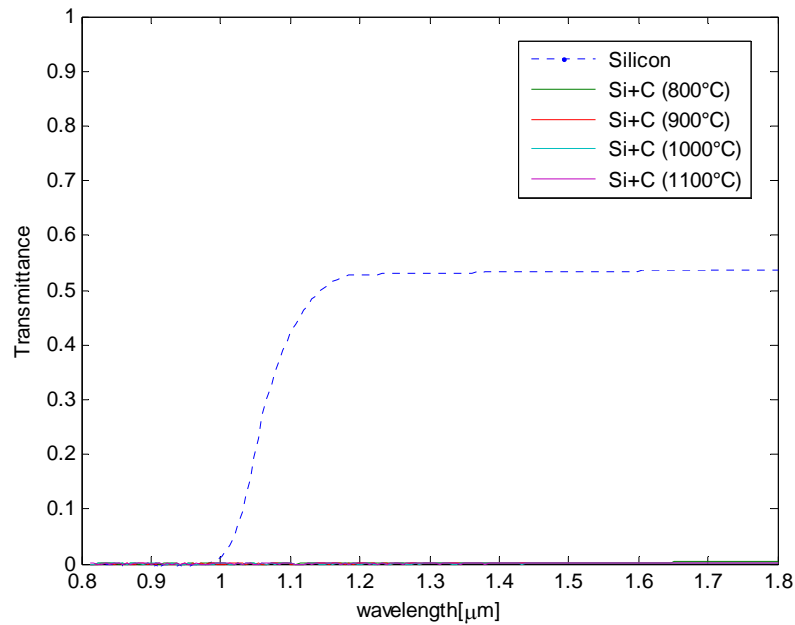
Fig. 2.22. Transmittance measures before and after carbon deposition.

As a consequence of this high absorption, the optical energy is entirely converted into heat for all the layers characterized, independently of the pyrolysis temperature. This should hopefully allow for maximizing the optoacoustic conversion efficiency but, on the other hand, makes the optical characterization of the carbon films more difficult.

In fact, the absence of the interference fringes, or a significant transmission data (due to the strong light absorption in the carbon layer), complicates the determination of refractive index even using several experimental data simultaneously in the extraction, such as reflectance measurements in the visible and near infrared regions performed by irradiating both sides of the samples (silicon and carbon faces). In order to overcome these difficulties and compare the performances of the resists layers pyrolyzed at the four temperatures,   a thinning of the films up to a thickness of roughly 200 nm was realized by RIE oxygen etching operated with a reactive ion etching SENTECH 591 equipment. The RIE oxygen process used in this operation was different than the commonly used oxygen plasma widely employed to strip photoresist in lithographic processes [22], since it was performed on a capacitively coupled RIE apparatus providing directionality and rate control to the etching by a proper DC bias applied to the sample, yielding a carbon etching rate around 110 nm/min. The thinning of carbon layer in oxygen plasma was quite uniform on a wafer quarter and allowed a good control of thickness reduction by time etching.

In Fig. 2.23 some optical images of the carbon surface after a 6 minutes oxygen RIE etching are reported.

Radius = 47,59 µm

Fig. 2.23. Optical images of carbon surface after thinning by oxygen plasma

The thinning procedure led to acceptable results, even if particulate and some isolated spots of about 50 microns diameter were present on the thinned samples. Moreover, the etching rate, was fairly constant on the several samples annealed at the four temperatures proving to be independent of the pyrolysis type realized.

T1	200nm	Mag = 145.95 K X	WD = 4 mm	Signal A = InLens
		EHT = 5.00 kV	Gun Vacuum = 5.75e-010 Torr	Date :3 Feb 2011
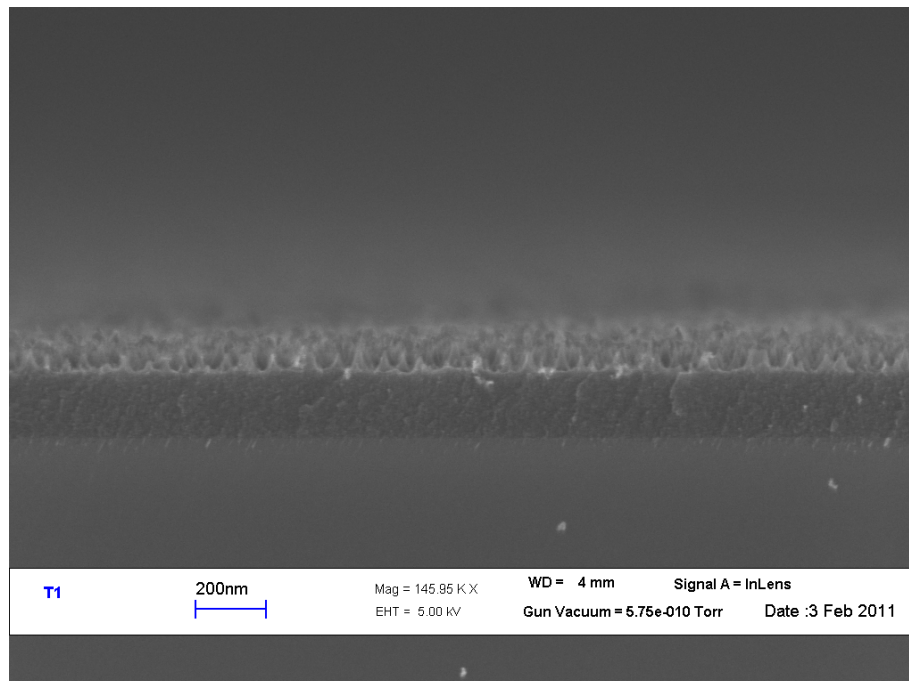
Fig. 2.24. SEM image of carbon film thinned up to 200 nm by reactive ion etching

The SEM image of a slightly inclined cross-section of a carbon layer thinned up to 200 nm, putting into evidence the small superficial roughness induced by the oxygen RIE, is reported in Fig. 2.24.

The thinned samples were optically characterized in the visible and near infrared range in order to determine the optical constants of the carbon layers with better confidence. Some results of the optical measurements are reported in Figs. 2.25, 2.26 and 2.27 (in which the carbon face was kept towards the optical source in the two measures shown on top of the figures).

From these measurements, the refractive indexes of the carbon layers have been derived by using the Forouhi-Bloomer dispersion relation running the fit procedure on four experimental acquisitions. In particular, a transmission measurement was exploited in the NIR (this was necessary since silicon is opaque in the visible frequency range) together with three reflectance measures, one in the visible and two in the near infrared region. In this last frequency range, in fact, the reflectance measurement with the silicon face on the front side can be utilized as well, thanks to the IR transparency of the substrate.
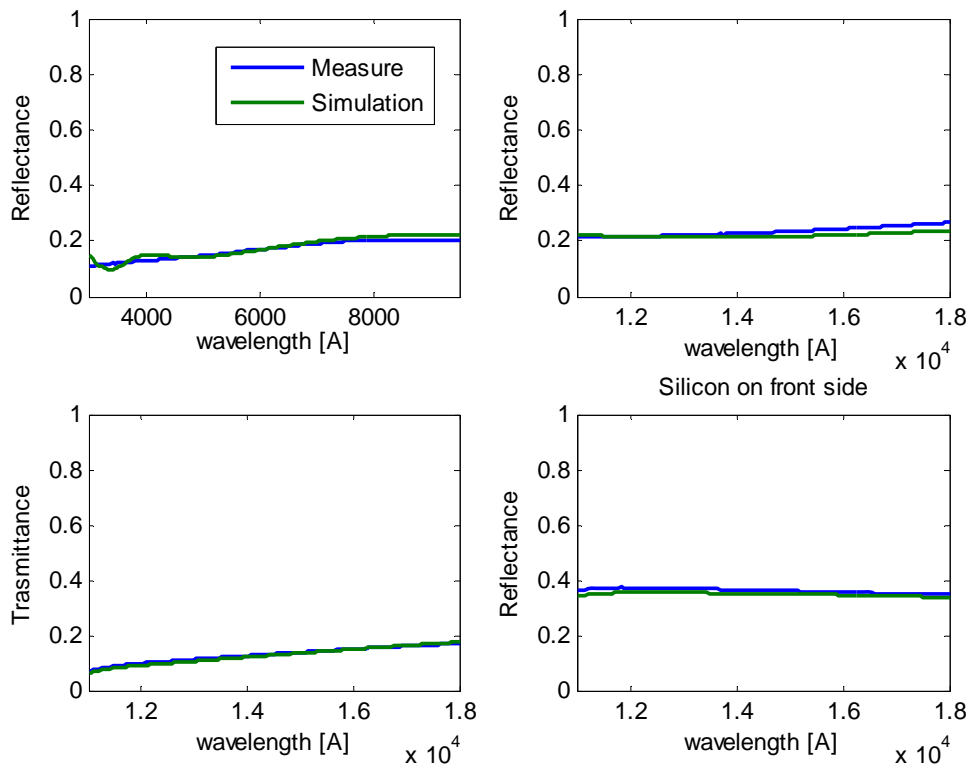
Fig. 2.25. Optical measures realized on carbon layer annealed at 900°C

Unfortunately, the reflectance in the NIR for the carbon layer annealed at 800°C was not measurable due to the too small sample size, and the optical characterization attempted by using only two experimental datasets turned out to be affected by considerable errors and will not be reported here. The fitting obtained for the layers carbonized at 900, 1000 and 1100 °C, on the contrary, was very good, as may be observed by the match between simulated and measured data reported in Figs. 2.25-2.27.
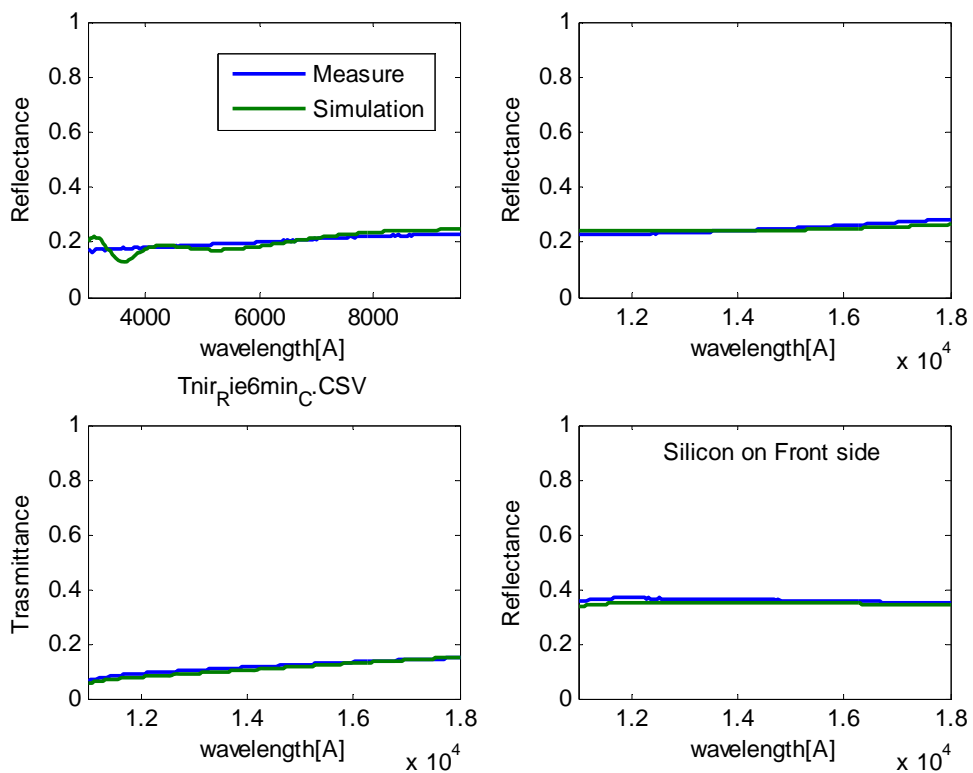
Fig. 2.26. Optical measures realized on carbon layer annealed at 1000°C
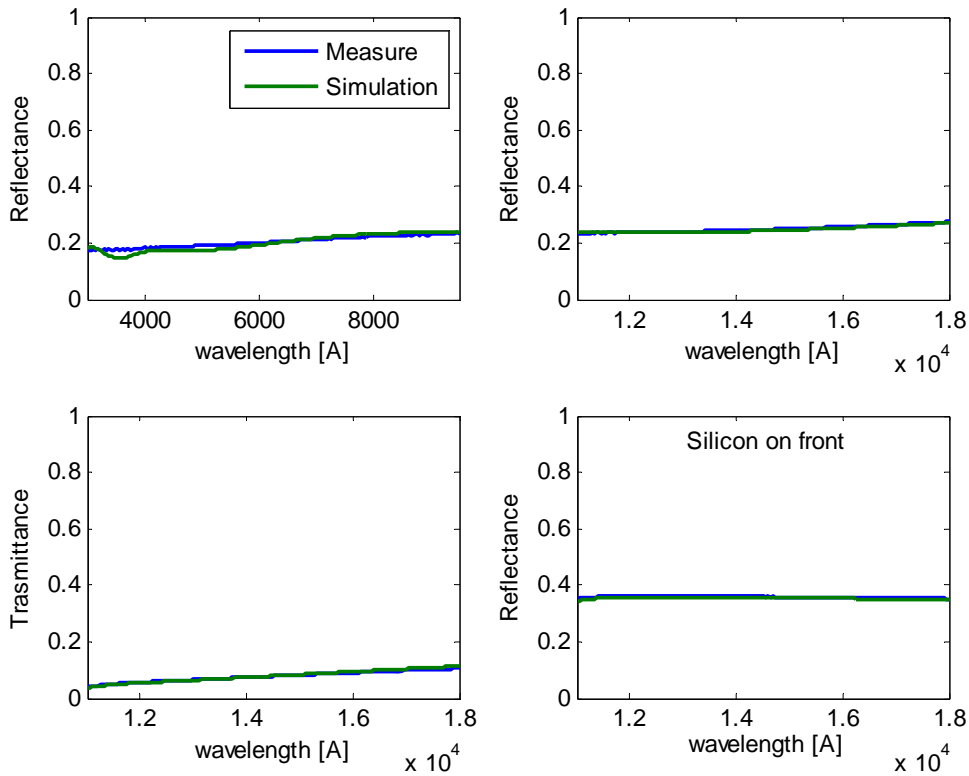
Fig. 2.27. Optical measures realized on carbon annealed at 1100°C

This good match obtained between measurements and simulations for all the annealing temperatures considered provides a good confidence on the extraction of the optical constants for carbon. Actually, an imperfect fitting can be observed only at the highest frequencies, where also the layer roughness should be taken into consideration.

In order to accurately determine the absorption coefficient, the real thickness was earlier measured by SEM for each layer characterized and therefore it was not used as a variable in the fitting procedure. In fact, when high absorption layers are investigated, the independent estimation of thickness represents a remarkable advantage that allows avoiding possible errors in the complex refractive index derivation. The optical constants obtained with the described procedure are finally plotted in Figs. 2.28 and 2.29 in the near infrared region of interest. As may be observed in Fig. 2.29, the absorption coefficient increases with the annealing temperature, reaching its maximum value of $1.3*10^5$ cm^{-1} for the carbon film annealed at 1100° (considering a wavelength of 1.064 μm). The high absorption obtained for

this layer is very promising for the implementation of a high efficiency optoacoustic conversion process.
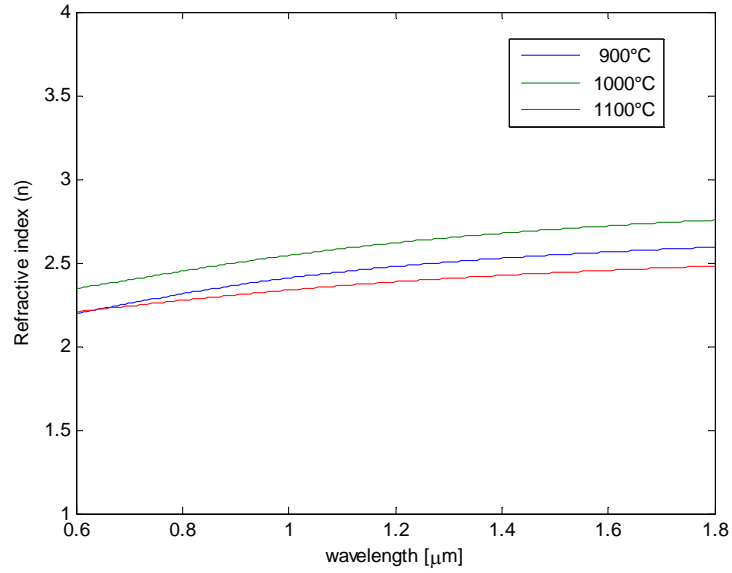
Fig. 2.28. Refractive indexes of carbon films for the several annealing temperatures
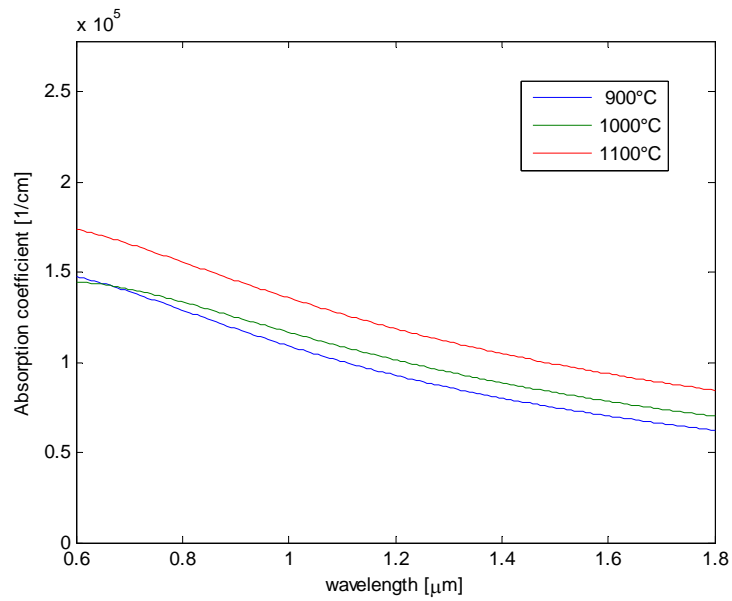
Fig. 2.29. Absorption coefficients of carbon films annealed at the different temperatures

2.6.3   Optical Absorption in the Ultrasonic Emitter

Once derived the optical constants of carbonized resist, the energy absorbed in the MOMS emitter can be calculated as shown in Fig. 2.30, where the absorption, normalized to the incoming optical energy, is plotted as a function of the thickness of the silicon membrane.
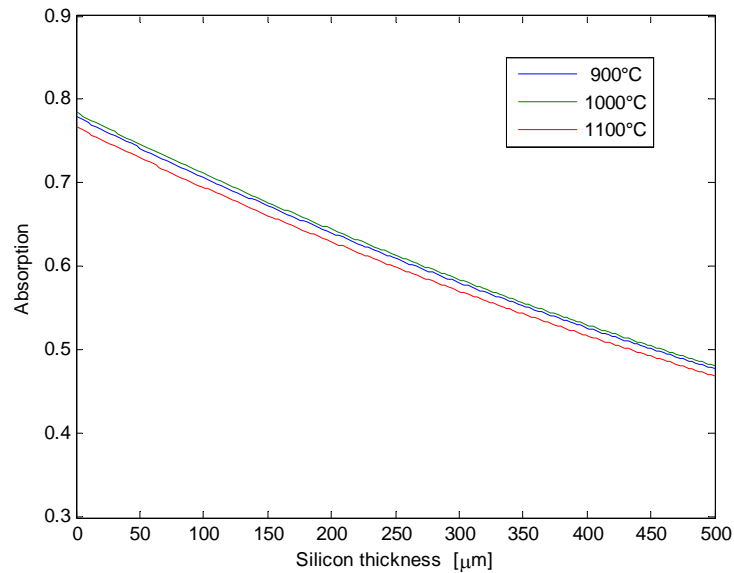
Fig. 2.30. Energy absorbed by 1 µm thick carbon film as a function of silicon membrane thickness (at λ=1.064 µm)

As may be seen, the calculated absorption is quite similar for the various annealing temperatures. In fact, the high absorption coefficient, in the order of 10^5 cm^{-1}, guarantees the full absorption of the laser beam on every carbon film. Furthermore, the lowest refractive index of the resist annealed at the maximum temperature results in the lowest absorption, due to high difference of refractive index at the silicon-carbon interface. The effect of the different absorption coefficient of the several films can be appreciated in Fig. 2.31, where the optical absorption of emitters realized on a 100 µm thick silicon membrane is plotted as a function of carbon thickness. As may be observed, the carbon film annealed at the maximum temperature reaches the plateau earlier due to its more pronounced absorption. Moreover, the effect of optical interference is visible in the plots for small values of the thickness, resulting in a less smooth shape of the curves.
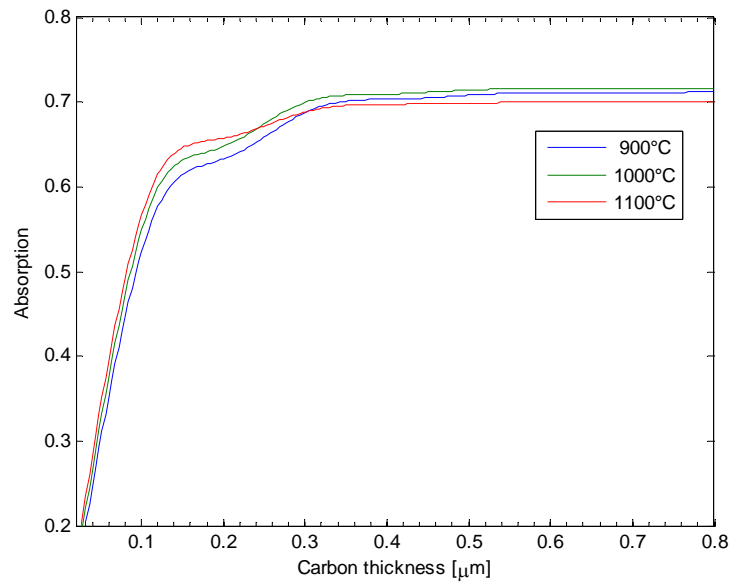
Fig.2.31. Absorbed optical energy by carbon against thickness

It is worth noting that, according to the simulation results reported in Fig. 2.30, the thinning of the silicon membrane up to 100 µm results approximately in a 50% increase of the absorbed energy with respect to the case of a bulk substrate (with thickness around 500 µm). However since the nanosecond pulsed lasers provide a coherence length in the order of few millimeters, a correct calculation of the absorbed energy should take into account the effect of optical interference in the silicon membrane.

The result of an optical simulation executed considering this phenomenon is reported in Fig. 2.32. By examining the figure, it is clear that the trend of Fig 2.30 can be only employed to derive the average power absorbed by the carbon layer, mediated on the envelope of the interference pattern of Fig. 2.32. However, this theoretical analysis predicts that the exact power reaching the absorbing layer from the silicon membrane is strongly affected by its thickness (even by variations in the order of hundreds of nanometers), and should in theory be widely variable from device to device due to process parameter spread.
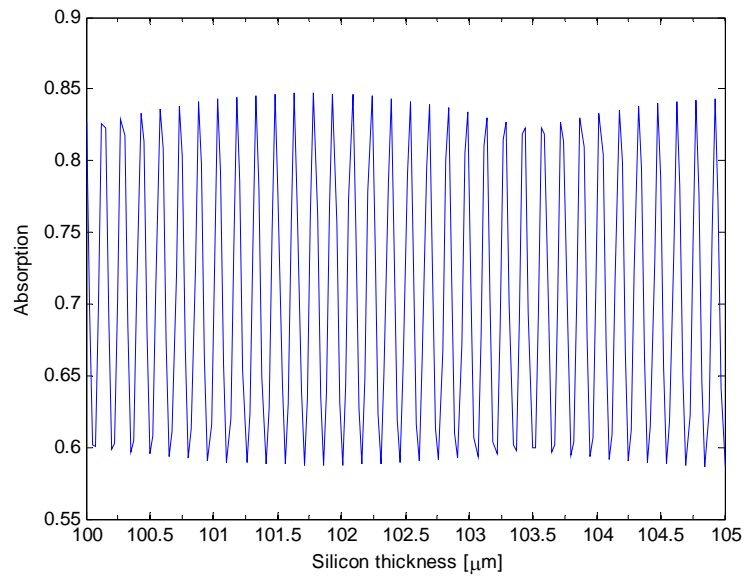
Fig. 2.32 Energy absorbed by carbon film considering the coherence of the laser beam at 1.064 μm wavelength (temperature of carbon annealing of 900°C)

However, it must be pointed out that in reality the thickness of the silicon membrane will be actually not constant in the hundreds of nanometers range even within the core of the fiber used to deliver the laser up to the emitting layer, because of the etching profile, which is not absolutely flat at its bottom (actually, multimode fibers are often used to this purpose, whose core diameter typically varies in the range 200-600 μm). As a consequence of that, the laser light transmission within the fiber diameter will be probably averaged yielding an overall transmitted power that will coincide with a short-range average of the plot reported in Fig. 2.32, yielding a smaller variation of the optical power absorption from one device to another.

Differently than the case discussed above, for the emitters realized on dielectric membrane a more accurate calculation of the absorbed energy is possible. In fact, due to the negligible attenuation of the laser beam in the dielectric multistack and smaller refractive index difference between the optical fiber and the membrane, the emitters on dielectric membrane theoretically provide the optimal optical absorption. However their performances are slightly worsened by the polysilicon layer deposited on top of the membrane to enhance carbon adhesion, yielding to 65% absorption of the incoming power.

2.6.4   Calculation of the Transient Temperature Profile in the MOMS Emitters

The values of the complex refractive index of the films and the related calculations of the absorbed optical power, obtained as previously described, can be exploited to derive the transient temperature profile in the emitter during its operation as a thermoelastic emitter. In fact, as seen in equation (2.2), the *f(t)* function can be employed to model the time shape of the laser beam. In Fig. 2.33, a laser pulse calculated by choosing a rise time of 0.3 ns is shown.
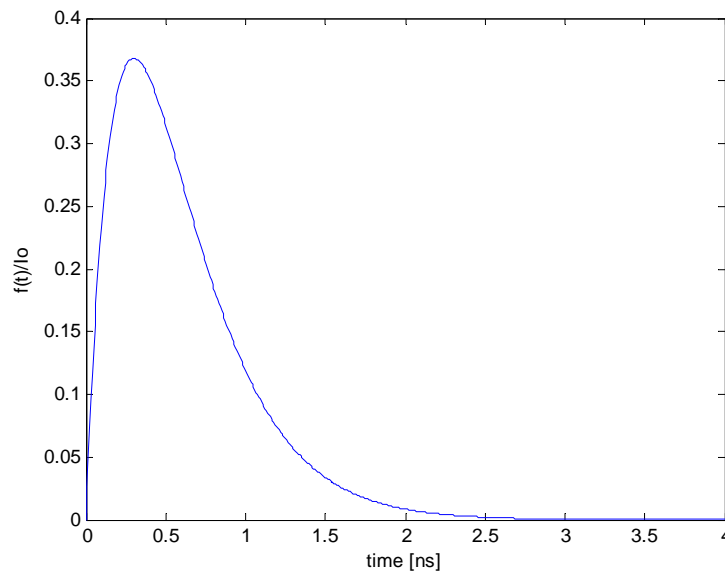
Fig. 2.33 Temporal shape of laser beam simulated by f(t)

The chosen time allows for having a full width at half maximum of about 800 ns that well approximates the typical temporal shape of nanosecond pulsed lasers. Furthermore an optical intensity I_0 of 10^{11} W/m^2 can be reasonably used in the simulations since this values is compatible with the power provided by the widely used pulsed lasers with Nd:YAG laser sources. In order to calculate the temperature profile, the 3D heat equation is solved in a two-dimensional domain by taking advantage of the cylindrical symmetry of the simulation domain (Fig. 2.34). In the chosen reference frame, it is assumed that the laser beam travels along the vertical *z*-axis while *r* is the radial coordinate (r=0 symmetry axis). The temperature distributions, computed by the finite element method with the COMSOL Multiphysics package, are finally depicted at two significant simulation times in Figs. 2.35 and 2.36 for two emitters respectively realized on a silicon and on a dielectric membrane.
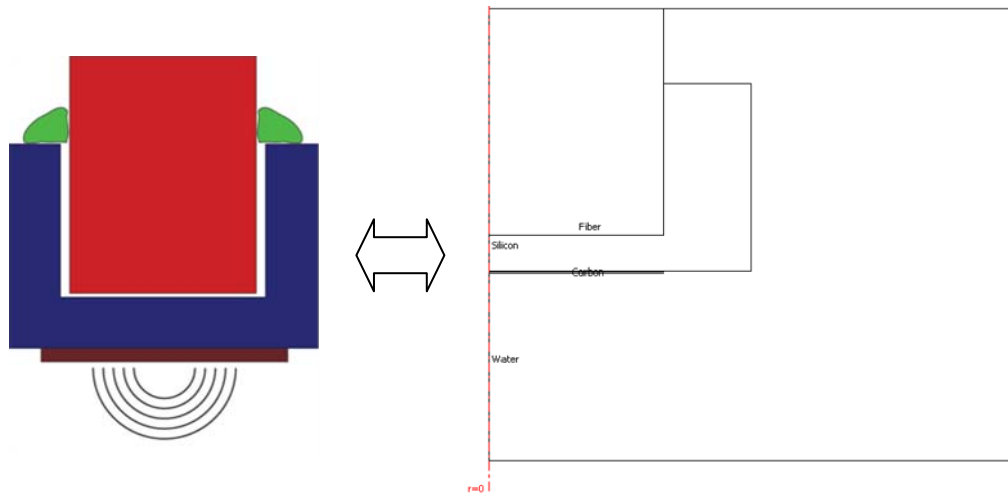
Fig. 2.34. Emitter on silicon membrane and equivalent 2-D model by taking advantage of cylindrical symmetry
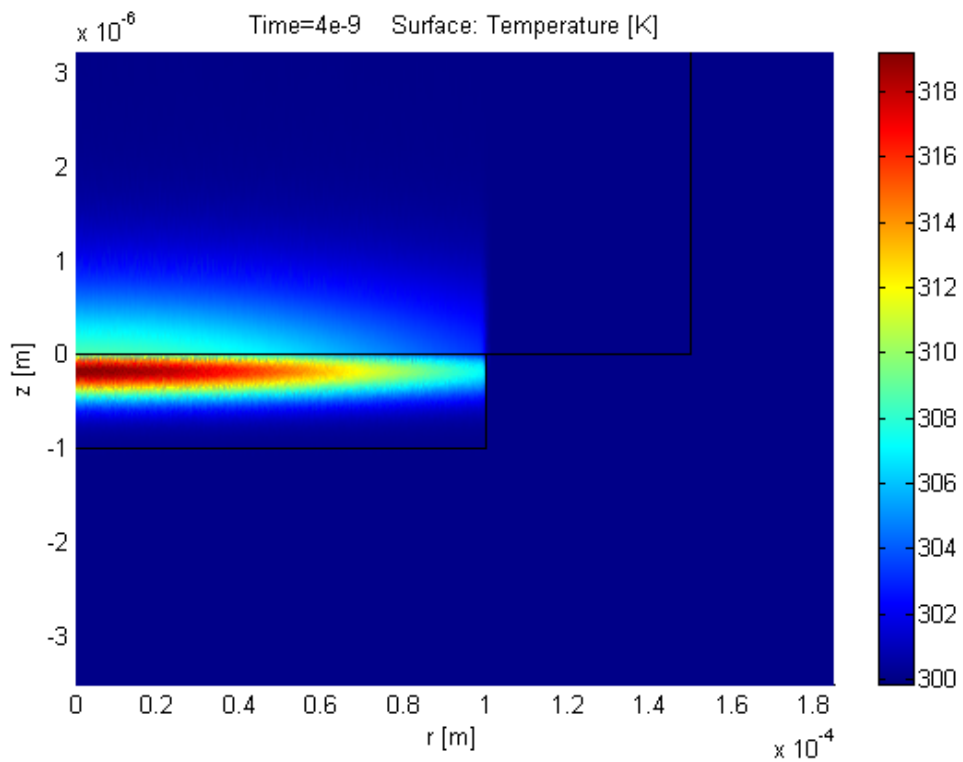
Fig.2.35. Temperature distribution in a emitter realized on silicon, calculated by element finite simulation

The geometric parameters employed in the simulation are 1 μm thick carbon film, 100 μm fiber radius and a width of 50 μm for the lateral silicon wall. The silicon substrate is considered 500 μm thick. The presence of thin nitride and polysilicon layers has been neglected in the heat equation solution of the emitter on the dielectric membrane.
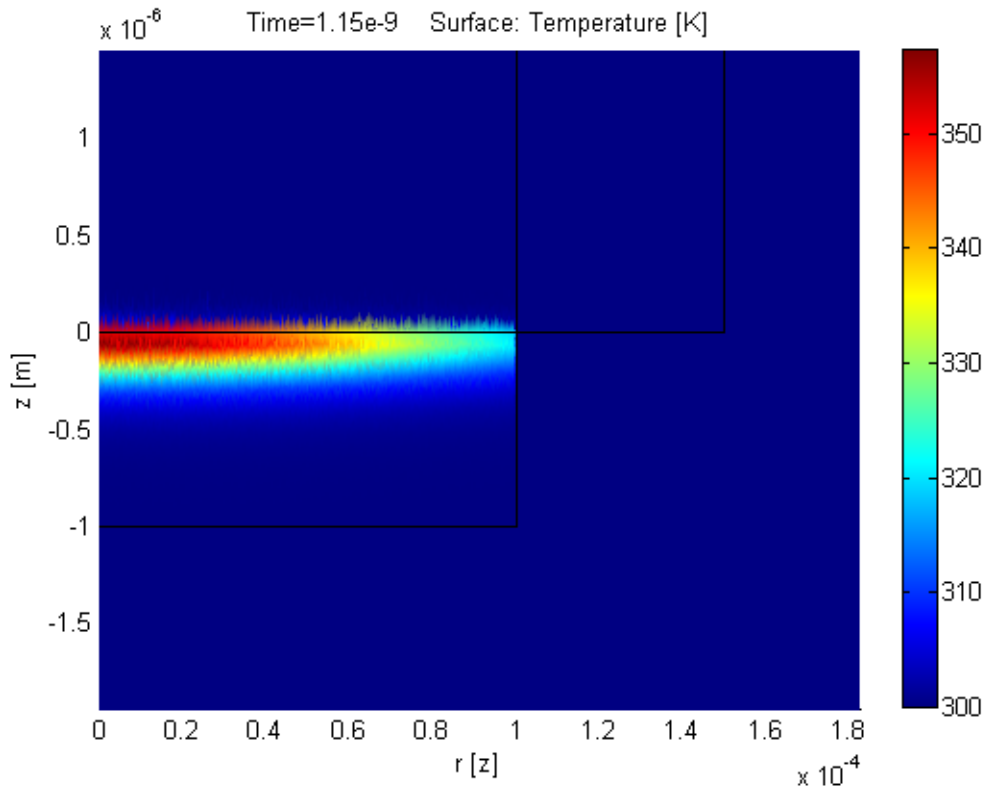
Fig. 2.36. Temperature distribution in an emitter realized on dielectric membrane

From the simulations, it is clear that the presence of the thick silicon membrane under the carbon emitter strongly affects the temperature profile, reducing the maximum temperature reachable because of its high thermal conductance. The maximum calculated temperatures reached within the carbon layer during the transient heating are plotted as a function of time for the two different MOMS based emitters in Fig.2.37. As may be observed, the ultrasonic source realized on dielectric membrane shows a temperature peak of roughly 350 K against the one of 335 K of the emitter on silicon. As a consequence of that, the silicon membrane does not seem to provide a larger bandwidth, despite the higher cooling speed of the film provided by its presence, because of the lower temperature peak reached.
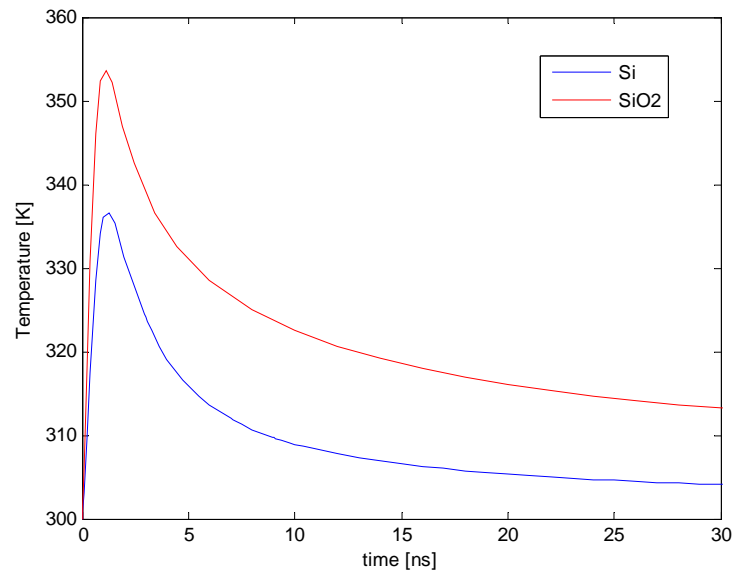
Fig. 2.37. Temperatures against the time for the emitters realized on silicon and dielectric membranes (calculated in the respective maximum value points)

As can be clearly seen in Fig. 2.38, where the normalized Fourier transform of the temperature time dependence are shown, the spectrum of the emitter on dielectric membrane is characterized by large amplitude at high frequencies. Moreover, in order to maximize the opto-acoustic generation, the simulation results suggest that the thickness of carbon film could be further reduced up to few hundreds of nanometers, for example by using the RIE oxygen etching described previously.

It must be said, however, that the discussed simulations only allow qualitative evaluations, such as the comparison of the expected performances of the two main emitter structures designed. It has to be noted, in fact, that the calculated temperature distributions are dependent on the thermal conductivity and the heat capacity of the carbon layer. Therefore, in order to achieve a predictive model, the thermal properties of the carbon film should be experimentally determined possibly by fabricating proper test structures to measure these parameters.

On the contrary, in the simulations presented above, parameters referred to amorphous carbon layers taken from the literature have been utilized, as shown in the table below:

Parameter	Value	Measure Unit
Carbon Absorption coefficient	10^7	1/m
Carbon thermal conductivity	6	W/(m·K)
Carbon density	2000	Kg/m^3
Heat capacity	500	J/(Kg·K)
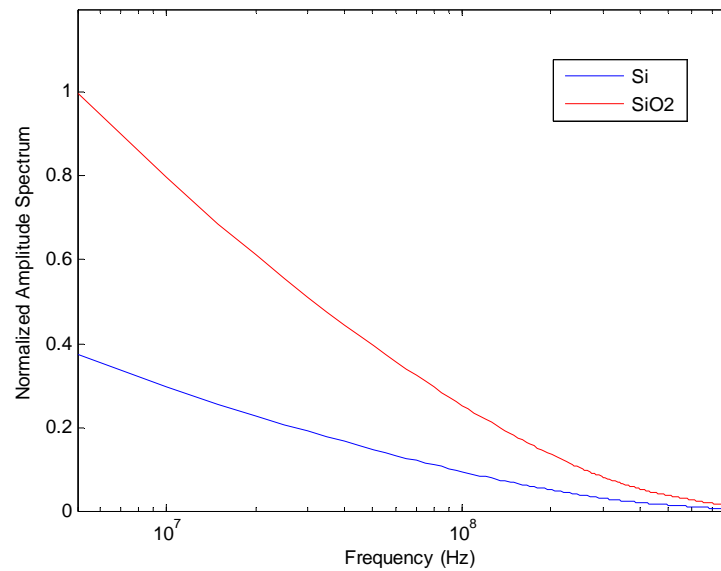
Fig. 2.38. Normalized Fourier Transformers of the temperature functions reported above

2.7 Acoustic Characterization

Once completed the fabrication process of the first prototypes of ultrasonic generators, a preliminary acoustic characterization was realized employing an Nd:YAG (PowerChipNanoLaser) for irradiating the emitters. This Q-switched Diode-Pumped Solid-State Laser has minimum and maximum pulse energies of 50 and 80 µJ respectively, with an average power of 50 mW at its maximum repetition rate of 1 kHz. The pulse width at Full Width Half Maximum (FWHM) is less than 500 ps. These Nd:YAG lasers present ideal characteristics for optoacoustic generation and consequently are widely used in this application. Actually, most of the experimental results presented in the last decades employ this kind of laser, taking advantage of the short pulse duration which permits wideband emission. Furthermore the emitted optical power is generally adequate to assure good

ultrasonic generation amplitude without damaging the emitter layer. Ultrasonic signals with bandwidth of tens of Megahertz have been generated by using thin absorbing layers and Nd:YAG pulsed lasers [2] [23] [24].

The experimental setup, used for the characterization of the MOMS devices, is shown in Fig. 2.39.
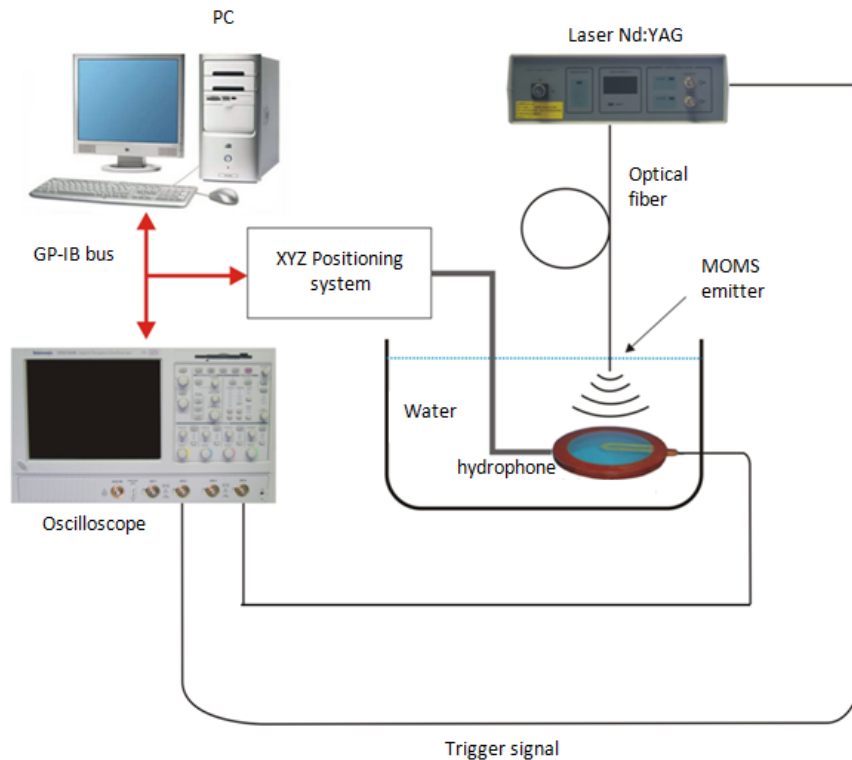
Fig. 2.39. Measurement setup for the opto-acoustic generation

In the setup, a PVDF membrane hydrophone (Marconi 699/1/00002/200) has been utilized to measure the generated ultrasounds, using a TDS Tektronix oscilloscope to acquire the sensor signal. All the presented measurements have been carried out in liquid environment, keeping both the ultrasonic source and the detector immersed in deionized water. A large multimode fiber, with roughly 630 and 600 μm respectively cladding and core diameters, was used for guiding the laser beam to the optoacoustic transducer in these first tests. A laser/optical fiber coupler was utilized for interfacing the laser output with the fiber, which, unfortunately, led to a considerable optical power loss.

In the measured prototype, the carbon layer was obtained with an annealing temperature of 800°C, yielding a thickness of roughly 800 nm for the pattern geometry and deposited on a silicon membrane as described previously.

The acoustic field was evaluated by measuring the ultrasonic signal emitted by the optoacoustic source in different positions using a computer controlled xyz stage to shift the detector from on measurement to another. In this way, the 3D distribution of the acoustic field generated by the carbon emitter could be estimated. In Fig. 2.40, a longitudinal section of the acoustic field generated by the optoacoustic source acquired on a plane approximately intersecting the axis of symmetry of the MOMS is shown in colour scale. As may be observed, the acoustic field intensity decreases by 90% from 2 to 16 mm from the source. In Fig. 2.41, a transverse section of the acoustic field measured at a distance of 2 mm from the emitter is reported.

The results of the acoustic characterization proved that acoustic pressures in the range of 1 MPa can be obtained with the MOMS emitter in its near-field region, using a laser pulse energy of 50 μJ with 500 ps FWHM. Moreover, the acoustic field observed turned out to be limited within a cylindrical region of space having a radius of roughly 0.75 mm measured from the axis of symmetry of the MOMS. In this respect, it is important to observe that the hydrophone used in the characterization had a 0.8 mm pixel diameter, and consequently was not completely suited to measure an acoustic field characterized by rapid spatial variations like the one of the optoacoustic source. In fact, every measurement point accounts for the pressure applied on the relatively large active area of the detector, most probably resulting in some imprecision in the estimation of the actual spatial distribution. In addition, it is expected that field components at higher frequencies are more attenuated than the low frequency ones by the unavoidable spatial average effect performed by the detector on its 0.8 mm pixel, possibly leading to additional attenuation of the signal amplitude and limitation of the measured emission band (besides the native cut-off of the piezoelectric detector, whose central frequency is 30 MHz).   These limitations of the measurement setup did not allow a complete characterization of the MOMS ultrasonic source at higher frequencies, for which a wideband miniaturized transducer should be utilized for an exhaustive characterization of the fabricated. Then, the amplitude spectrum of the acoustic wave detected at 2 mm, is finally reported in Fig. 2.42.   The intensity reduction at high frequencies is probably due to the limited wideband of the sensor utilized in the acquisition.

In fact the cut off frequency of membrane hydrophone is roughly 60 MHz (but its sensitivity decreases sensibly already for lower frequencies), corresponding with the profile observable in the figure. The obtained result is very interesting because demonstrates that using a nanosecond pulsed laser with emitters realized with carbonized resist is possible to generate ultrasounds of 50 MHz bandwidth and beyond.

Furthermore, the measurements demonstrated undoubtedly that the pressure emitted by the MOMS source developed is several orders of magnitude higher than pressure generated irradiating a metallic film [13] and comparable in intensity with the best results reported in the literature for comparable emitters realized on bulk substrates [25]. Moreover, the high thickness control of the carbon film, obtained by the fabrication process based on pyrolysis of photoresist, assures a sensible increase of the acoustic pressure emitted, compared to previously reported results obtained by irradiating a thicker absorbing target made of graphite powder and epoxy resin [13].
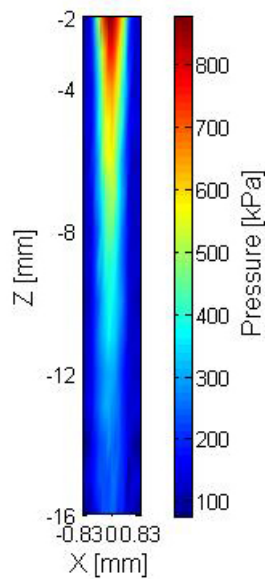
Fig. 2.40. Longitudinal section of the acoustic field from 2 to 16 mm from the source, acquired with a membrane hydrophone.
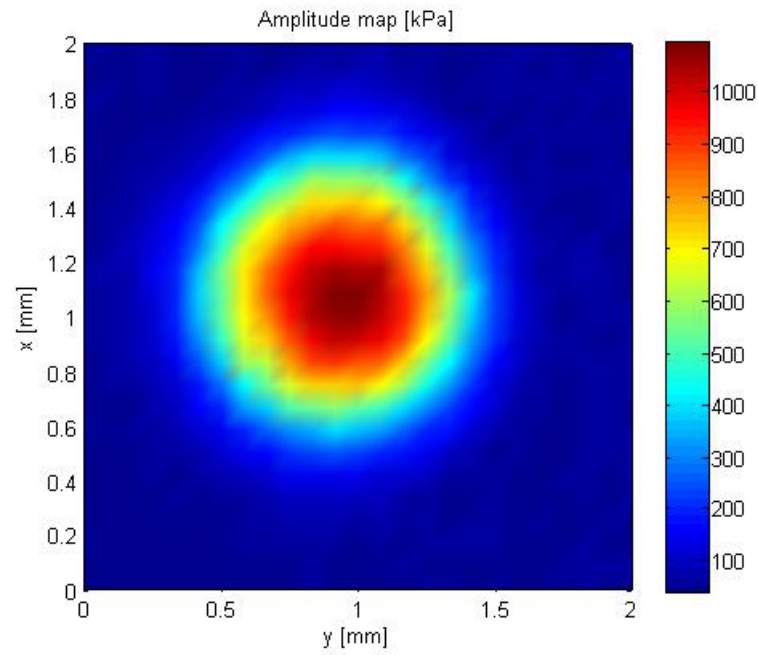
Fig. 2.41. Transverse section of the acoustic field at a distance of 2 mm from the source, acquired with a membrane hydrophone
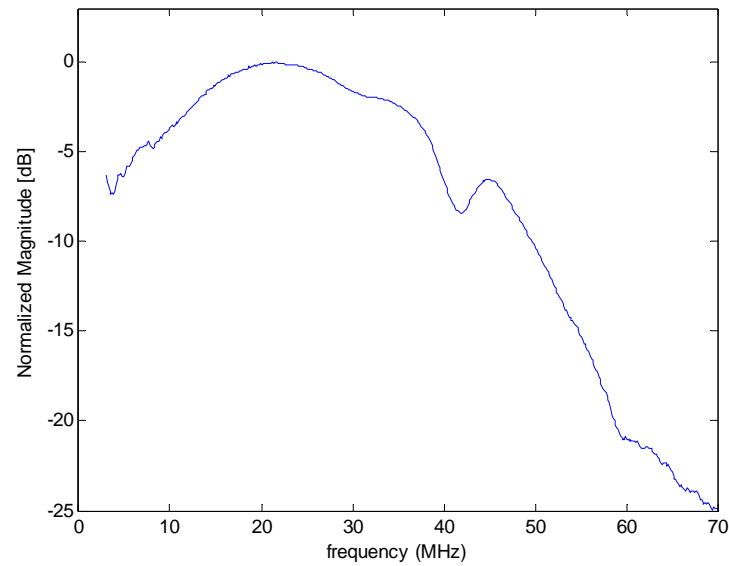
Fig.2.42. Normalized amplitude spectrum of laser generated ultrasound

As far as possible biomedical applications of the developed technology are concerned, it must be pointed out that the acoustic pressures generated by an individual piezoelectric

transducer of the type typically employed in diagnostic imaging are comparable with the opto-acoustic signal measured [26]. Furthermore, if higher pressures were required for some application, it must be considered that the modulation of the intensity should be possible by utilizing a more powerful laser source as long as the ablation threshold of the carbon layer is not crossed. In order to obtain higher emission intensity without changing the laser pulse energy, the emitters realized on dielectric membrane could also be used, as the simulation results suggest.

Bibliography

[1] R. White, "Generation of Elastic Waves by Transient Surface Heating", *Journal of Applied Physics*, vol. 34, no. 12, pp. 3559-3567, 1963.

[2] T. Buma, M. Spisar, and M. O'Donnell, "High-frequency ultrasound array element using thermoelastic expansion in an elastomeric film", *Applied Physics Letters*, vol. 79, no. 4, pp. 548-550, 2001.

[3] Y. Haga, M. Fujita, K. Nakamura, C. J. Kim, and M. Esashi, "Batch fabrication of intravascular forward-looking ultrasonic probe", *Sensors and Actuators A: Physical*, vol. 104, no. 1, pp. 40-43, 2003.

[4] S. Hu and L. V. Wang, "Photoacoustic imaging and characterization of the microvasculature", *Journal of Biomedical Optics*, vol. 15, no. 1, 2010.

[5] L.R.F. Rose, "Point source representation for laser generated", *J. Acoust. Soc. Amer.*, vol. 75, no. 3, pp. 723–732, 1984.

[6] A. E. Green and K. A. Lindsay, "Thermoelasticity", *Journal of Elasticity*, vol. 2, no. 1, 1972.

[7] D. S. Chandrasekharaiah and K. S. Srinath, "Thermoelastic waves without energy dissipation in an unbounded body with a spherical cavity", *International Journal of Mathematics and Mathematical Sciences*, vol. 23, no. 8, pp. 555-562, 2000.

[8] E. Marín, J. Marín, and R. Hechavarría, "Hyperbolic heat diffusion in photothermal experiments with solids", *J. Phys. IV France* , vol. 125, pp. 365 - 368, 2005.

[9] I. Arias and J.D. Achenbach, "Thermoelastic generation of ultrasound by line-focused laser irradiation", *International Journal of Solids and Structures*, vol. 40, no. 25, pp. 6917–6935, 2003.

[10] A.E. Green and P.M. Nagdhi, "Thermoelasticity without energy dissipation", *Journal of Elasticity*, vol. 31, pp. 189-208, 1993.

[11] S. K. Roychoudhuri and S. Mukhopadhyay, "Effect of rotation and relaxation times on plane waves in generalized thermo-visco-elasticity", *The International Journal of Mathematics and Mathematical Sciences* , vol. 23, no. 7, pp. 497-505, 2000.

[12] G. Arfken, "Helmholtz's Theorem", in *Mathematical Methods for Physicists, 3rd ed.*, 1985, pp. 78-84.

[13] E. Biagi, F. Margheri, and D. Menichelli, "Efficient Laser-Ultrasound Generation by Using Heavily Absorbing Films as Targets", *IEEE Transactions on Ultrasonics, Ferroelectrics, and Frequency Control*, vol. 48, no. 6, pp. 1669-1680, 2001.

[14] S. Ranganathan, R. McCreery, S. M. Majji, and M. J. Madou, "Photoresist-Derived Carbon for Microelectromechanical Systems and Electrochemical Applications", *Journal of The Electrochemical Society*, vol. 147, no. 1, pp. 277-282, 2000.

[15] B.Y. Park, L. Taherabadi, C. Wang, J. Zoval, and M. J. Madou, "Electrical Properties and Shrinkage of Carbonized Photoresist Films and the Implications for Carbon Microelectromechanical Systems Devices in Conductive Media", *J. Electrochem. Soc.*, vol. 152, no. 12, pp. J136-J143 , 2005.

[16] R. E. Denton, R. D. Campbell, and S. G. Tomlin, "The determination of the optical constants of thin films from measurements of reflectance and transmittance at normal incidence", *Journal of Physics D: Applied Physics* , vol. 5, no. 4, 1972.

[17] C. Manifacier, J. Gasiot, and J. P. Fillard, "A simple method for the determination of the optical constants n, k and the thickness of a weakly absorbing thin film", *Journal of*

Physics E: Scientific Instruments , vol. 9, no. 11, 1976.

[18] D. M. Roessler, "Kramers-Kronig analysis of reflection data", *British Journal of Applied Physics* , vol. 16, no. 11, 1965.

[19] P.-O. Nilsson, "Determination of optical constants from intensity measurements at normal incidence", *Applied Optics*, vol. 7, no. 3, pp. 435-442, 1968.

[20] W. A. McGahan, T. Makovicka, J. Hale, and J. A. Woollam, "Modified Forouhi and Bloomer dispersion model for the optical constants of amorphous hydrogenated carbon thin films", *Thin Solid Films*, vol. 253, no. 1-2, pp. 57-61, 1994.

[21] G. Compagnini, "Optical constants of hydrogenated and unhydrogenated amorphous carbon in the 0.5-12-eV range", *Applied Optics*, vol. 33, no. 31, pp. 7377-7381 , 1994.

[22] M. A. Hartney, D. W. Hess, and D. S. Soane, "Oxygen plasma etching for resist stripping and multilayer lithography", *Journal of Vacuum Science & Technology B: Microelectronics and Nanometer Structures*, vol. 7, no. 1, pp. 1-13, 1989.

[23] A. J. A. Bruinsma and J. A. Vogel, "Ultrasonic noncontact inspection system with optical fiber methods", *Applied Optics*, vol. 27, no. 22, pp. 4690-4695, 1988.

[24] P. A. Fomitchov, A. K. Kromine, and S. Krishnaswamy, "Photoacoustic Probes for Nondestructive Testing and Biomedical Applications", *Applied Optics*, vol. 41, no. 22, pp. 4451-4459 , 2002.

[25] Y. Hou, S. Ashkenazi, S. Huang, and M. O'Donnell, "Improvements in optical generation of high-frequency ultrasound", *IEEE Transactions on Ultrasonics, Ferroelectrics, and Frequency Control*, vol. 54, no. 3, 2007.

[26] F. P. Branca, *Fondamenti di Ingegneria clinica* , 2nd ed., 2008.

Interferometric Detection of Ultrasounds: Design and Fabrication of Optoacoustic Receivers

3

3.1 Introduction

The increasing interest concerning the use of acoustic waves, both generated by optical absorption of short laser pulses in biological tissues or in highly absorbing thin layers for different applications, has recently made the development of ultrasonic receivers capable of detecting wideband ultrasonic signals a relevant research theme [1] [2] [3] . The various issues involved in the design and fabrication of extrinsic Fabry-Perot interferometers on optical fiber by means of appropriate silicon microstructures, will be here discussed in depth. In order to do that, the physical phenomena related to opto-acoustic interferometric detection will be analyzed, by deriving optical and acoustic models from basic theory and performing measurements on proper test structures in order to estimate the relevant material parameters. By taking advantage of microfabrication techniques, the realization of highly miniaturized MOMS detectors will be demonstrated, opening a door to possible endoscopic applications even based on arrays of ultrasonic receivers. The presented results might help overcome the limitations that still exist to date in the applicability of high frequency acoustic waves in diagnostic tools, because of the strong attenuation of such waves in biological tissues and the lack of effective miniaturization techniques for high frequency ultrasonic arrays.

The MOMS-based Fabry-Perot interferometers presented will be mainly realized on a dielectric membrane similar to the one described in Chapter 2 and employed in some of the emitters (namely the multilayer composed by thermal silicon dioxide, silicon nitride and

LTO), which helps maximising the amount of incoming light on the interferometric structure. As described for the emitters, the thicknesses in the multilayer have been accurately chosen in order to compensate the tensile and compressive stresses of the individual layers, assuring membranes with high mechanical stability and stiffness.

The process flow adopted here, quite similarly to the case of the ultrasonic emitters described in the previous chapter, relies on a double depth silicon etching, and also allows the fabrication of ultrasound detectors on silicon membranes, which are expected to have a larger optical power loss for the lower transmittance of fibre-silicon-interferometer structure, but higher stiffness and mechanical robustness as well, and consequently have been considered of concern for the developed technology.
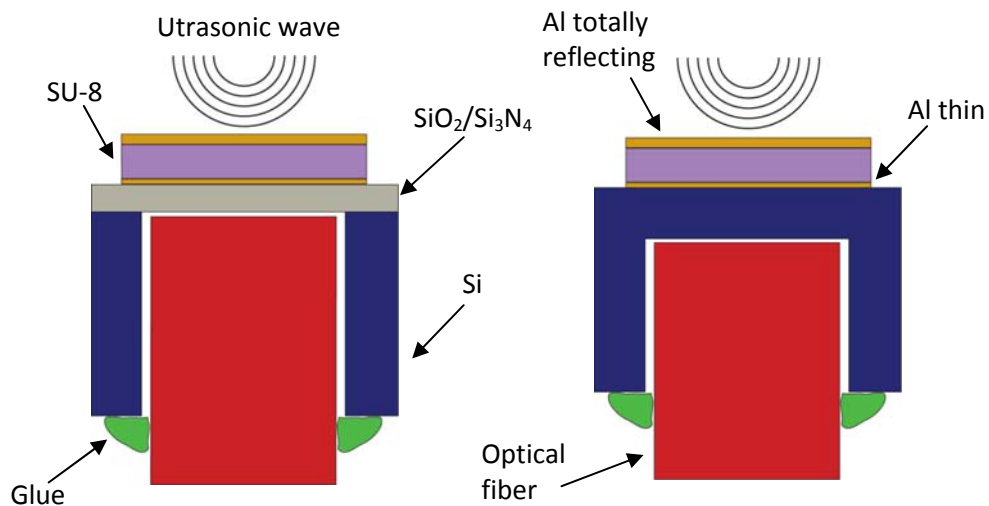
Fig. 3.1. Interferometers on dielectric (left) and silicon membranes (right)

3.2 Theory of Interferometric Detection

3.2.1 Acoustic Modelling

The MOMS-based ultrasonic receivers have been designed based on the well-known principle which allows measuring the pressure applied by an acoustic wave through a Fabry-Perot interferometer (Fig. 3.1). A polymer film, characterized by low Young's modulus, is coated with a very thin Al layer having a non negligible transmittance of light at the desired wavelength on one side and with a thicker, totally reflective one on its opposite face. In

order to measure the thickness variation of the polymeric spacer in the presence of ultrasound waves, the interferometric cavity is interrogated with a laser beam and the reflected power measured by a photodiode. In this way, when an acoustic wave hits the structure, the reflected intensity is modulated by interference effects and the spectrum of the incoming acoustic waves can be measured with the photodiode [4] [5].

The sensitivity, e.g. the conversion efficiency of acoustic pressure in optical intensity, can be defined as:

$$S = \frac{dI_R}{dP} \tag{3.1}$$

where I_R is the reflected intensity and P the incident acoustic pressure. Indicating with β the optical phase shift throughout the cavity, eq. (3.1) can be rewritten bringing into relief the optical and acoustic parts:

$$S = S_{opt.} \cdot S_{aco.} \tag{3.2}$$

$$S_{opt.} = \frac{dI_R}{d\beta} \qquad S_{aco.} = \frac{d\beta}{dP}$$

As may be seen from eq. (3.2), the sensitivity can be maximized by designing an interferometer which assures a strong variation of the reflected intensity with the phase shift and a considerable thickness modulation when an acoustic pressure is applied. The acoustic behaviour of the sensor can be derived by considering the simplified model depicted in Fig. 3.2.
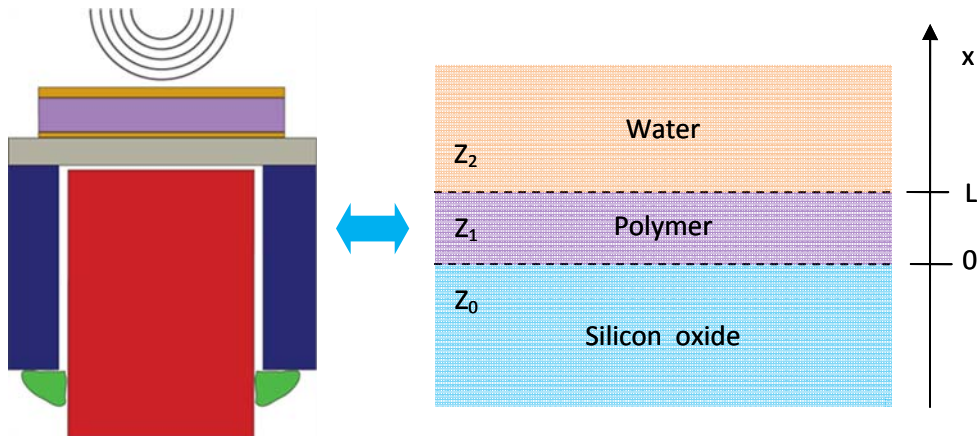
Fig. 3.2. View of MOMS based ultrasonic detector and acoustic schematization

At the ultrasonic frequencies of operation for the MOMS detectors and considering the designed thicknesses, the phase shifts in the metallizations can be considered negligible and, consequently, the pressure applied on the interferometer can be calculated without accounting for the presence of the two thin aluminium layers. Similarly, the effect of silicon nitride can be ignored without significantly affecting the model validity.

Considering the model schematically represented in the figure, the polymer thickness variation due to the incident pressure can be written as:

$$dl = \frac{1}{E} \int_0^L P \, dx \tag{3.3}$$

where E is the Young's modulus and P is the acoustic pressure in the sensing film, whose thickness is L. This resulting pressure is the sum of the incident wave harmonics transmitted into the structure and reflected at its boundaries because of the acoustic impedance mismatches between the polymer and the surrounding media.

Considering a sinusoidal acoustic wave of amplitude P_0 incoming on the interferometer, characterized by an angular frequency ω and a wave vector k, the pressure inside the structure can be calculated as [4]

$$P = P_0 T \, e^{j\omega t} \left(e^{jkx} \sum_{i=0}^{\infty} (R_1 R_2)^i e^{-jk2L} \right. \\ \left. + R_1 e^{-jkx} \sum_{i=0}^{\infty} (R_1 R_2)^i e^{-jk2L} \right) \tag{3.4}$$

where T and R are respectively the transmission and reflection coefficients at the polymer-water and polymer-silicon oxide interfaces, defined as:

$$R_1 = \frac{Z_0 - Z_1}{Z_0 + Z_1} \qquad R_2 = \frac{Z_2 - Z_1}{Z_1 + Z_2} \qquad T = \frac{2Z_1}{Z_1 + Z_2}$$

By calculating the sum of the geometric series, equation (3.4) is simplified as:

$$P = P_0 T \, e^{j\omega t} \left(e^{jkx} \frac{1}{1 - R_1 R_2 e^{-jk2L}} \right. \\ \left. + R_1 e^{-jkx} \frac{1}{1 - R_1 R_2 e^{-jk2L}} \right) \tag{3.5}$$

$$= P_0 T \, e^{j\omega} \frac{e^{jkx} + R_1 e^{-jkx}}{1 - R_1 R_2 e^{-jk2L}}$$

Now, substituting (3.4) in (3.3), the thickness variation due to the applied pressure can be finally computed as:

$$dl = \frac{P_0 T \, e^{j\omega t}}{E(1 - R_1 R_2 e^{-jk2L})} \int_0^L \left(e^{jkx} + R_1 e^{-jkx} \right) dx \qquad (3.6)$$

The acoustic sensitivity, which represents the absolute value of the optical phase shift per unit acoustic pressure rad/MPa is then expressed, neglecting the acoustic absorption in the polymer (real wave vector), by:

$$S_a = \frac{d\beta}{dP} = \frac{4\pi n |dl|}{\lambda_o P_0} = \frac{4\pi n}{\lambda_o} \frac{\sqrt{2}T}{Ek} \sqrt{\frac{(1 - \cos kL)\left(1 + 2R_1 \cos kL + R_1{}^2\right)}{1 + R_1 R_2 (R_1 R_2 - 2\cos 2kL)}}$$

where λ_o is the optical wavelength of the laser source employed for interrogating the cavity and *n* the refractive index of the sensitive film. By analyzing this equation, it is possible to do some important considerations.

In particular, from the derived expression of the acoustic sensitivity, it is clear that the sensitivity increases with *L*, but vanishes when the acoustic wavelength approaches the polymer thickness, limiting the bandwidth of the interferometer. Therefore, the best thickness depends on the particular application, and the desired trade-off between sensitivity and bandwidth. As a consequence of that, choosing a sensing film characterized not only by low Young's modulus, but also low density (in order to permit high speed of ultrasound waves), is essential in order to maximize the acoustic performances. Moreover, the acoustic sensitivity depends linearly on the refractive index of the polymer and, consequently, a material with high *n* assures a better acoustic sensitivity because of the higher phase shift engendered when the ultrasonic pressure is applied. In addition, it is worth noting that the use of high optical frequencies for interrogating the Fabry-Perot cavity also improves the detection performance. However the use of laser frequencies above the near infrared region can lead to non negligible optical attenuations in the interferometer and consequently decrease the optical sensitivity.

The deformations per unit acoustic pressure ($|dl|/Po$) calculated for two interferometers respectively realized on silicon and dielectric membranes are reported in Fig. 3.3 as a function of the frequency of the acoustic wave.
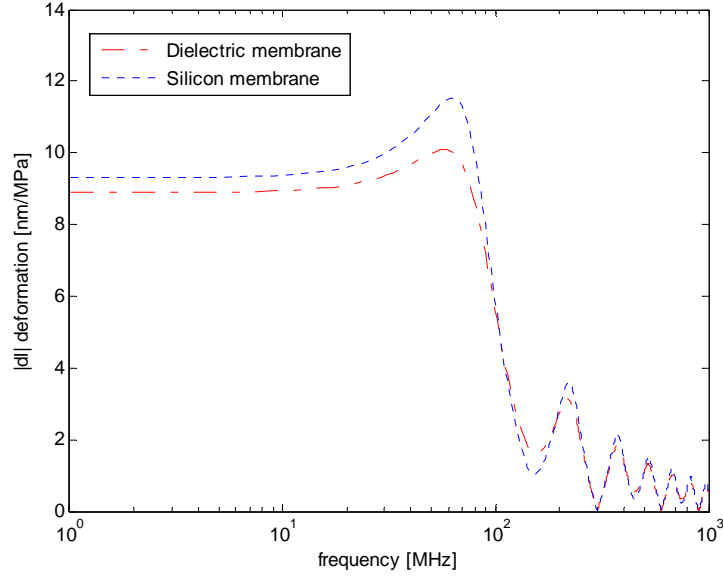
Fig. 3.3. Deformations per unit pressure of 10 μm thick interferometers deposited on dielectric and silicon membranes (10 and 50 nm thick Al layers)

As may be seen from the calculated curves, the two different structures provide similar acoustic performance with an average deformation in the plateau region around 9 nm/MPa for a 10 μm thick polymer. The bandwidth, as may be shown using eq. (3.6), depends on acoustic speed and polymer thickness in the following way:

$$f = \frac{c_a}{L} \tag{3.7}$$

where c_a is the acoustic speed in the material and f is the first frequency for which the right hand side of (3.6) goes to zero, equal to 300 MHz for the considered cases. Therefore, the bandwidth only depends on the geometry and the acoustic properties of the polymer layer and is independent of the characteristics of the supporting structure on which it is realized. This is not true in general for the acoustic sensitivity expressed in eq. (3.2) in which the acoustic impendence difference between the polymer and the substrate is of concern. The parameters used in the simulations, taken from the literature, are tabulated below [6]:

	Acoustic impedance [MRayls]	Young's Modulus [GPa]	Acoustic speed [m/s]
Water	1.5	-	-
SU-8	3.5	2	2886
SiO$_2$	12	-	-

According to the model, the acoustic sensitivity can be increased by using a thicker SU-8 layer in the detector, as shown in Fig. 3.4. As may be observed, the dependence of acoustic sensitivity on polymer thickness is quite linear, leading to considerable improvement of the performance at the expense of some bandwidth reduction.
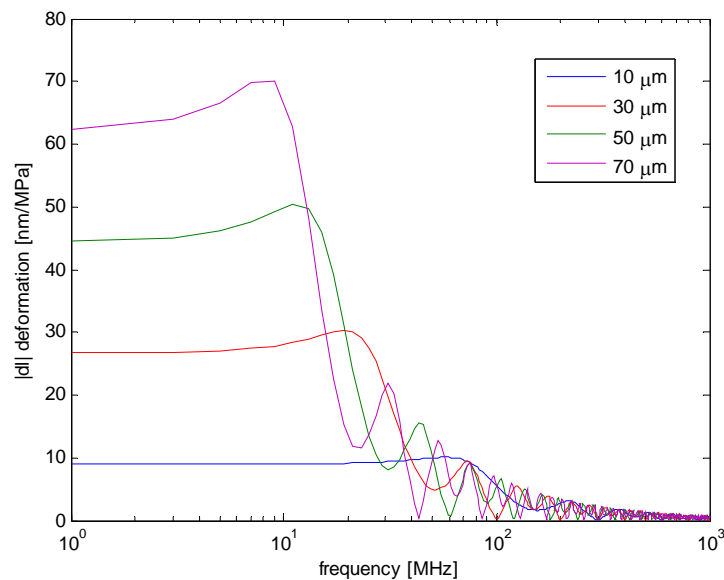
Fig. 3.4. Deformations per pressure unit of several polymer thicknesses (on dielectric membrane, 10 and 50 nm thick Al layers)

3.2.2 Optical Modelling

The optical intensity reflected from a multilayer structure composed by *n* isotropic and homogenous films can be conventionally expressed in matrix notation [7] [8] [9] [10].
Indicating with E_m^+ and E_m^- the electric field amplitudes of waves respectively incident and reflected at the *m*th interface in the multilayer, the relation reported below can be derived by applying the equations of wave propagation:

$$\begin{pmatrix} E_m^+ \\ E_m^- \end{pmatrix} = \underbrace{\frac{1}{t_{m,m+1}} \begin{pmatrix} e^{-j\beta_{m+1}} & r_{m,m+1}e^{j\beta_{m+1}} \\ r_{m,m+1}e^{-j\beta_{m+1}} & e^{j\beta_{m+1}} \end{pmatrix}}_{A_{m,m+1}} \begin{pmatrix} E_{m+1}^+ \\ E_{m+1}^- \end{pmatrix} \tag{3.8}$$

In this way, the electrical fields at the *mth* interface are written as a function of the fields calculated at the successive interface, taking into account the optical phase shift β in the *m*+1 layer and the Fresnel reflection and transmission coefficients *r*, *t*. The phase shift due to the wave propagation within the film can be expressed as:

$$\beta_m = \frac{2\pi}{\lambda} N_m d_m \cos\theta_m$$

where N_m is the complex refraction index of the material, θ_m the propagation angle calculated with respect to the normal direction from the interface and λ the wavelength. For a wave travelling from the *m*th to the (*m*+1)th layer, the Fresnel coefficients $r_{m,m+1}$, $t_{m,m+1}$ for parallel (p) and perpendicular (s) field polarizations are given by:

$$r_{m,m+1}^{\ p} = \frac{N_{m+1} \cos\theta_m - N_m \cos\theta_{m+1}}{N_m \cos\theta_{m+1} + N_{m+1} \cos\theta_m}$$

$$t_{m,m+1}^{\ p} = \frac{2N_m \cos\theta_m}{N_m \cos\theta_{m+1} + N_{m+1} \cos\theta_m}$$

$$r_{m,m+1}^{\ s} = \frac{N_m \cos\theta_m - N_{m+1} \cos\theta_{m+1}}{N_m \cos\theta_m + N_{m+1} \cos\theta_{m+1}}$$

$$t_{m,m+1}^{\ s} = \frac{2N_m \cos\theta_m}{N_m \cos\theta_m + N_{m+1} \cos\theta_{m+1}}$$

By applying eq. (3.8) to every interface, a relation between the electrical fields in the first and last layer of the structure is derived:

$$\begin{pmatrix} E_0^+ \\ E_0^- \end{pmatrix} = \prod_{i=0}^{n} A_{i,i+1} \begin{pmatrix} E_n^+ \\ 0 \end{pmatrix} = \begin{pmatrix} a_{11} & a_{12} \\ a_{21} & a_{22} \end{pmatrix} \begin{pmatrix} E_n^+ \\ 0 \end{pmatrix} \tag{3.9}$$

where the backward wave in the *n*th layer is supposed to have vanishing amplitude.

The reflectance, defined as the fraction of electromagnetic power reflected at the interface calculated with respect to the incoming one, can be then computed for every polarization considering the appropriate Fresnel coefficients:

$$R = \left|\frac{E_0^-}{E_0^+}\right|^2 = \left|\frac{a_{21}}{a_{11}}\right|^2 \tag{3.10}$$

If the light is unpolarized, the reflectance is expressed as the average of the values derived for the parallel and perpendicular polarizations as:

$$R = \frac{R_p + R_s}{2} \tag{3.11}$$

When the electromagnetic wave impinges normally on the structure ($\theta_m = 0$) the Fresnel coefficients are considerably simplified and become independent of polarization:

$$r_{m,m+1} = \frac{N_m - N_{m+1}}{N_m + N_{m+1}} \qquad\qquad t_{m,m+1} = \frac{2N_m}{N_m + N_{m+1}}$$

Coming back to the interferometer in Fig. 3.2, as discussed before the acoustic pressure *P* applied to the structure modulates the polymer thickness (indicated below by the variation *dl*) and leads to a modulation of the phase shift that, neglecting strain induced variations in the refractive index, can be expressed by:

$$\beta = \frac{2\pi}{\lambda} N(d + dl) = \beta_{DC} + d\beta(P)$$

As a consequence of that, the optical intensity reflected by the interferometer, namely the reflectance of the multilayer structure multiplied by the incident intensity, is given by the sum of a continuous part (independent of the applied pressure) and another variable that can be exploited to measure the acoustic wave hitting the Fabry-Perot, according to the following formula:

$$I_R = I_{DC} + dI(P) \tag{3.12}$$

in which I_{DC} is an undesired contribution that can interfere with the detection of the transient intensity $dI(P)$. In fact, a too large value of the intensity may saturate the photodiode and increase the shot noise current. The structure of the interferometer is thus designed in a convenient way for maximizing the variable part with respect to the DC level in

order to reach the best performance. Furthermore, resolution and phase sensitivity can be increased by interrogating the cavity with an optical intensity level chosen to be as close as possible to the detector saturation threshold (this can be done in practice by tuning the laser power), even if this leads to some limitations in the maximum detectable pressure level.

3.3 Optical Characterization

3.3.1 Preliminary Tests

Four prototypes of planar Fabry-Perot interferometers, with different thicknesses of the spacer and of the bottom metal film were realized on fused silica substrates (pure SiO_2), using negative SU-8 10 resist to fabricate the polymer spacer according to the process flow of Fig. 3.5. Fused silica was chosen to mimic the optical properties of the SiO_2/Si_3N_4 membrane that was adopted in the final detectors. Aluminum was deposited by evaporation to realize both the thin and thick metal layers of the interferometers. The second metallization was 50 nm thick, while two thicknesses were tested for the thinner one placed under the SU-8 layer (namely 5 and 10 nm).

1. Bulk fused silica

2. Thin Al evaporation (5, 10 nm)

3. SU-8 spinning, exposure and bake

4. Thick Al deposition (50 nm)
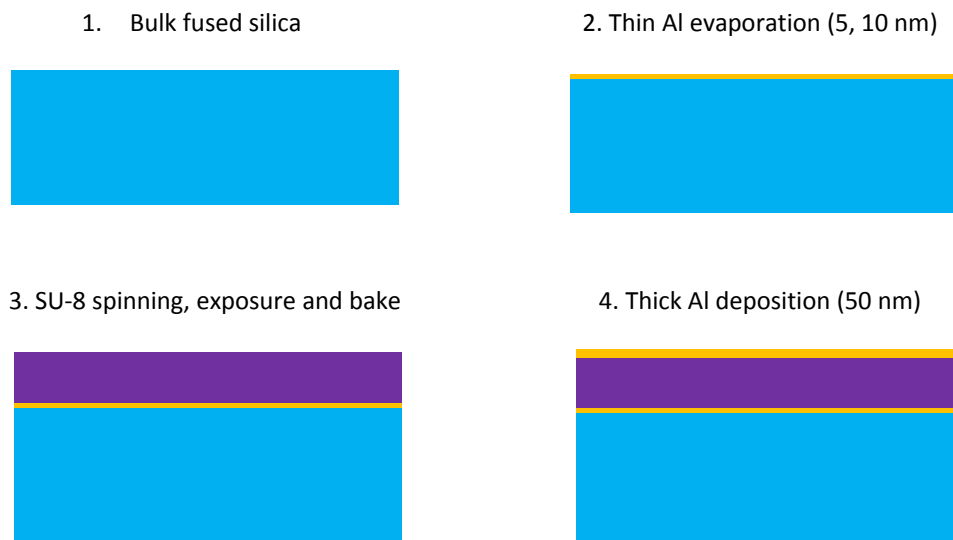
Fig. 3. 5. Process flow for the fabrication of 4 receivers prototypes

SU-8 was deposited by spinning, in roughly 5 and 10 μm thick layers, obtained by varying the spinning speed (4400 and 3000 RPM respectively). The resist was then exposed to UV light and hard baked at 200°C for 1 min on a hotplate before depositing the last Al layer.

Fig. 3.6. Avantes (left) and FTIR (right) spectrometers

As can be seen from eq. (3.8), the reflectance dependence on wavelength is connected to the phase shift. The modulation depth and optical sensitivity can be then derived by optical reflectance measurements. In Fig. 3.7 the reflectance spectra measured in the near infrared range by means of the Avantes Spectrophotometer (Fig. 3.6 left), are reported for the different structures. As may be observed for the reflectance measurements, the use of a 10 nm thick aluminium layer assures an intensity modulation depth of about 80% and a maximum slope in the reflectance-wavelength plot of 37 μm^{-1}. As a whole, the thickest metallization leads to a remarkable improvement of performance, while the use of thicker polymer layers results in fringe shrinkage and thus in an increment of sensitivity.

On the same samples, reflectance has also been measured in the near-infrared range above 1 μm (Fig. 3.8). The measurements were realized though a Fourier Transform Infrared Spectrometer (FTIR, Fig. 3.6 right). In this case, the measurement results show that the fringe amplitude decreases with increasing polymer thicknesses revealing a partial coherence loss of light during its propagation within the interferometer.
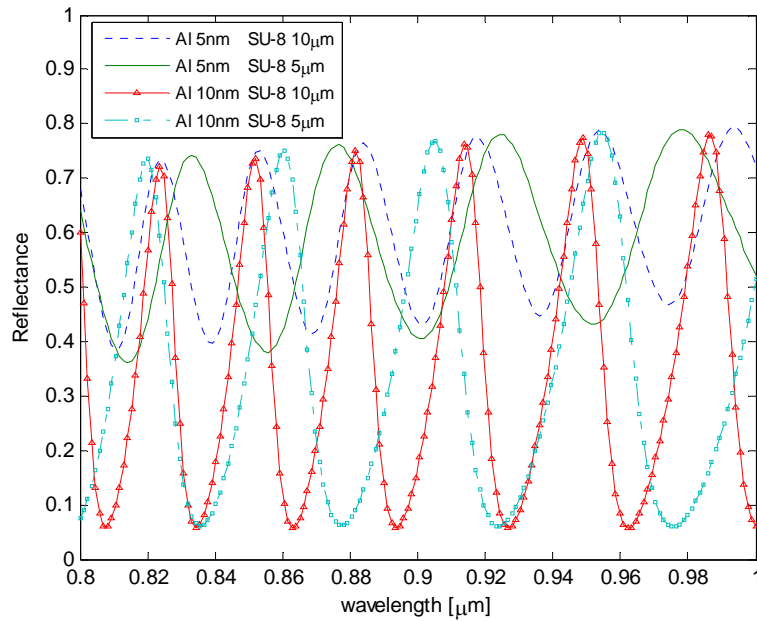
Fig. 3.7 Reflectance measures of receivers prototypes on fused silica, acquired by Avantes Spectrophotometer
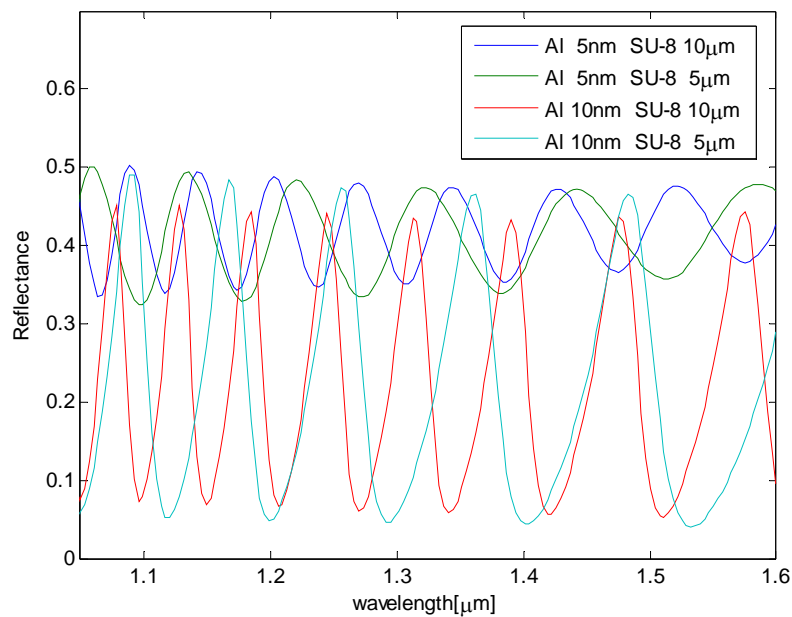
Fig. 3.8. Reflectance measures of receivers prototypes acquired by FTIR Spectrometer

When a film behaves incoherently, the electromagnetic waves combine in a manner that is insensitive to phase differences resulting in disappearance of interference fringes. If the film thickness is not large enough to show a completely incoherent behavior, a partial coherence arises making the optical simulation of the structure difficult. The coherence length, which is

an estimation of the maximum thickness for which the film shows a coherent behavior, can be expressed as $L = \lambda^2/(n\Delta\lambda)$, where λ and $\Delta\lambda$ are respectively the central wavelength and spectral width of the light source, and n is the refractive index of the propagation medium. Fortunately, the use of a monochromatic source like a solid-state laser assures a coherent behavior and, consequently, the actual modulation depths obtained on the interferometers during their operation will be much larger than those observed in Fig.3.8.

Besides the planar interferometers described above, some additional test structures were also realized in order to determine the complex refractive indexes of the thin layers used in the interferometer, whose values have been used in optical simulations performed to predict the optomechanical behaviour of the Fabry-Perot detectors. Such model can be used to determine the best geometry that can be adopted for the interferometer for maximizing sensitivity and modulation depth and, consequently, effectively to assist the design of the detectors. Thanks to the software application realized in this thesis, and briefly described in chapter 2, a rather quick and easy optical characterization of the thin layers by photometric and infrared measurements was possible.

3.3.2 Refractive Index of Aluminum Thin Layers

The problem of aluminum optical characterization has been investigated for many years. In 1963, Ehrenreich [11] demonstrated the existence of an absorption band at 1.6 eV in the thin film material. Successively, a complete calculation of refractive index was realized by Mathewson and Myers [12], showing the presence of another strong absorption peak in the interband region at 0.5 eV. Nevertheless, the optical constants reported in the literature for Al films are not suitable for simulating the optical behavior of multilayer structures where very thin Al films are used, like the interferometers investigated here. In fact, such optical constants are appropriate only for Al thicknesses greater than roughly 30 nm, since the optical constants of very thin films are strongly dependent on the process used for the deposition and, when only few nanometers are deposited, may depend on the deposition substrate, as well. Therefore, the optical constants for the thin films used in the detectors have been extracted experimentally on test samples, according to the procedure reported in the following, and used in the predictive model of the Fabry-Perot cavity.

The optical characterization of thin Al was realized by evaporating 10 nm thick layers on double polished silicon wafers and acquiring several experimental data in the visible and

infrared spectra on these samples. Starting from the reflectance and transmittance measurements, the complex refractive index was derived through a fitting procedure employing the Drude-Lorentz model. In Fig. 3.9 the simulations are compared with the experimental data, yielding a very good match.
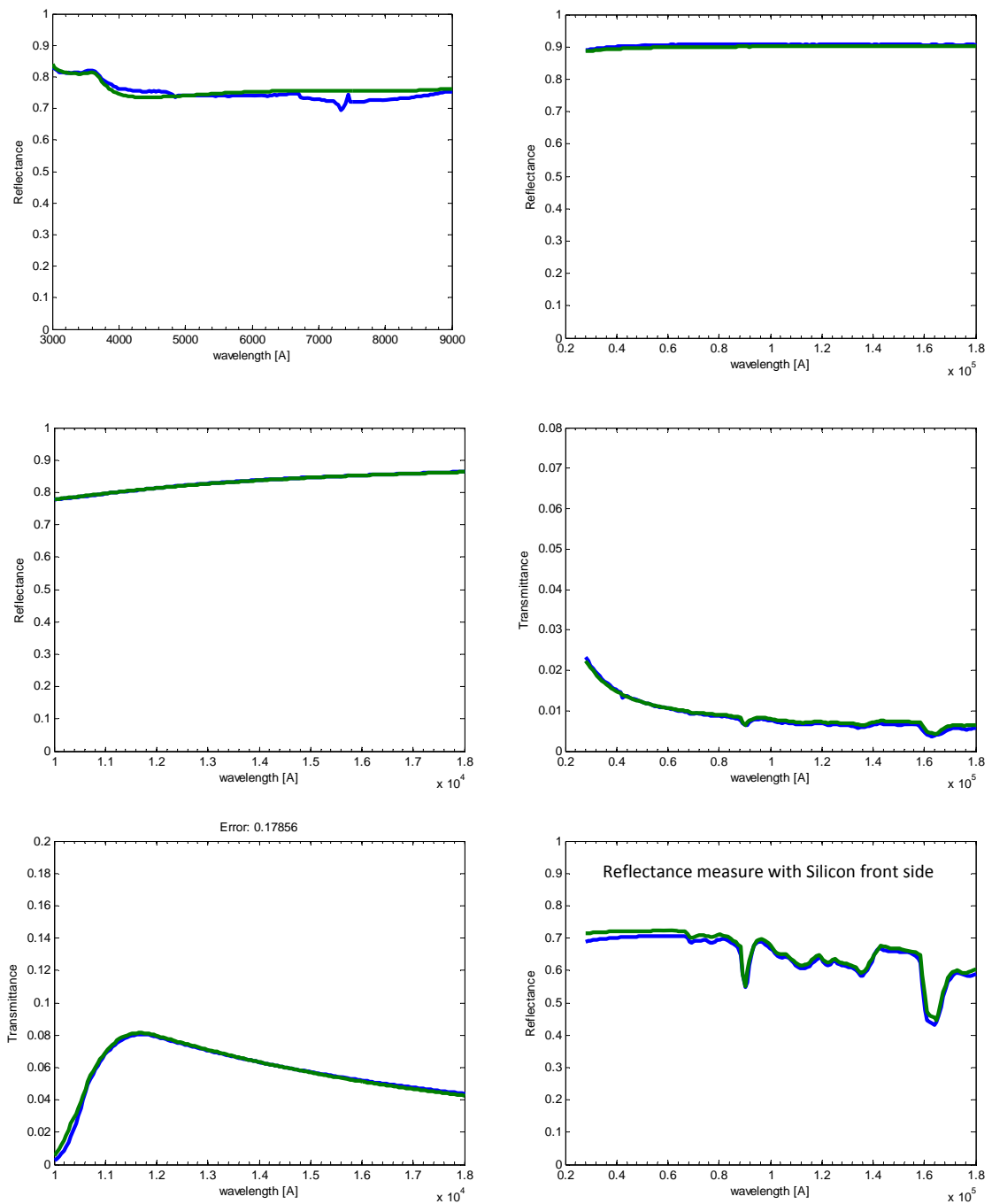
Fig. 3.9 Reflectance and Transmittance measures on 10 nm thick Al evaporated on double polished silicon substrate

In the extraction, the Drude and Lorentz variables were simultaneously modified in order to minimize the error function calculated using six optical measures. In particular, the FTIR acquisitions were of primary importance to determine accurately the Drude term and did not lead to a wrong estimation of interband contributions (modeled by damped Lorentz oscillators). The complex refractive index obtained for thin Al is shown below in the frequency range of interest, compared with the same parameter measured on a 50 nm thick, optically bulk sample.
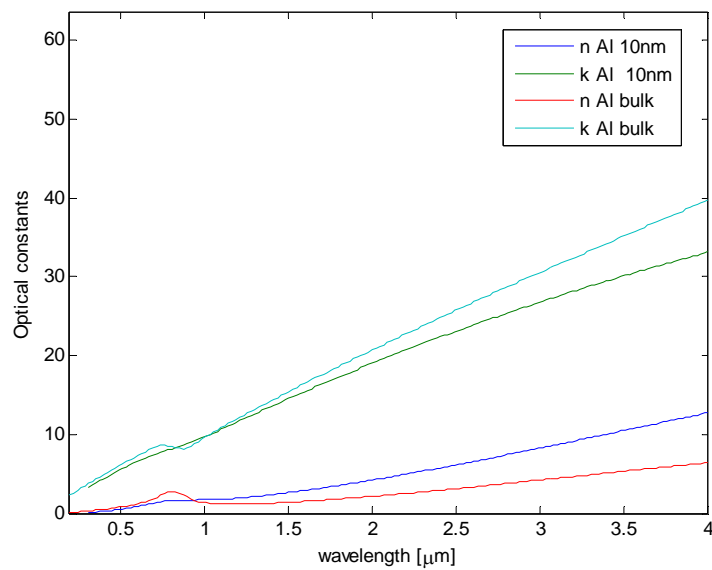
Fig. 3.10. Optical constants of thin and bulk aluminum films

As can be observed by comparing the determined optical constants with those commonly obtained on thick aluminum [13], the interband peaks, due to the presence parallel bands, are less strong in the thin films. Consistently with theoretical expectations, a small variation of the measured optical coefficients was noticed between layers deposited with slightly different thicknesses. Anyway, the refractive index determined for the 10 nm thick Al layers could be employed to model the interferometer with good match with experimental data, as will be shown in the following. Some measurements on Al films deposited on bulk silicon oxide wafers (fused silica) were realized as well. However, in this case the optical characterization was less easy because it required a previous calculation of silicon oxide refractive index, whose vibrational modes in the infrared region are modeled using a quite high number of classical oscillators that make the extraction procedure quite difficult.

3.3.3 Refractive Index of SU-8 Photoresist

SU-8 is an epoxy based photoresist that is widely used in Micro Electro Mechanical System (MEMS) technology. Developed by IBM [14], it was initially applied as a standard photoresist for high resolution lithography. Differently than many other resists, SU-8 presents very good mechanical properties and consequently can be suitable as a structural material. Thanks to its thermal and chemically stability, it is often employed for the fabrication of MEMS devices, especially in microfluidic applications where water insolubility is required. Moreover, it is biocompatible [15] and suitable for fabricating very high aspect ratio structures. Thanks to its relatively low Young's modulus ($\cong$2GPa), this resist is a good candidate as a sensitive film in the Fabry-Perot cavity, and has already been used for this purpose [16]. Moreover, its acoustic impedance of about 3.5 MRayls assures a good acoustic match with water (1.5 MRayls), eliminating the need to use coupling layers to improve the detector performances. However, it has to be observed that an acoustic wave travelling into the SU-8 photoresist is slightly attenuated (a 0.33 db/μm attenuation has been experimentally derived at 1 GHz [17]).

The optical properties of SU-8 10 were determined by spinning the resist on fused silica substrates and measuring its reflectance and transmittance in the visible and near infrared ranges. The photoresist was spun on two wafers at 3000 RPM and 4400 RPM to investigate the effect of the spinning speed, and of the different thickness consequently obtained, on the optical properties. During the processing, the SU-8 layers were baked for 2 minutes at 65°C and subsequently brought to 95°C using a roughly 2 min temperature ramp and left at the final temperature for 5 min before exposure (performed with an exposition time of 15 sec). Afterwards, the resist was baked again (1 min at 65°C, 2 min at 95° C) in order to complete the cross link reaction initiated by exposure. Finally, after the development, the resist was hard baked for 1 min at 200°C to further cross-link the patterned SU-8 structures and consequently stabilize their mechanical properties. This last operation is strongly recommended when the photoresist is used as a structural material and therefore left as a part of final device.

The reflectance and transmittance measurements realized on the thickest SU-8 layer are reported in Fig 3.11.
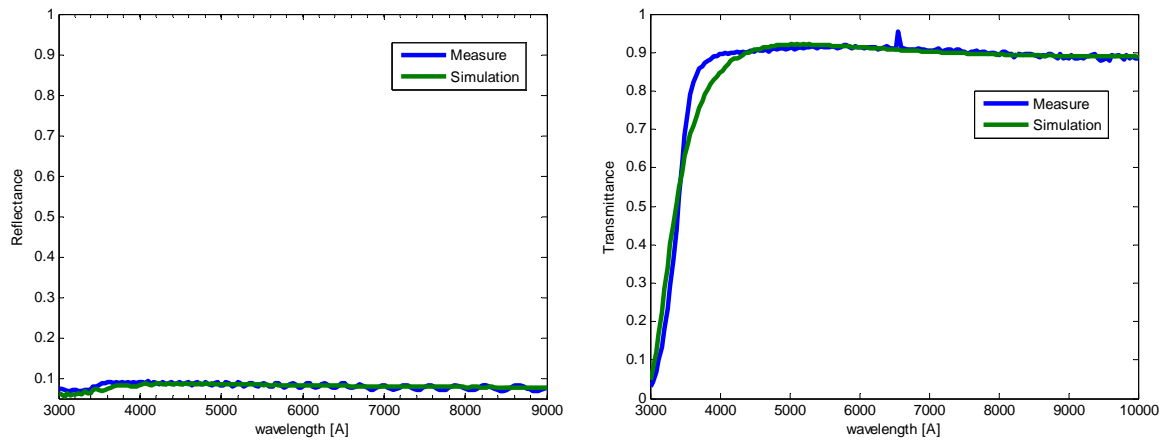
Fig. 3.11. Reflectance (left) and transmittance measures realized on 10 µm thick SU-8 (3000 RPM)

The optical behavior was well simulated by using a Cauchy dispersion relation. The refractive index and the extinction coefficient, derived by the fit procedure introduced previously, are shown in Figs. 3.12 and 3.13 respectively.
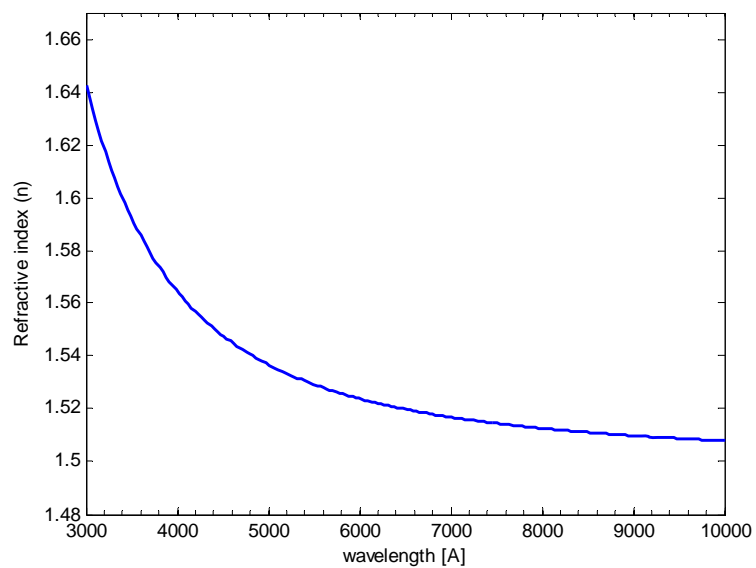
Fig. 3.12. Refractive index of SU-8 photoresist
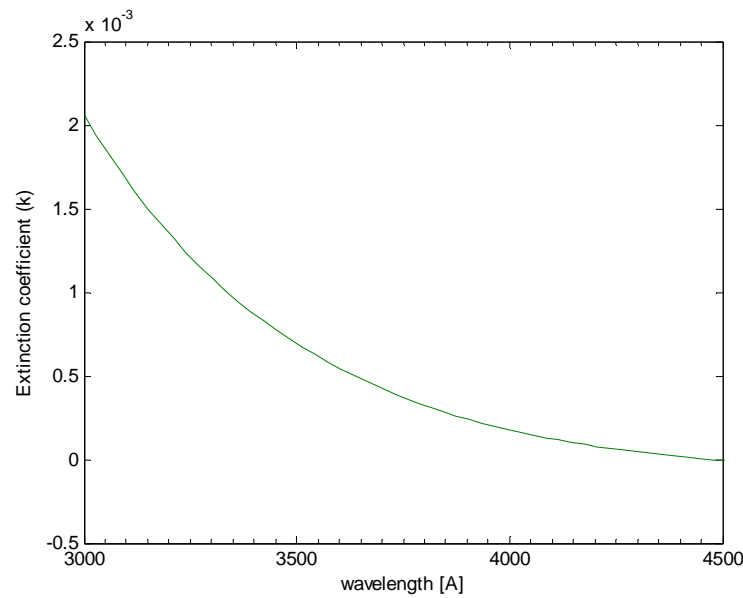
Fig.3.13. Extinction coefficient of SU-8 photoresist

The same values of the extracted optical constants allowed for simulating satisfactorily the reflectance and transmittance of the photoresist layers of both thicknesses, evidencing the fact that the optical properties have no remarkable dependence on the resist thickness. On the contrary, slight variations of the optical constants were observed depending on the bake type performed, resulting in a reduction of refractive index after the hard bake procedure [17]. Moreover, as can be observed in Fig. 3.13, the optical absorption becomes negligible for wavelength values larger than 400 nm, confirming the suitability of this material for the fabrication Fabry-Perot devices used with infrared lasers. In fact, a low attenuation of the electromagnetic radiation, interrogating the Fabry–Perot cavity, is quite important to increase the modulation depth of the interferometer.

3.3.4 MOMS-Based Interferometer

Once completed the optical characterization of the thin layers constituting the detector, the reflectance measurements performed on the interferometer prototypes realized on fused silica were compared with the simulated data as shown in Fig. 3.14. This measurement, realized on the interferometer constituted by 10 nm thick Al and 10 μm thick SU-8 layers, does not show a perfect match with the simulation in the whole measurement range. This can be attributed to a partially incoherent optical behavior of thick SU-8 at shorter

wavelengths. However the match with experimental data is very good in the visible and near infrared range, where the measure was acquired by the Avantes spectrophotometer.
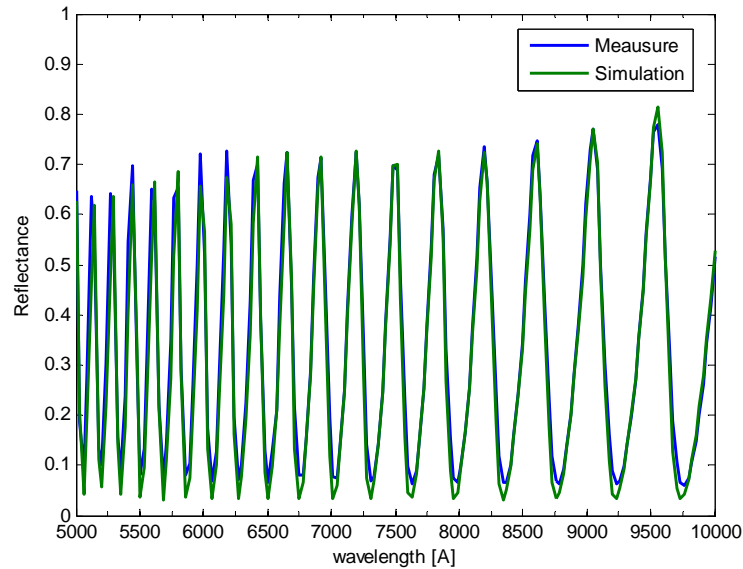
Fig. 3.14. Reflectance measure and simulation of a detector prototype

Thanks to simulation procedure, the reflectance could be calculated as a function of the SU-8 photoresist thickness for the fabricated detectors, as shown in Fig. 3.15 in which the structure that assures the best sensitivity performance at 1550 nm wavelength was considered.
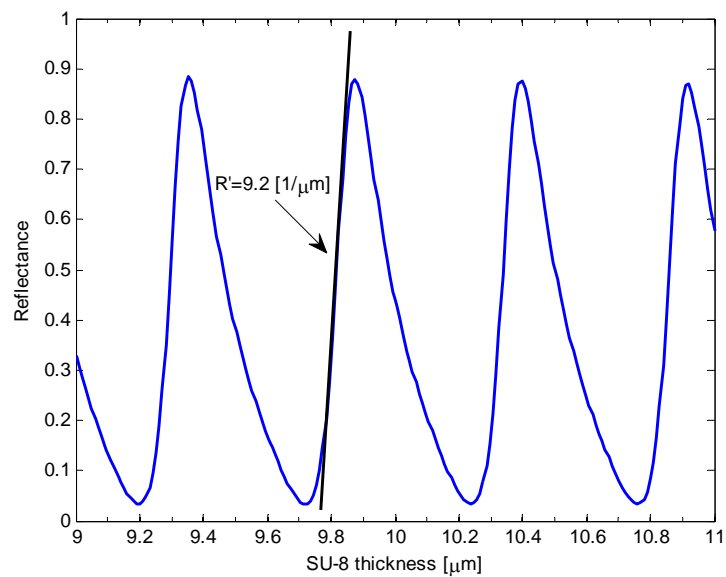
Fig. 3.15 Reflectance simulated against polymer thickness (10 nm thin Al, 1550 nm wavelength)

As may be observed, the optical behavior is very promising because it assures a remarkable variation of the optical intensity even for very small thickness changes. In the region of maximum slope, in particular, a sensitivity of roughly 9.2 μm^{-1} can be derived from the simulation. In order to have high opto-mechanical sensitivity in ultrasound detection, an operating point corresponding to a high slope of the reflectance/thickness plot reported in Fig. 3.15 should be chosen, theoretically. Anyway, despite the good thickness uniformity achieved with the fabrication process, such operating point cannot be determined with sufficient precision by controlling the thickness of the SU-8 layer. In order to overcome this problem, a tunable laser source can be used for interrogating the interferometer, in which the wavelength can be adapted up to reaching the maximum optical sensitivity. As it clearly appears in the simulation, a narrow tuning range (about 30 nm) is expected to be sufficient to guarantee the best detection performance.

In order to investigate in deeper detail the relation between laser wavelength and polymer thickness, the reflectance has been reported in Fig. 3.16 on a 3-D plot as a function of wavelength and SU-8 thickness.
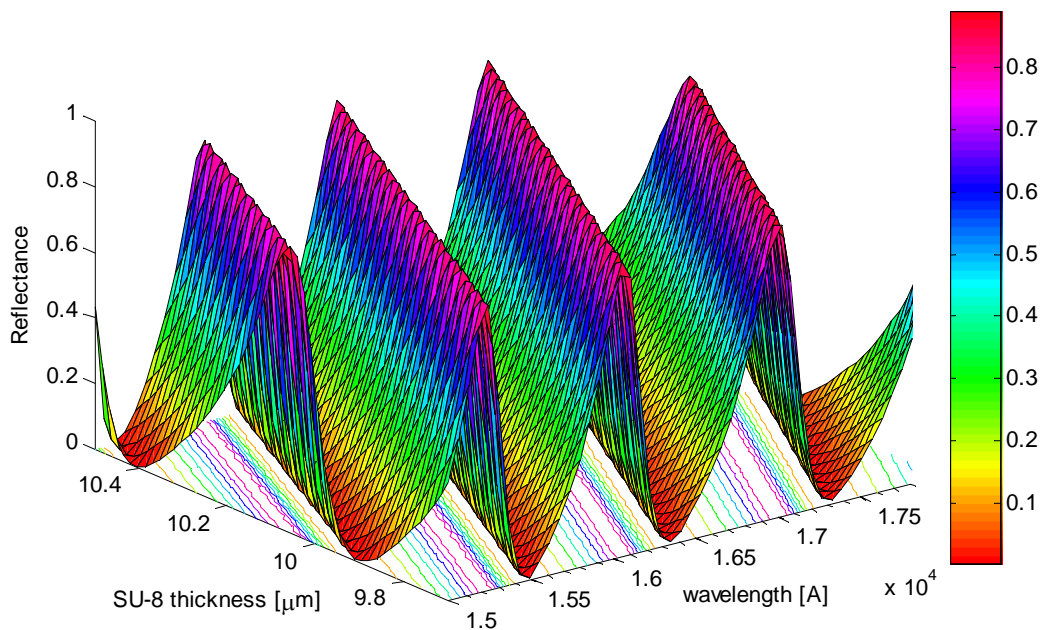
Fig. 3.16. Reflectance of the Fabry-Perot deposited on Fused-Silica (10 and 50 nm thick Al metallizations)

The interference fringes are clearly visible in both the x and y direction in the plot, corresponding to the two physical parameters considered. From the 3-D plot it is clear that a

working point showing a high reflectance derivative with respect to wavelength assures at the same time high sensitivity against the Fabry-Perot cavity length, giving the possibility to determine the optimal operation wavelength with concern to opto-mechanical sensitivity, through a quite straightforward reflectance measurement on the Fabry-Perot.

In order to determine the effect of the thickness of the thinner Al metallization on the detection performances, the modulation depth of the reflectance was calculated as a function of the mentioned parameter by optical simulations (Fig. 3.17). From the results, it was derived that evaporating Al films with thickness higher than 10 nm causes a degrade of the opto-mechanical transfer function, because of the sensible reduction of the laser beam intensity transmitted into the Fabry-Perot cavity. On the other hand, excessively thin layers do not provide sufficient reflection at the internal face of the Fabry-Perot and consequently most of the back reflected light crosses the film, and do not contribute to interference within the cavity.
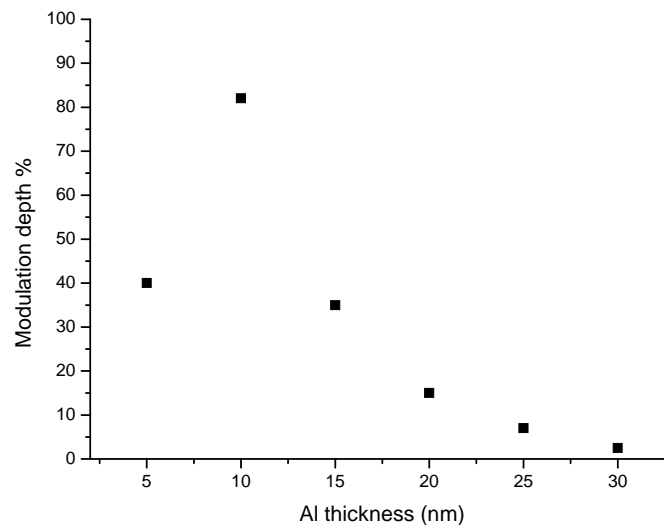
Fig. 3.17. Modulation depth as a function of thickness of first Al metallization, derived by optical simulations

In this respect, it must be considered that the calculated modulation depths may suffer from some imprecision in the values of the optical constants assumed for thin Al. This is due to the fact that, as explained before, the optical constants of a very thin layer are dependent on process variables such as the deposited thickness. Then, the fringe shape, determined by

considering the optical constant of the 10 nm thick Al also for thicker or thinner films, could contain some estimation error. The modulation depths of interferometers with thickness of the first metallization above 20 nm were, instead, calculated by using the well-known refractive index of optically bulk aluminum, reasonably assuming an optical behavior similar to the bulk material for such layers.

Differently from the prototypes fabricated on fused silica, the final interferometers were realized on a dielectric multistack. Therefore, the refractive index differences between silicon oxide and nitride must also be considered for an accurate modeling of the detector in this case.
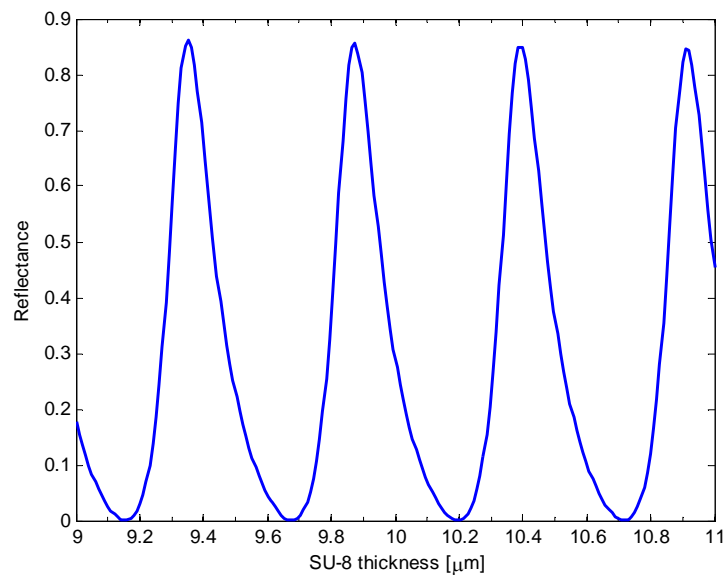
Fig 3.18. Reflectance of a interferometer carried out on dielectric membrane (λ=1550 nm)

In Fig.3.18, the reflectance calculated for the backside of the dielectric membrane assumed in contact with a silica fiber and with the optimized interferometer of Fig. 3.15 on top of it is plotted against the SU-8 thickness. As may be observed, the optical response has a similar behavior compared to the interferometer on fused silica of Fig. 3.15 (which was however simulated without the presence of the fiber), with an even higher modulation depth. This effect depends on the fact that thermal oxide, which is the first layer of the membrane, has a refractive index value very close to the one of the optical fiber, usually made of silica glass, minimizing the energy reflected at the core-detector interface, which actually is almost zero around the points of minimum reflectance in the plot. Furthermore, the additional films (silicon nitride and LTO) needed to fabricate the stress-compensated membrane present low

refractive indexes and very low absorption, and consequently have an almost negligible effect on the optical function transfer of the detector.

As discussed for the emitter, the developed technology allows the simultaneous fabrication of ultrasonic detectors on dielectric and silicon membranes. However, when the Fabry-Perot devices are realized on silicon, the reflectance is significantly distorted because of the overlap of silicon and polymer interference fringes. As can be seen in Fig. 3.19, actually, the fringes due to the SU-8 interferometer are less dense than those owing to the silicon membrane because of its lower thickness, as can be clearly seen by performing a simulation in which silicon is modeled as an optically incoherent medium (also shown in the figure).
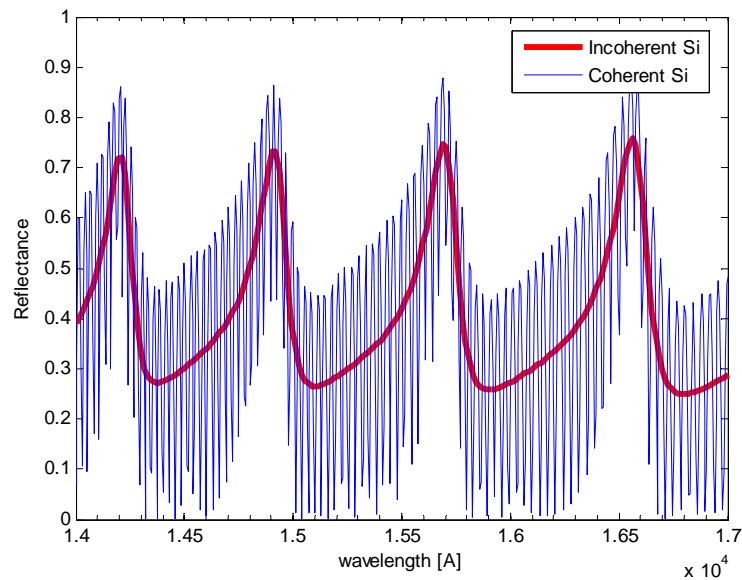
Fig.3.19. Reflectance calculated for a Fabry-Perot deposited on 100 μm thick Si membrane

Differently from the case of the prototype realized on the dielectric membrane, in which the interference fringes due to the refractive index variation between the fiber and the membrane is almost negligible, the presence of silicon strongly affects the optical behavior, complicating the calculation of the best operation wavelength for the device. Since the tunable laser sources usually present a linewidth of few MHz, they typically have a coherence length in the order of meters. In order to dump undesired interference effects like those related to the presence of the silicon membrane in the interferometers, it is possible to introduce noise in the laser line, broadening its bandwidth and, consequently decreasing its coherence length to few millimeters. This method, although appropriate to cancel the

possible energy losses due to the optical interference taking place within the fiber, it is not useful for layers thinner than 1 mm, like the silicon membrane considered. As may be seen in Fig. 3.20, in which the reflectance of the interferometer is plotted as a function of wavelength and SU-8 thickness, the effect of silicon interference fringes makes the theoretical dependence of the optical transfer function on the design parameters rather difficult to read.

However, it must be said, that, as discussed in chapter 2 for the emitters, the small unavoidable variations of the silicon membrane thickness due to the DRIE etching profile might partly smooth out the undesired interference pattern, introducing some spatial averaging effect on the reflected light. Such effect, anyway, is expected to be lower than the case on the emitters because of the smaller core of the single mode fibers commonly used in interferometric applications at these wavelengths (usually around 10 μm in diameter).
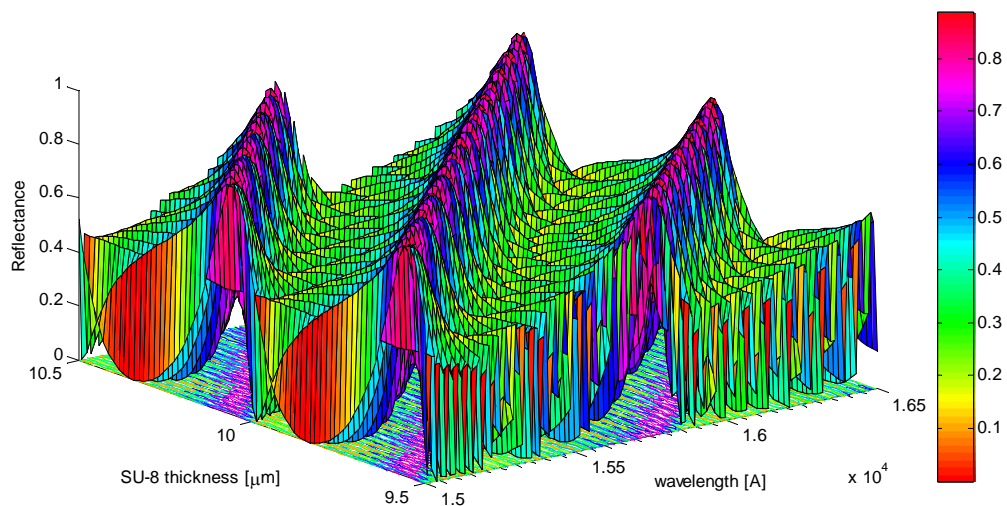
Fig. 3.20 Calculated reflectance of a Fabry-Perot interferometer fabricated on silicon membrane

Moreover, it is worth noting that, even in the presence of the described distortion of the optical transfer function due to the presence of the thick silicon membrane, the functionality of the MOMS detector should be maintained because the modulation of the optical intensity reflected from the Fabry-Perot cavity only depends on changes in the thickness of the SU-8 layer, since silicon is too stiff to take part in the acoustical-optical conversion process. Anyway, besides introducing the problem of additional interference fringes, the presence of the silicon membrane reduces the modulation depth compared to the case of the dielectric

membrane because of its optical absorption in the near infrared region and its higher refraction index difference with respect to the silica fiber.

By analyzing the results of acoustic and optical simulations, it is possible to conclude that, differently than the case of the MOMS emitter where the presence of the silicon membrane provided some benefits in term of faster cooling (even if balanced by a lower peak temperature), the fabrication of ultrasonic detectors on dielectric membrane represents the best solution to assure high sensitivity and easy calibration of the operation wavelength.

3.4   Process Flow

The process flow designed for the fabrication of the ultrasound detectors is shown in Fig. 3.21. The first steps, which allow the fabrication of the dielectric membrane and the backside silicon oxide mask, are completely analogous to those analyzed for the ultrasonic sources and will not be described here. Quite obviously, these similar process flows have been conceived to permit, in principle, the simultaneous fabrication of emitters and receivers on the same substrate, even if the full compatibility of the two processes is not trivial, as will be discussed in the following chapter.

After steps 1-9, identical to the case of the emitters' fabrication flow described in Chapter 2, the first partially reflective mirror of the Fabry-Perot cavity (10 nm thick Al) is deposited by electro-gun evaporation (step 10) and, afterwards, the SU-8 resist is spun at 3500 RPM and thermally treated as explained in section 3.3 (step 11). The top 60 nm thick, totally reflective aluminium mirror is then deposited by evaporation as well (step 12), masked with positive photoresist and patterned by wet etching (step 13). In this step, the use of a stripping solution (Posistrip ARCH Chemicals) with ultrasonic agitation was tested, for removing the resist mask, but the attempt was unsuccessful because wet stripping led to the detachment of Al from SU-8. In order to overcome the problem, the photoresist stripping was then realized using its development solution after a new exposure or, alternatively, by oxygen RIE etching.

After completion of the Fabry-Perot structures on the front side, the final back side Deep Reactive Ion Etching (DRIE) step is executed to define the MOMS (step 14) and allow the fiber insertion (step 15).

1. Silicon Bulk (500 µm)

2. Thermal Oxide (700 nm)

3. Nitride (300 nm)

4. Low Temperature oxide (LTO,1µm)

5. Back LTO deposition (2 µm)

6. SiO$_2$/Si$_3$N$_4$ patterning

7. Back photoresist mask

8. Deep reactive ion etching (100 µm) and resist stripping

9. Dielectric membrane patterning

10. Al Evaporation (10 nm)

11. SU-8 resist (8 µm)

12. Al Evaporation (60 nm)

13. Wet Al etching (50 nm)

14. Silicon DRIE (400 µm)

15. Fiber insertion

Fig.3.21. Process flow for the fabrication of opto-acoustic ultrasonic detectors

3.5   Fabrication Process

As mentioned before, the detectors' fabrication process is in many aspects similar to the one describer earlier in this thesis for the MOMS-based ultrasonic emitters. An analogous solution for micromachining in the two cases was chosen not only for the similarities of the two types of MOMS, but also because the final purpose of the research carried out with this thesis is, in fact, the development of a technology that permits the full integration of ultrasounds generators and detectors on the same MOMS. This choice also helped speed up the development of the fabrication technology for the detectors, by fully exploiting the experience accumulated in the experimental tests carried out earlier for the emitters. As a consequence of that, the micromachining of the MOMS detectors was quite smooth in the experiments, yielding good results like the one shown in Fig. 3.22, in which the back side view of a MOMS containing a circular array of detectors realized both on dielectric and silicon membranes is shown, after the first DRIE step (step 8 in the process flow).
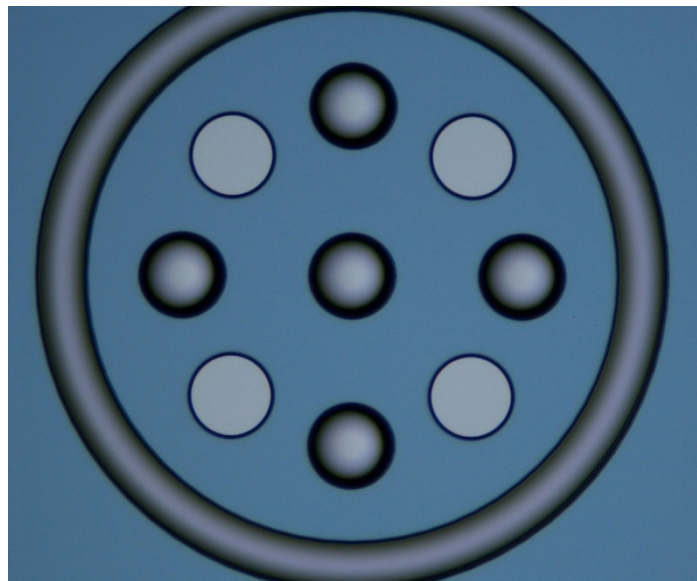
Fig. 3.22. Optical image of back side after first silicon etching

The etched structures were subjected to a 15 min DRIE process, leading to an etching depth of roughly 95 μm (in the structures with diameter of approximately 250 μm), while the other four visible geometries were covered by OiR photoresist (step 7) during the etching step, enabling the double depth silicon etching.

After this first backside DRIE etching, the microfabrication continued on the wafer front with the RIE patterning of the 2 μm thick dielectric membrane that was removed in regions targeted to the fabrication of Fabry-Perot on silicon, in order to avoid the additional optical attenuation that would take place if the dielectric stack was left under the interferometer on the silicon membrane. After the front side patterning of the dielectric stack, the 10 nm thick aluminum layer constituting the first partial reflecting mirror of interferometer was then deposited by evaporation, and the SU-8 spun and baked following the previously described procedure. In these tests, the exposure time was increased up to 18 sec, against the 15 sec normally employed to assure a good match between photolithographic mask and patterned resist, in order to correctly pattern the resist despite the 2 μm high steps existing on the front side of the wafer after the dielectric stack patterning.

With the baking process described, the SU-8 showed a very good adhesion on aluminum, as could be verified by performing scratch tests on the wafer front with scotch brite (M3 Glass 270 syrom), in which no detachment of SU-8 or Al from the substrate was observed. A SEM image of the front side of a processed sample after the completion of the Fabry-Perot structures is shown in Fig. 3.23.
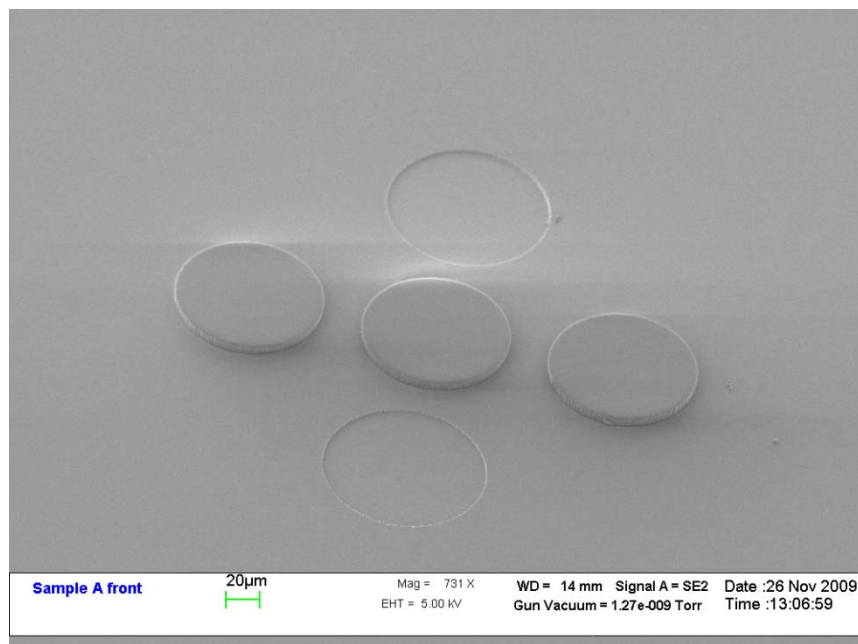
Fig.3.23. Front side view of an array of three detectors

Three 8 μm thick interferometers are visible together with two circular etched areas on the dielectric membrane, designed for the fabrication of carbon emitters on silicon membrane,

according to the integrated process whose development will be described in the following chapter.

A particular of the dielectric multistack observed in cross-section is reported Fig. 3.24, in which the three layers constituting the membrane (thermal SiO_2, Si_3N_4 and LTO) are clearly visible for their different contrast at SEM. As may be observed, the measured thickness of the nitride layer is approximately 270 nm, very close to the value chosen in process design (300 nm) to effectively balance the compressive stress of the silicon oxide layers.
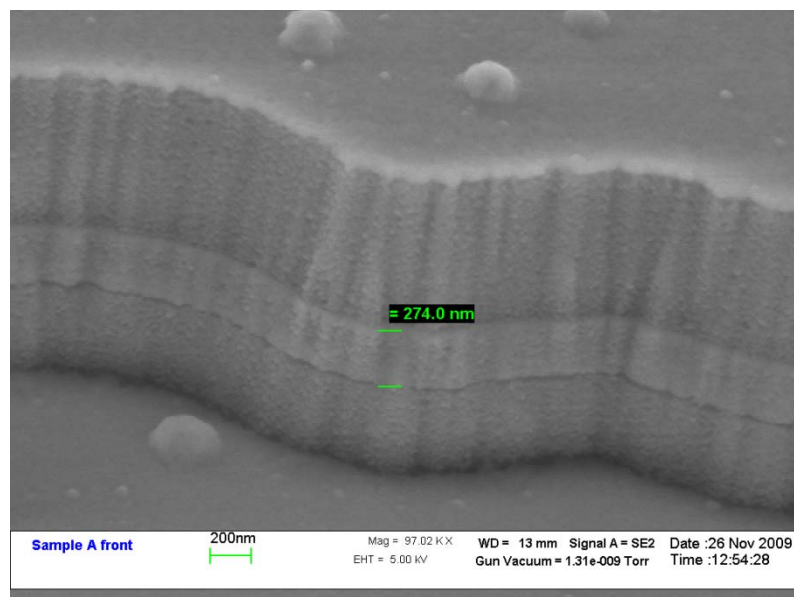
Fig. 3.24. SEM image of the dielectric membrane

Once completed the fabrication of the Fabry-Perot interferometers with the final 60 nm thick Al evaporation, the critical aspects related to the patterning of the second Al layer mentioned before were investigated. In the first tests, the wet etching of aluminum by means of the classical procedure consisting in lithography, wet etching and wet stripping proved to be impossible. In fact, despite the 200°C hard bake, the integrity of SU-8/Al interfaces was degraded during the removal of the positive resist mask. In particular, the thick upper aluminum layer detached from the underlying polymer at the very beginning of the stripping process and, while the stripping proceeded, the SU-8 layer was also removed from the substrate. This effect was observed even without utilizing ultrasonic agitation during stripping. In order to overcome this problem, two different techniques were investigated.

The first one took advantage of the use of positive tone photoresist as a mask for the patterning of the Fabry-Perot upper metallization. Since, actually, a positive resist becomes soluble in its development solution after being exposed to ultraviolet light, the mask layer could be removed, once completed the Al etching, by further exposure and development of the positive resist. This operation did not affect the SU-8 because it was already completely crosslinked by its own development process and by the hardbake procedure formerly performed. In this way, Al etching on top of the interferometers was possible, as shown in Fig. 3.25.
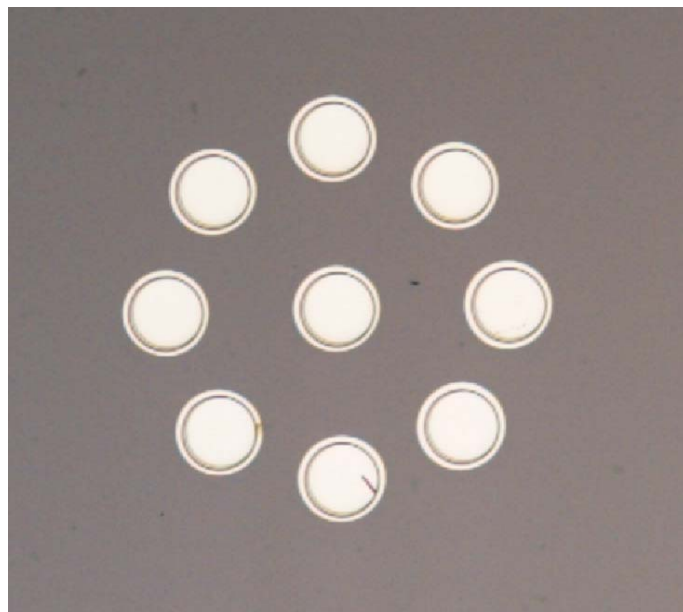
Fig. 3.25. **Al wet etching by positive resist masking**

In the described procedure, the exposure times (18 and 7.9 sec respectively for SU-8 and OiR resists), were accurately chosen in order to achieve a complete coverage of the Fabry-Perot during the wet aluminum etching. The OiR positive resist has, in fact, a nominal thickness of 4 μm and is not completely suited to provide good step coverage on patterned structures as thick as the interferometers (that present roughly 8 μm high steps). Furthermore, as will be cleared later on, the Al/SU-8 interface is slightly damaged even using the removal technique based on positive resist development after wet etching. The shorter exposure time, therefore, is particularly important because it allows for covering the sidewalls of the interferometers more effectively, maintaining the borders of the Fabry-Perot structures

covered by the positive resist for a longer time during the resist removal process. This was confirmed by the fact that the interferometers appeared undamaged after the first development of the OiR resist used in its patterning before Al etching, most likely because the SU-8 was completely covered by the positive resist for almost the whole development process, in this case.

By utilizing a photoresist development time of 50 sec, a satisfactory removal of the positive photoresist after Al etching was achieved. In Fig. 3.26, the undesired deterioration of the Al/SU-8 interface is reported by way of example, related to a fabrication test in which the development was prolonged by 40 sec beyond the optimum time. As may be seen in the figure, apparent fractures are visible on the aluminum surface, due to its detachment from SU-8 and, most probably, to the one of SU-8 itself from the bottom Al metallization.
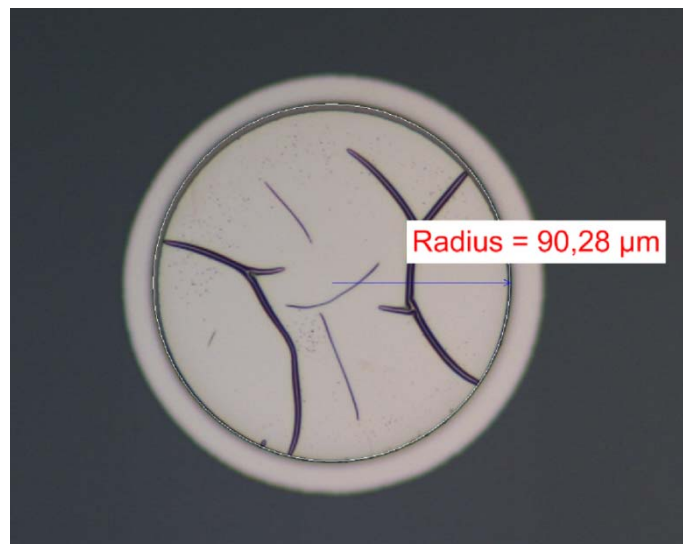
Fig. 3.26. Fabry-Perot interferometer subjected to 90 sec developer solution for removing the positive mask resist employed in the Al patterning

The second technique employed a RIE etching based on oxygen plasma (the same described in chapter 2 in the thinning of the carbon films) to remove the resist mask used for aluminium wet etching. This technique yielded better results compared to the former one, also in terms of robustness with respect to the process parameters, achieving a perfect removal of the positive resist with no trace of damage on the interferometers, as may be observed in Fig. 3.27, in which an optical image of Fabry-Perot interferometers after oxygen RIE stripping is shown.
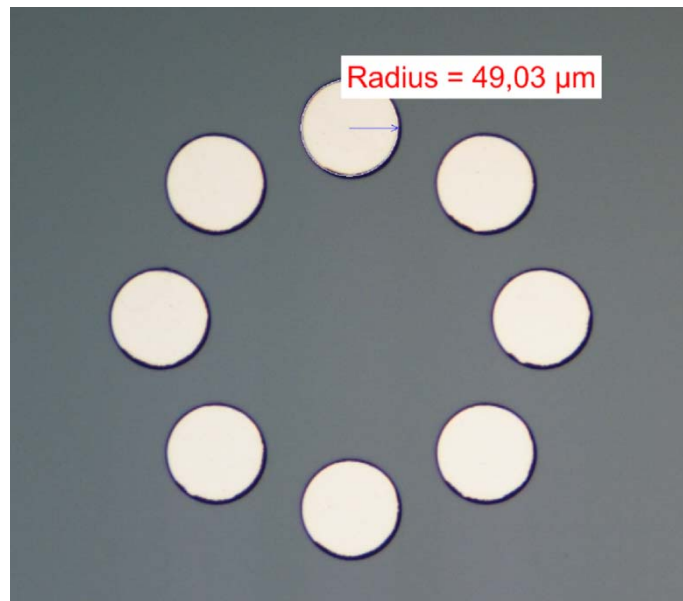
Fig. 3.27. Aluminum patterning by wet etching and subsequent oxygen plasma to remove the mask layer

In this second case, SU-8 photoresist itself was employed as a mask for Al wet etching on the interferometers. The same exposure time and baking process was utilized for both the structural and wet etching mask SU-8 layers, apart from the hardbake performed only on the former, quite obviously using an opposite mask tone in lithography. Since in this case no positive developer was needed, this method yielded the best results, leading to a perfect aluminium etching in correspondence with the Fabry-Perot, with complete removal of the 8 μm thick SU-8 mask layer by means of a 30 minutes oxygen RIE, a process showing high etching selectivity with respect to the bottom aluminium layer.

Scratch tests were realized on the patterned aluminium films on SU-8 obtained with the different techniques described, finding generally an acceptable adhesion, even if some interferometers were detached from the wafer during the tests, particularly in the receivers processed with the procedure based on positive resist development after etching.

In conclusion, the tests showed that, besides stripping solution, also positive resist developer is dangerous for the aluminium-polymer interface, so dry techniques like oxygen RIE removal of resist (of both positive or negative type) should be preferred. In order to pattern aluminium on SU-8 without using any development solution, selective deposition realized by the use of a micromachined shadow mask obtained by pass-through DRIE etching on a silicon wafer and aligned to the detectors' substrate by temporary wafer bonding could also be an

option, even though in this case a lower alignment accuracy should be expected compared to standard lithography.

Once solved the problems related to the processing of the interferometers, the fabrication of the ultrasonic receivers was completed with the final deep reactive ion etching step needed for the fiber housing. As already observed in the emitters' process, it was not possible to complete the pass-through silicon etching in the circular geometries with diameter smaller than 300 μm because of the DRIE rate dependence on the exposed area. The maximum etching time is, in fact, limited by the rate of larger structures realized on silicon membranes, in which the etching must not extend to the entire wafer thickness, and this made impossible to continue silicon removal in the smaller structures. This problem will be thoroughly discussed in the next chapter, in which specific tests aimed at deriving the effective DRIE rate dependence on the feature size will be described and alternative solutions that can allow the simultaneous fabrication MOMS-based devices of a sizes broad range, thus overcoming the most critical aspects related to the integration of the emitters and the detectors on the same micromachined support.

3.6   Acoustic Characterization

As described previously, the use of a tunable laser source is of primary importance in order to determine the operation wavelength assuring the best optical behaviour of the ultrasonic receivers. This working point should be chosen in order to guarantee both high sensitivity and linearity in the optoacoustic function, the latter property being important to avoid distortion of the detected ultrasonic wave. A TSL-210H laser, produced by Santec, was employed in the acoustic characterization to interrogate the Fabry-Perot cavity. This toll is a semiconductor laser that can emit a variable optical power which may be increased up to 50 mW over the full wavelength tuning range. The high power generated can be very useful in the measurements because it may allow overcoming possible attenuations and optical energy losses due to the fiber connectors, assuring an adequate optical intensity on the detector. The tuning range,

TSL-210H laser

extended from 1510 nm to 1580nm, is wide enough to permit the localization of the best

working condition for optoacoustic sensitivity, according to the procedure introduced in section 3.3. Moreover the Santec laser provides a coherence control that may be used to enlarge the spectral width of the laser line up to 200 MHz, which enables controlling energy attenuation due to optical interference effects in long fibers by decreasing the coherence length of the radiation.

Thanks to the technological advancements achieved in the field of fiber-optic communications, the use of laser sources working in the infrared region represents in principle the ideal solution to allow a prompt applicability of the developed technology. In fact, a C-band telecommunication IR laser, presently available on the market at a reasonable price, would satisfy the power and tunability requirements needed for the correct operation of the MOMS.

The acoustic characterization of the interferometer prototypes realized was carried out by using the experimental setup shown in Fig. 3.28, available in the Ultrasounds and Non Destructive Evaluation Laboratory at the University of Florence.
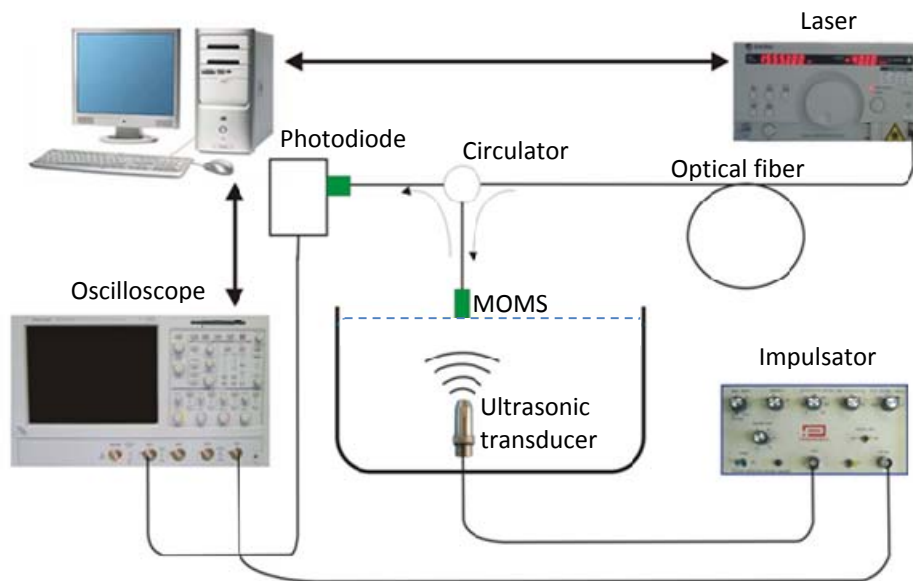
Fig. 3.28. Experimental setup for the detection of acoustic waves by MOMS based transducer

The tunable laser beam was guided up to the MOMS transducer through a single-mode optical fiber, characterized by a 125 μm cladding diameter. The reflected intensity was then separated from the incident beam by an optical circulator, a common optical component that allows separating waves travelling in opposite directions. In this way, the light generated

by the laser source was only transmitted to the MOMS and did not interfere with the reflected power measured by the InGaAs photodiode (PDA10CF), in which the reflected power was converted into a voltage signal by using a 10 kΩ transresistance gain amplifier. This photodiode provided adequate responsivity at the wavelengths of the tunable laser source (around 1 A/W) and 150 MHz bandwidth, assuring the correct detection of wideband ultrasonic signals as those generated by thermoelastic effect.

A trigger signal provided by an electronic impulsator was used to sample the sensing signal waveform with an oscilloscope at the right time immediately after ultrasound generation performed with a 10 MHz piezoelectric source. As seen in the previous fabrication process, the completion of silicon etching was not possible for structures with diameter smaller than 300 µm because of the too different etching rates between large and narrow geometries. As a consequence of that, all the available prototypes with Fabry Perot realized on dielectric membrane in this first fabrication batch had a quite large diameter (at least 400 µm). For this reason, in order to enable the acoustic characterization of the fabricated detectors, a capillary was used in order to fit the thin single mode fiber to the housing diameter. In fact, the insertion of the fiber into a much larger cavity without mechanical adaptation would result in a considerable power reduction because of oblique incidence of the laser light on the interferometric cavity that would drastically decrease the amount of optical power reflected from the interferometer and collected by the small fiber core (smaller than 10 µm in diameter). The employed capillary inserted within the fiber housing is shown in Fig. 3.29.

In order to correctly insert the capillary into the silicon cavity without damaging the relatively fragile dielectric membrane at bottom, a micrometric 3D positioning system was set up, including a stereoscopic viewer with variable inclination employed to visualise the capillaries and the fibers during insertion.

Once inserted within the housing, the capillary was fixed by using Torr-Seal epoxy glue, which, thanks to its high viscosity, assured a good mechanical strength without seeping into the cavity. This kind of glue, however, would not be adequate for insertion operation on MOMS characterized by a higher miniaturization because in the tests it was observed that the glue drop always invaded the surrounding region, making this kind of bonding technique unsuited to receivers arrays, where the cavities could be only few hundreds of microns apart from each other. This drawback, anyway, could be overcome by gluing all the devices of the

array simultaneously, possibly designing a tool that allows inserting all the optical fibers needed at the same time before sealing the cavities.
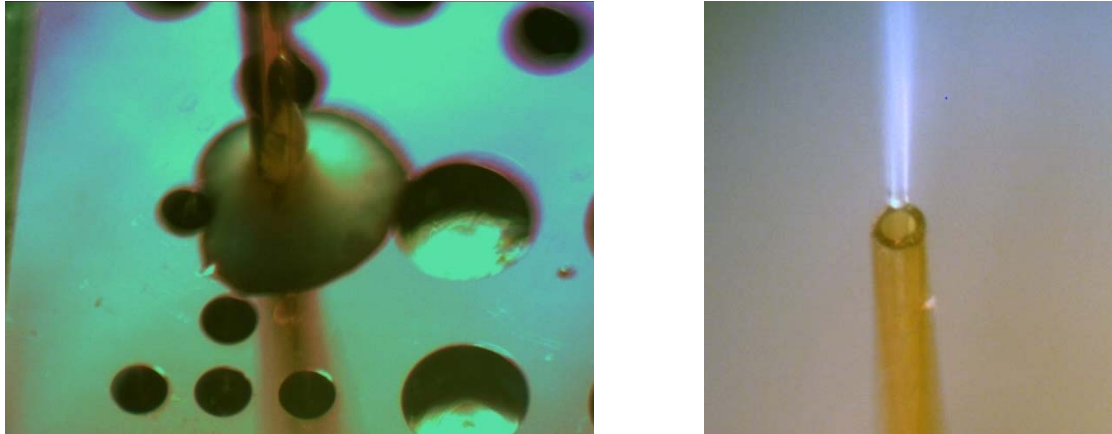
Fig. 3.29. Torr-Seal glue, roughly 600 μm diameter drop (a). Fiber insertion into capillary (b)

In order to develop a bonding technique suitable for smaller devices, the use of different glues was also investigated. In Fig. 3.30, for example, the best result obtained by cyanoacrylate glue can be observed. The minor density of the latter with respect to Torr-Seal permitted to reduce the flooding of the neighbouring regions thanks to the lower quantity of glue manually transferred to the MOMS device (a metal tip was used to drop the glue on the junction between the fiber and the MOMS). During the gluing operation, unfortunately, the cyanoacrylate penetrated slightly into the cavity but, as confirmed by experimental results, its presence did not interfere considerably with the functionality of the devices.
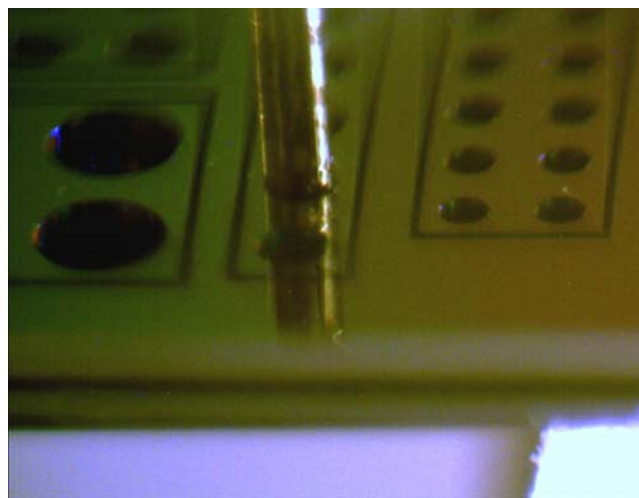
Fig. 3.30. Cyanoacrylate glue

Once fixed the capillary, the single mode fiber was inserted into it, as shown in Fig. 3.29b. This last operation was rather critical because, in performing the insertion, it was absolutely necessary to avoid any damage of the fiber tip (which may be easily take place by scraping against the capillary surface). The optical fiber, in fact, had to be previously lapped to guarantee a correct power transmission and a scratch of its tip would result in a drastic reduction of the optical power delivered to the interferometer.

The intensity reflected from a receiver deposited on dielectric membrane (with 300 μm diameter Fabry Perot on a larger membrane) was initially acquired without applying any pressure, in order to experimentally determine its modulation depth. The signal measured with the photodiode while the frequency of the laser source was ramped at a constant rate from the minimum to the maximum wavelength and vice versa, is reported in Fig. 3.31. In the subsequent tests, the wavelength was properly tuned in the working range of TSL-210H in order to have several interference fringes on the reflected spectrum.
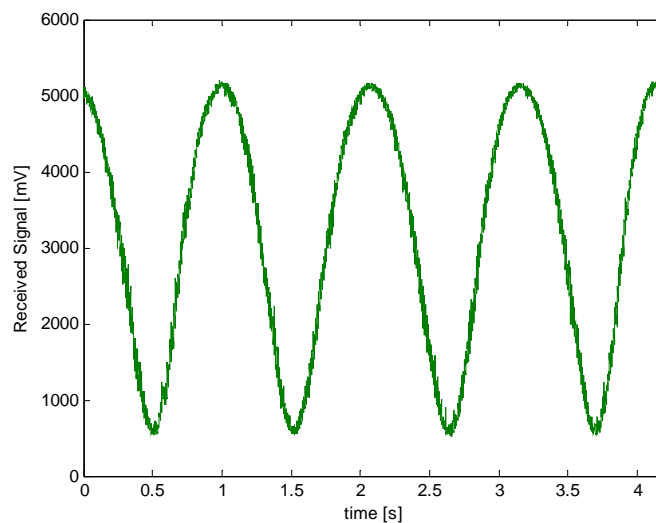
Fig. 3.31. Signal measured by the photodiode by ramping the wavelength of the tunable laser at a constant rate (with a power level of 4mW)

$$D = \frac{V_{max} - V_{min}}{V_{max} + V_{min}} = \frac{5160 - 580}{5160 - 580} \cong 0.8$$

The experimental results substantially confirmed the theoretical expectations concerning the optical behaviour of the interferometric detector, since they yielded a modulation depth around 80 % for a Fabry-Perot realized on dielectric membrane with 10 nm of aluminium as

first metallization. In this respect, it must be said that, although the experimentally observed interference pattern was coherent with the simulations, the optical power measured was lower than that expected. In fact, a voltage of 40 V should be theoretically detected by applying a 4 mW laser power and considering a total reflection (without accounting for the 10 volts maximum output of the PDA10CF).

However, the several fiber connections existing in the experimental setup, introduced significant optical losses, attenuating the laser radiation above all when the fibers were not perfectly terminated. Since the power measured was about 15% of the theoretical maximum it is quite clear that the power transmission efficiency could be sensibly increased by terminating the fibers with more advanced and automated methods (fiber termination was performed lapping the fiber tips by hand in these experiments). With respect to detector performance, this problem does not impact acoustic characterization in which the actual incident optical power can be accounted for as a multiplicative factor in the estimation of acoustic sensitivity.

These acoustic tests, performed once determined the wavelength that allowed for reaching the highest sensitivity, were carried out by using a 10 MHz Panametrics ultrasonic source to generate incoming acoustic waves (see Fig. 3.32).
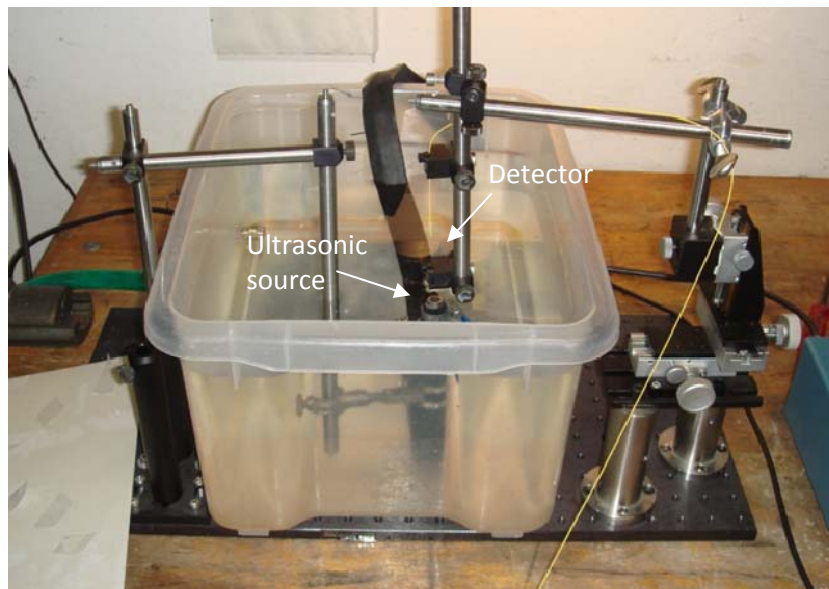
Fig. 3.32. A 10 MHz Panametrix transducer is used to excite the MOMS-based detector

The signal acquired through the MOMS device, at 1.4 cm from the source, is shown in Fig. 3.33. In the measurement, the Fabry-Perot was interrogated by applying a 4 mW laser power, resulting in a voltage signal with 200mV peak to peak amplitude from the photodiode/transresistance amplifier system. The correct distance between the acoustic source and the interferometer was calculated by considering the acoustic wave speed in water and observing the time elapsed from the generation of the ultrasonic pulse and the sensing signal rising edge on the oscilloscope.
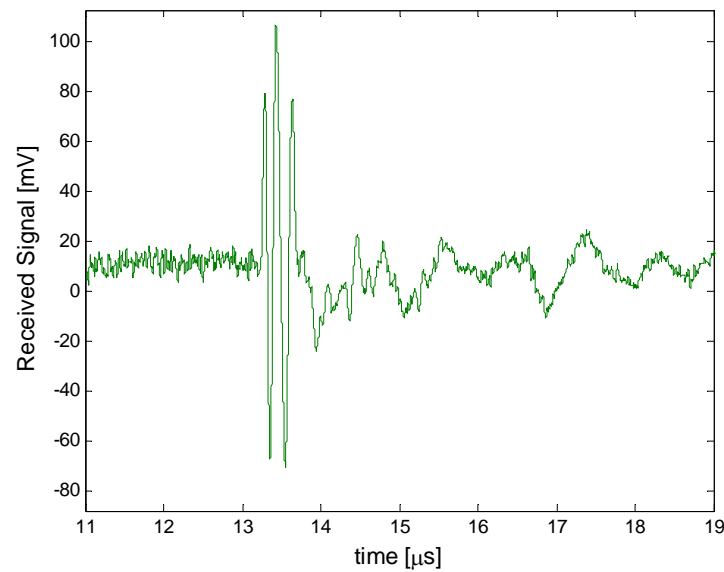
**Fig. 3.33. Acoustic wave detected by an interferometer on dielectric membrane
(consisted from 10 nm Al, 8 μm SU-8, 50 nm thick Al)**

The decrease in acoustic sensitivity taking place when the detector operated far from the optimal wavelength can be observed in Fig. 3.34. As may be observed, the peak to peak amplitude appears sensibly reduced due to the lower slope of the optical function at the wavelength employed.

In conclusion, the characterized interferometers provided a typical sensitivity of roughly 0.20 V/MPa, considering approximately a 1MPa peak to peak signal incoming on the detector. The pressure applied was measured by using the membrane hydrophone described in the previous chapter. Anyway, it has to be observed that the different active areas of the two sensors could lead to an imperfect estimation of the real pressure incident on the Fabry-Perot. The acoustic sensitivity can be also expressed without considering the diode gain, leading to a value of 20 μW/MPa.
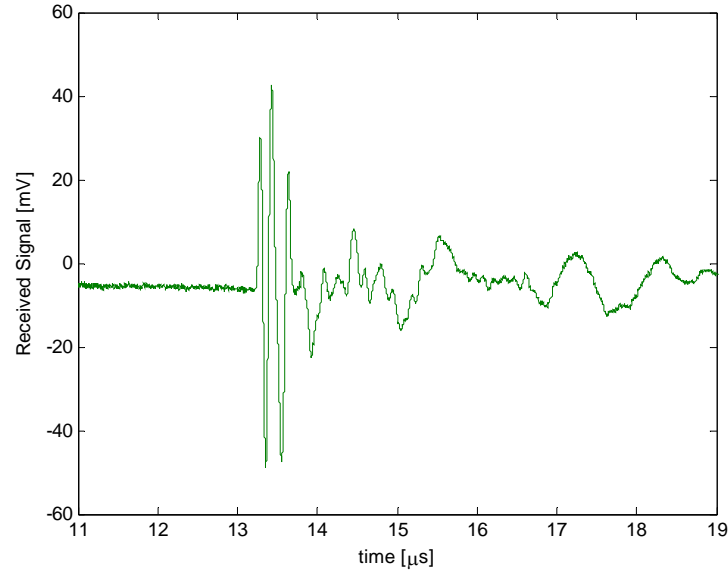
Fig. 3.34 Acoustic wave detected by interrogating the MOMS at a wavelength far from the optimum value for acoustic sensitivity

As a whole, it may be concluded that the experimental results confirm the theoretical expectations derived by the acoustic and optical modelling performed with parameters extracted from the optical measurements. In fact, the optical sensitivity of 9.2 μm^{-1} and the deformation of 9 nm/MPa, previously derived in the presented models, yield to a calculated value for the voltage/pressure sensitivity quite close to the one obtained in the measurements, namely:

$$S = I_o \, G \, \frac{dI_R}{dL} \frac{dL}{dP} \cong 0.15 * 4 \, mW \cdot 10^4 \frac{V}{W} \cdot 9.2 \, \frac{1}{\mu m} \cdot 9 \frac{nm}{MPa} = 0.49 \frac{V}{MPa}$$

where I_0 and *G* are respectively the incoming power on the detector and the transresistence gain of the photodiode, and *L* is the polymer thickness. The 0.15 multiplicative term was considered to keep into account the optical losses in the fiber connections and the coupling with the laser beam (such parameter was chosen based on the power measured with the photodiode in the experiments, as explained before). The discrepancy between theoretical and experimental data is acceptable, especially taking into consideration the fact that an accurate measure of the optical power incident on Fabry-Perot was not possible with the available setup and that the photodiode performances were taken from the datasheet and not measured.

As observed by the above calculation, acoustic sensitivity should be easily tunable by changing the laser power, providing the possibility to further improve the detection performance, if necessary. As a whole, the obtained results are very encouraging because they demonstrate that the optoacoustic detection of ultrasonic signals with high sensitivity is possible using a fiber optic silicon MOMS, and, more importantly, that the spatial resolution of the sensing, which is related to the detector size, can be sensibly increased without decreasing the acoustic performance (the pixel size in the measured devices actually corresponds to the active area of the sensor, that should in principle coincide with the 8 μm core diameter of the single-mode fiber).

Bibliography

[1]   B. T. Cox and P. C. Beard, "The frequency-dependent directivity of a planar fabry-perot polymer film ultrasound sensor", *IEEE Transactions on Ultrasonics, Ferroelectrics, and Frequency Control*, vol. 54, no. 2, pp. 394-404, 2007.

[2]   P. Morris, A. Hurrell, A. Shaw, E. Zhang, and P. Beard, "A Fabry–Pérot fiber-optic ultrasonic hydrophone for the simultaneous measurement of temperature and acoustic pressure", *J. Acoust. Soc. Am.*, vol. 125, no. 6, pp. 3611-3622, 2009.

[3]   Y. Hou, S. Ashkenazi, S. Huang, and M. O'Donnell, "An integrated optoacoustic transducer combining etalon and black PDMS structures", *IEEE Transactions on Ultrasonics, Ferroelectrics, and Frequency Control Society*, vol. 55, no. 12, pp. 2719-2725, 2008.

[4]   P.C. Beard, F. Perennes, and T.N. Mills, "Transduction mechanisms of the Fabry-Perot polymer film sensing concept for wideband ultrasound detection", *IEEE Transactions on Ultrasonics, Ferroelectrics and Frequency Control*, vol. 46, no. 6, pp. 1575-1582, 1999.

[5]   P. C. Beard and T. N. Mills, "Extrinsic optical-fiber ultrasound sensor using a thin polymer film as a low-finesse Fabry-Perot interferometer", *Applied Optics*, vol. 35, no. 4, pp. 663-675 , 1996.

[6]   S. Wang, P. Campistron, J. Carlier, D. Callens-Debavelaere, et al., "SU-8-based nanocomposites for acoustical matching layer", *IEEE Transactions on Ultrasonics, Ferroelectrics and Frequency Control*, vol. 56, no. 7, pp. 1483-1489, 2009.

[7]   K. Ohta and H. Ishida, "Matrix formalism for calculation of the light beam intensity in stratified multilayered films, and its use in the analysis of emission spectra", *Applied Optics*, vol. 29, no. 16, pp. 2466-2473 , 1990.

[8]   K.Ohta and H.Ishida, "Matrix formalism for calculation of electric field intensity of light in stratified multilayered films", *Applied Optics*, vol. 29, no. 13, pp. 1952-1959 , 1990.

[9]   E. Centurioni, "Generalized matrix method for calculation of internal light energy flux in mixed coherent and incoherent multilayers", *Applied Optics*, vol. 44, no. 35, pp. 7532-7539 , 2005.

[10] C. Katsidis and D. Siapkas, "General transfer-matrix method for optical multilayer systems with coherent, partially coherent, and incoherent interference", *Applied Optics*, vol. 41, no. 19, pp. 3978-3987 , 2002.

[11] H. Ehrenreich, H. R. Philipp, and B. Segall, "Optical Properties of Aluminum", *Physical Review* , vol. 132, no. 5, pp. 1918–1928 , 1963.

[12] A. G. Mathewson and H. P. Myers, "Absolute Values of the Optical Constants of Some Pure Metals", *Physica Scripta* , vol. 4, no. 6, 1971.

[13] D. Y. Smith, E. Shiles, and M. Inokuti, "The optical properties of metallic aluminum", in *Handbook of optical constants of solids, Volume 2*.

[14] J. M. Shaw, J. D. Gelorme, N. C. LaBianca, W. E. Conley, and S. J. Holmes, "Negative photoresists for optical lithography ", *IBM Journal of Research and Development*, vol. 41, no. 1-2, pp. 81-94, 1997.

[15] G. Voskerician, M. S. Shive, R. S. Shawgo, H. von Recum, et al., "Biocompatibility and biofouling of MEMS drug delivery devices", *Biomaterials*, vol. 24, no. 11, pp. 1959-1967, 2003.

[16] G. C. Hill, R. Melamud, F. E. Declercq, A. A. Davenport, et al., "SU-8 MEMS Fabry-Perot pressure sensor", *Sensors and Actuators A: Physical*, vol. 138, no. 1, pp. 52-62, 2007.

[17] S.-X. Wang, J. Carlier, A. Ndieguene, P. Campistron, et al., "Stiffness controlled SU-8-based nanocomposites: Application for 1 GHz matching layer conception", in *Ultrasonics Symposium, 2008. IUS 2008. IEEE*, pp. 678-681.

Ultrasounds Emission and Detection by Highly Miniaturized MOMS Devices Self-Standing on Optical Fiber

4

4.1 Introduction

The design and fabrication of acoustic probes suited to emit and detect high frequency ultrasonic signals represent the main objective of the research activity presented in this thesis. However, the two process flows analyzed in the previous chapters, for the development of generators and detectors, have shown several critical aspects related to the possible development of an integrated process. For instance, the Fabry-Perot interferometers employ single-mode fibers, which usually have a cladding diameter of 125 μm, but may be even smaller (80 μm for example). The emitters utilize, instead, multimode fibers that allow to avoid focusing too much optical energy in a narrow region of space on the emitter. This is important since the high power of the nanosecond pulsed laser source, used for acoustic generation, could melt or ablate the absorbing film, resulting in the breakdown of the device. Small single-mode fibers of 125 μm cladding diameter are certainly suitable for the detectors, but cavities with larger size suited for the ultrasonic sources must be included in the MOMS. Moreover, the need to realize optoacoustic devices on both silicon and dielectric membranes further complicates fabrication.

As described earlier, the deep reactive ion etching process presents a rate which strongly depends on the size of the etched region. A considerable overetching, which would be needed in order to realize pass-through cavities with very different diameter, does not represent a practical solution because it would most probably lead to damaging the dielectric membrane realized on the larger structures because of the limited selectivity of

the DRIE chemistry on silicon oxide. Therefore, the design of a process flow that permits the nearly simultaneous conclusion of silicon etching on different geometries is of primary importance to assure the feasibility of fabrication.

The critical aspects of two processes' combination will be here analyzed in detail. The design and fabrication of highly miniaturized acoustic probes, constituted by arrays of emitters and receivers, will be demonstrated, developing a MOMS technology suited to the full integration fiber lodgments with different size and, even more importantly, providing a technical solution for the problem of the separation of the MOMS devices from the micromachined wafer. In fact, the first emitters and receivers realized in the first batches presented in Chapters 2 and 3 were realized at the die level and their complete separation from the substrate was not strictly required to permit their acoustic characterization. On the contrary, the final devices must be released from the wafer after fiber insertion and the high miniaturization enabled by the MOMS technology adopted makes this operation quite challenging. In order to overcome such difficulty, a solution based on a particular type of front side micromachining enabling mechanical dicing of the micromachined devices from the substrate is proposed here, and its technological implementation described in the following.

4.2 Silicon DRIE Etching Lag

The dielectric membrane, constituted by a multistack containing thermal oxide, LPCVD nitride and LTO, is etched by the silicon DRIE process with a rate of roughly 35 nm/min. So, in performing the backside micromachining step, when the silicon substrate under the membrane is completely removed, the membrane itself begins to be etched and progressively thinned by the SF_6 plasma (in particular the first etched layer on the membrane backside is the 700 nm thick thermal oxide placed at the bottom of the stack). In case some of the membranes released on the wafer break due to the effect of DRIE overetching, a gas leakage in the cooling flow constituted by helium in the DRIE apparatus will appear. Since the effectiveness of cooling in the DRIE process (which is of fundamental importance to maintain the anisotropy of the etching) is measured through the helium gas pressure, when such pressure decreases too much the etching process cannot continue and is typically automatically stopped by the system.

Consequently, due to the spread of the DRIE etching rate depending on the size of the etched features, the fabrication of fiber lodgments with very different sizes, needed to integrate MOMS-based emitters and receivers, requires a rather precise estimation of the different etching rates. Once derived these rates, an appropriate set of lithographic masks can be designed to assure the almost simultaneous completion of silicon etching on different geometries and avoid the problem of helium losses that may stop the process prematurely. The accurate knowledge of silicon etching rate is less important for the devices realized on silicon membrane. In this last case (if the geometries are not excessively different in size, as actually happened in the mask set utilized for the early batches), an imperfect estimation of etching time may lead to different thicknesses of the silicon membranes, but without jeopardizing process feasibility in most cases. In order to exactly calculate the silicon rate, a 490 μm thick test wafer, appropriately patterned, was subjected to a 100 minutes long silicon etching. Moreover, the dielectric membrane on the front side was appropriately micromachined in order to allow the separation of the individual MOMS devices according to the process flow described in the next section. The MOMS structures, completely constituted by silicon, were then stuck to another silicon wafer used as a support and cut through a dicing tool with micrometric positioning capabilities. In this way, the cross section of the etched features could be observed by optical microscope and measured to derive their etching rate, as shown in Fig. 4.1 by way of example.

As may be seen in the picture, a silicon etching time of 100 minutes is definitely overestimated for the 250 μm large structures (placed at the center of the MOMS in the figure), but still does not permit the release of the smallest ones. Actually, after the DRIE, a remaining silicon layer (40 μm thick approximately), is still present at the bottom of the etched regions in the structures with diameter of 150 μm. Quite obviously, the differences between the rates become more pronounced when smaller geometries are considered. A map of silicon etching depths along the wafer referring to the 100 min etching described is depicted in Fig. 4.2.
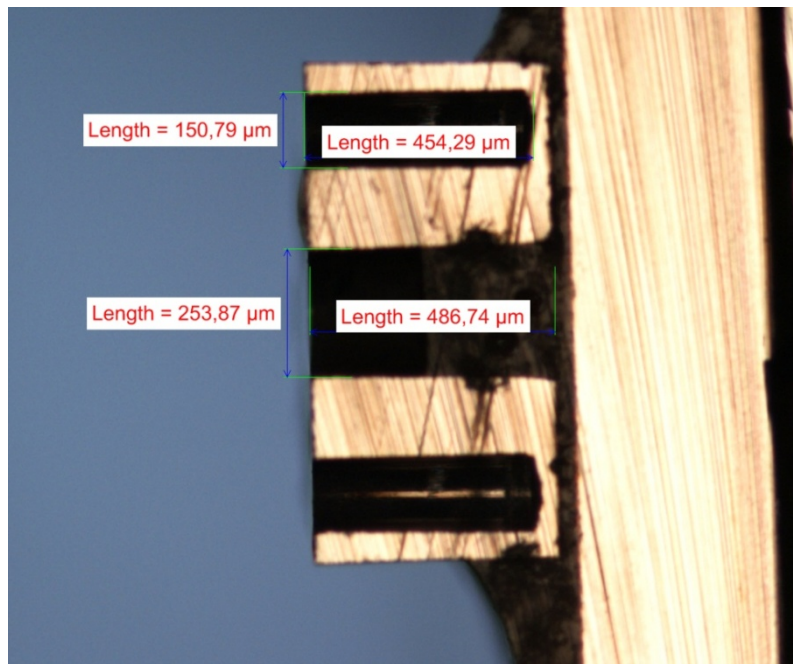
Fig. 4.1. Optical observation of a MOMS device cross section
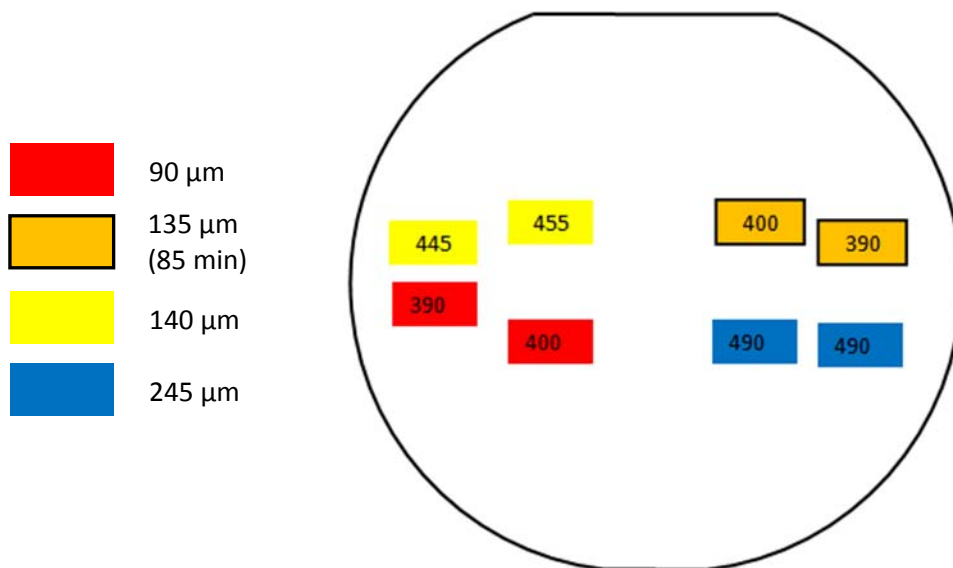
Fig. 4.2. Depths of silicon deep reactive ion etching after 100 minutes. Boundaries black highlighted for just 85 min etching time (490 µm thick silicon wafer)

As expected from theory, the silicon DRIE rate decreases slightly from the wafer center to the edge and, furthermore, the 90 µm large structures show a remarkable rate reduction to only 4 µm/min. The larger geometries with diameters of 140 and 245 µm, instead, have

etching rates of about 4.5 and 5.5 μm/min respectively. The last value was actually calculated by SEM measurements performed on a cross section realized on a silicon wafer with patterned features subjected to an etching time of 92 minutes (shown in Fig. 2.4). In this respect, it is important to observe that the rate is not constant in time in the various features, since it also depends on the etching depth and consequently decreases while the etching proceeds. Moreover, the density of the regions exposed to the sulfur hexafluoride plasma on the wafer surface can also affect the rates.

4.3   Process Flow

The considerable differences of silicon etching rates measured on etched features with different size have demonstrated that fabricating the MOMS devices needed for the integration of emitters and detectors on the same substrate is essentially impossible by using a double depth silicon etching like that presented in Chapters 2 and 3.

Consequently, a more complex process flow, that allows for a triple depth backside silicon micromachining has been designed in order to assure the fabrication of the self-standing integrated devices. The complete process flow is shown in Fig. 4.3. Starting from a 500 μm thick double polished silicon substrate (<100> oriented), a 700 nm thermal oxide layer is grown by wet oxidation at 1100°C (step 2). Then, a 300 nm thick silicon nitride film is deposited by LPCVD (step 3). Subsequently lithography and ICP SiO_2 etching are utilized to pattern the Si_3N_4/SiO_2 stack, removing the dielectric layers along donut shaped dicing regions designed all around the MOMS devices (step 4). Low temperature oxide is then deposited by CVD on both sides of the wafer (2 μm thick, step 5). Afterwards the backside is patterned by ICP SiO_2 etching (step 6), forming the first mask layer of the triple depth silicon etching

1. Silicon Bulk (500 μm)   2. Thermal Oxide (700 nm)

3. Silicon Nitride (300 nm)
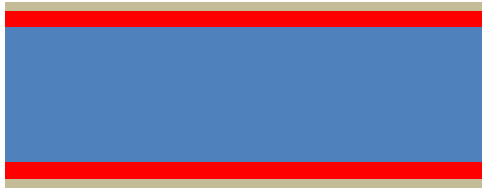
4. SiO$_2$/Si$_3$N$_4$ patterning
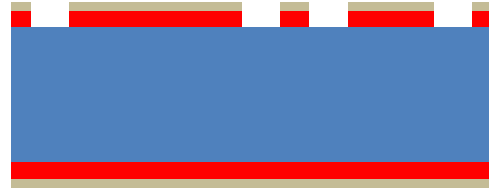
5. Low Temperature Oxide (LTO, 2µm)
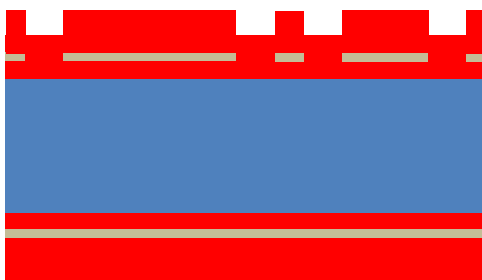
6. Back SiO$_2$/Si$_3$N$_4$ DRIE patternig
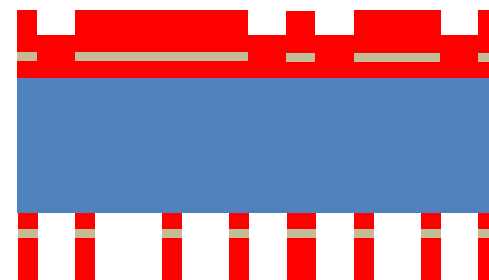
7. Polysilicon (100 nm)
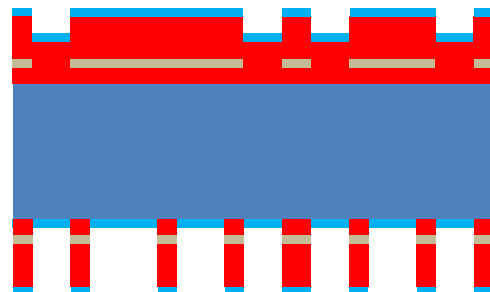
8. Back LTO (1.2µm)
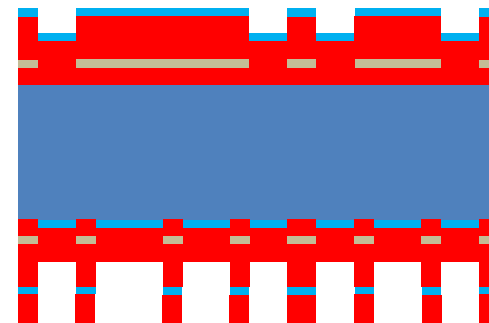
9. LTO patterning
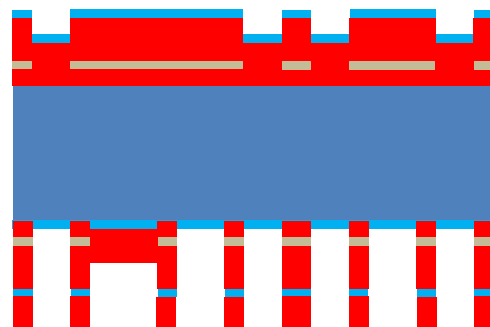
10. Back photoresist mask
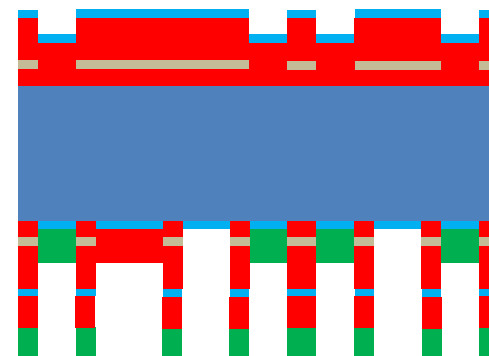
11. First DRIE (22 min) and resist stripping
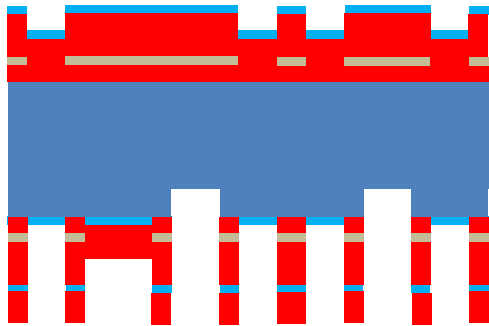
12. Second DRIE (23 min)
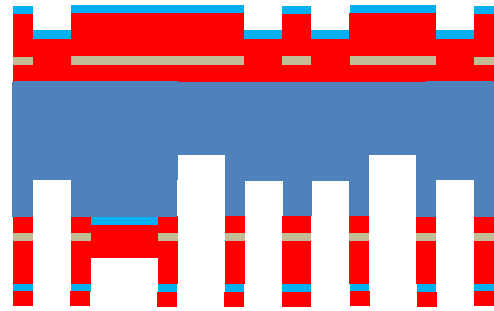
13. Back LTO DRIE etching
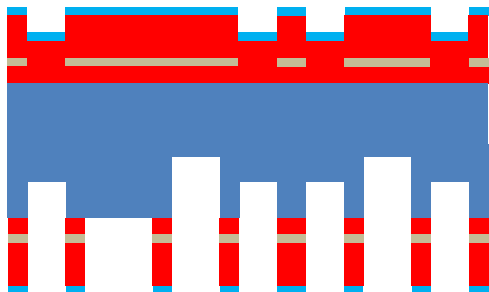
14. Wet Poly patterning
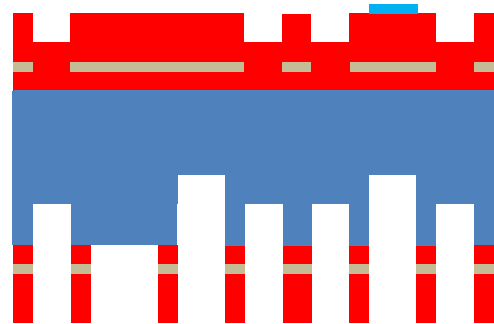
15. Front dielectric membrane patterning
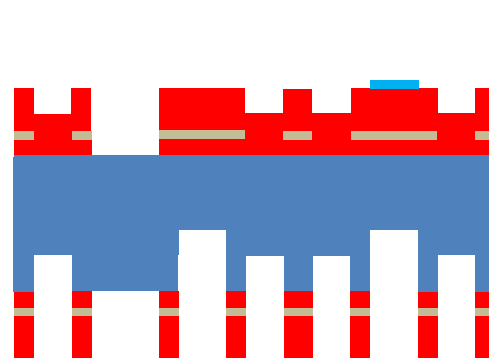
16. OiR Photoresist
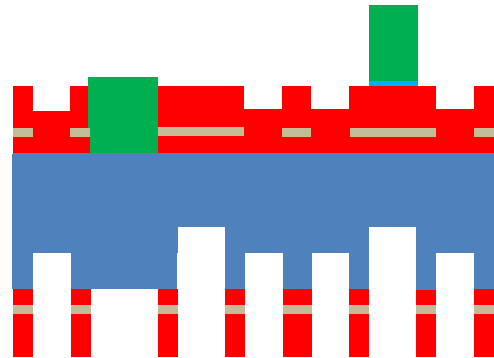
17. Resist carbonization

18. Al Evaporation (10 nm)

19. SU-8 resist (8 µm)

20. Al Evaporation (60 nm)

21. Wet Al etching (50 nm)

22. Final Silicon DRIE (76 min)

23. Fiber insertion

24. Devices separation
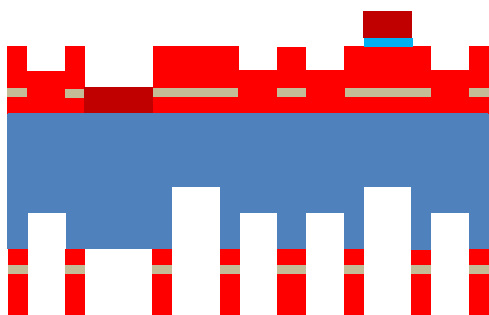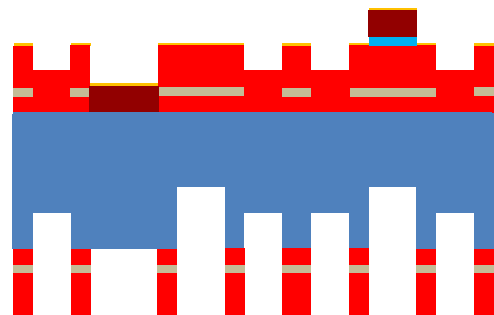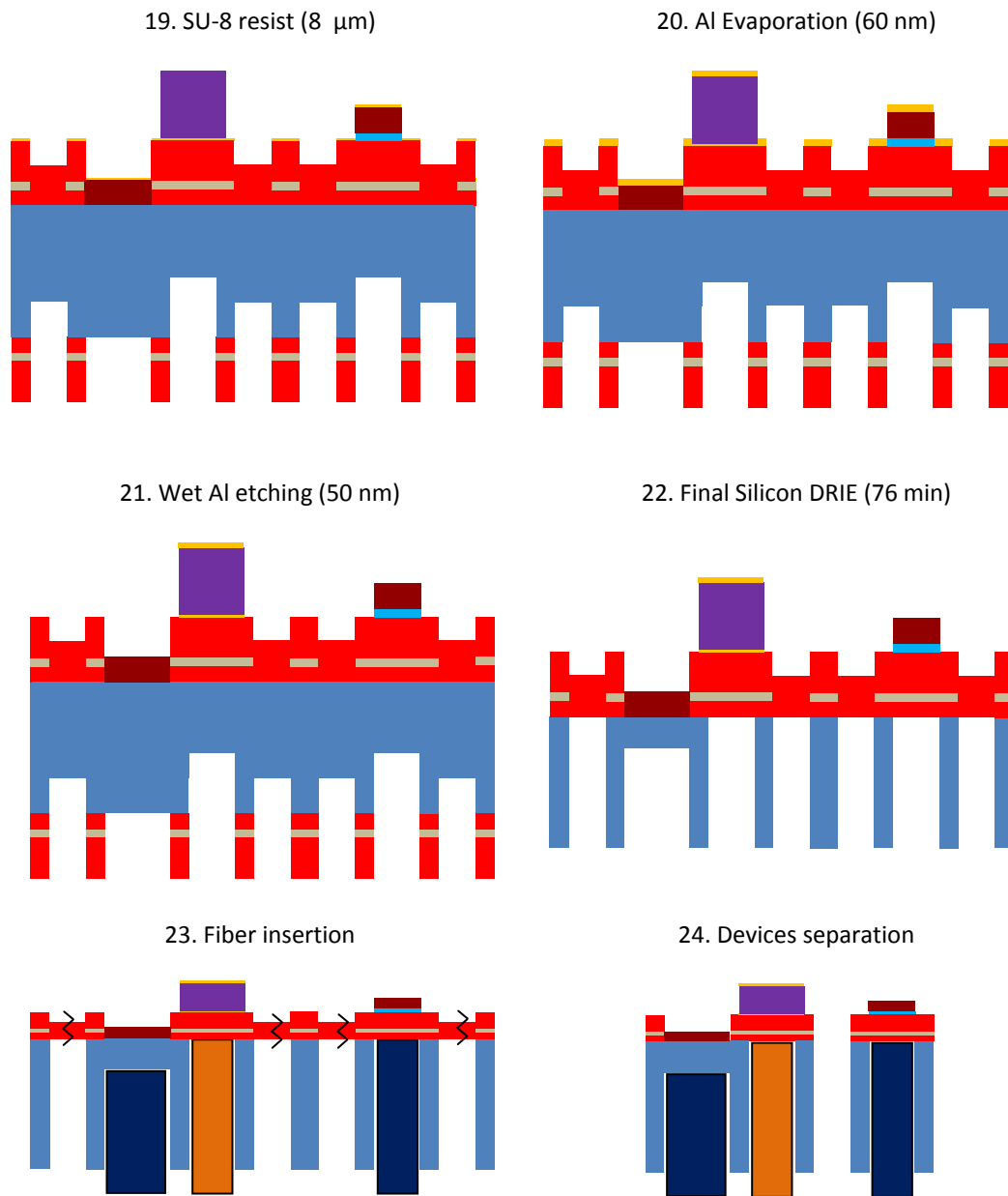
Fig. 4.3. Process flow for the fabrication of self standing MOMS devices on optical fiber

Subsequently, a 100 nm thick polysilicon layer is deposited by CVD (step 7). As discussed before, polysilicon is necessary in the emitters realized on dielectric membrane in order to assure a good adhesion of carbon. In this last process flow, polysilicon is also employed on the back side as an etch stop layer between the two oxide levels used in the backside hard mask. In fact, a 1.2 µm thick silicon oxide layer is deposited after polysilicon on the back side of the wafer and patterned by ICP etching (steps 8 and 9), contributing to constitute the

mask for deep silicon etching. Then, OiR photoresist is spun, completing the mask structure needed for the triple depth etching (step 10).

Once defined the backside mask, at step 11 the first silicon DRIE is realized, which begins the etching of the smaller structures designed on dielectric membrane (with diameter smaller than 150 μm). After this first DRIE, the photoresist is stripped, and a second etching step is carried out to define the structures on silicon and dielectric membranes with diameter properly chosen in designing the mask in order to achieve the desired etching depth (step 12). The remaining oxide mask layer is then removed from the backside by RIE etching (step 13). After that, the process flow continues with the same front side microfabrication flow separately described in Chapters 2 and 3 for emitters and receivers. Namely, the polysilicon is wet etched (step 14) and the dielectric membrane is patterned by ICP etching (step 15). Subsequently, the OiR photoresist is deposited by spinning, patterned (step 16) and carbonized (step 17), completing the front micromachining of the ultrasonic emitters. The Fabry-Perot needed to realize the receivers are then fabricated at the steps 18, 19 and 20 with the usual method. The removal of aluminum (step 21) can be realized by means of the first procedure presented in the last chapter (development of positive resist after etching to remove it) or by using SU-8 to mask the interferometer during aluminum etching. In this last case, however, the negative resist cannot be removed by oxygen plasma because of the presence of uncovered carbon on the wafer, since this RIE etching would remove it, as well. Anyway the second SU-8 layer used as a mask for Al etching, hard baked after the Al removal, can be left on the final interferometer without interfering considerably with the acoustic detection performances. In fact, from an optical point of view, the resist presence is absolutely not influential because the laser beam is totally reflected from the second thick aluminum layer. Acoustically, on the contrary, the second SU-8 could slightly decrease the sensitivity introducing a non negligible attenuation, especially at high frequencies.

The silicon etching is finally completed by backside DRIE at step 22, allowing the desired silicon removal on structures with different sizes. As can be observed at the step 23, related to fiber insertion, at this point of the process the MOMS-based acoustic probes are just sustained by a fragile 2 μm thick low temperature oxide membrane. On such membrane, the compressive stress of LPCVD SiO_2 is not balanced by the tensile stress of silicon nitride (as it happens in the designed dielectric membranes) and, consequently, the device can be easily separated by mechanical dicing (step 24), which can be done before or after fiber insertion,

as will be seen later on. The choice of depositing two microns of LTO, rather than 1 at step 5, can be motivated by the necessity to have a structure easy to break, but at the same time capable of assuring adequate mechanical robustness in sustaining the individual devices before dicing.

4.4 Fabrication Process

One of the most interesting aspects of the process flow discussed is represented by the triple depth silicon etching. An optical image taken from the back side of the wafer that allows for well appreciating the three different etching times is shown if Fig. 4.4, on a sample in which the second deep reactive ion etching was completed (step 12). As may be observed in the figure, the largest structure with diameter of 240 μm, designed to realize an ultrasonic emitter by housing a multimode fiber, is still masked by silicon oxide.
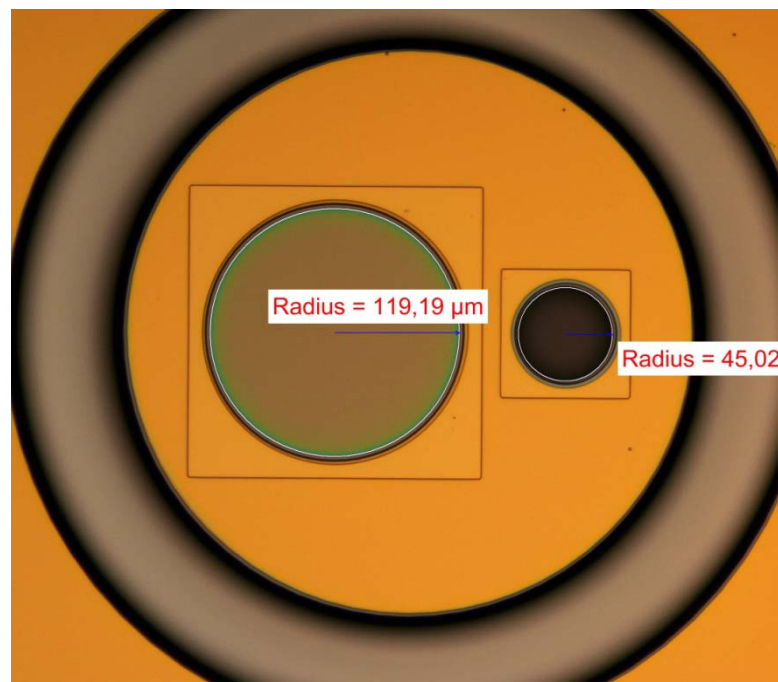
Fig. 4.4. Backside view after deep reactive ion etching (step 12)

On the contrary, the 90 μm large structure, suitable for the insertion of a thin single-mode fiber (detector), had been already subjected to an overall 45 minutes DRIE silicon etching, operated in two subsequent steps of 22 and 23 min respectively. The measured etching rate,

after the first 22 min, was considerably high, leading to an approximately 135 μm deep cavity. This confirms the theoretical expectations, according to which the etching rate is dependent on the surface density of the exposed regions. During the first DRIE, in fact, only the smaller geometries were not masked and their density on the wafer was very low. Anyway, the rate decreased sensibly during the two other deep silicon etchings.

The etching rate was also high on the donut defining the dicing line used to separate the device from the wafer by breaking the fragile sustaining LTO membrane on the front side. As observable by less dark color, the donut was subjected only to the second DRIE and was etched for only 23 minutes. Anyway, its wide area resulted in a higher etching rate compared to the 100 μm diameter housing of the smaller fiber and, consequently, the masks were designed paying attention to covering all the donuts during the first DRIE. The square visible in the optical acquisition is related to the patterning of an additional silicon nitride hard mask not described in the process flow, initially designed to permit the fabrication of funnel-shaped cavity conceived to ease the fiber insertion, as was verified on a test wafer (Fig. 4.5)
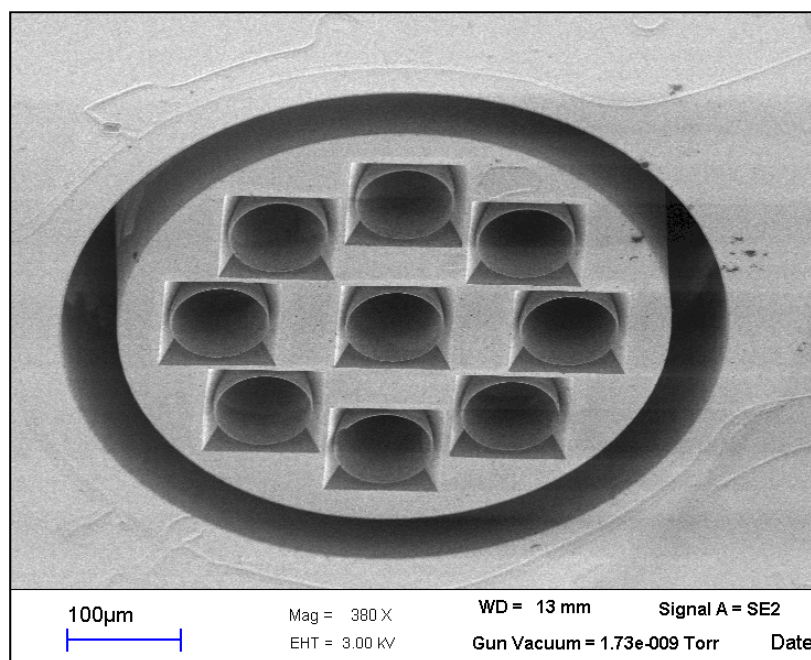
Fig. 4.5 SEM image of funnel-shaped silicon cavities for fiber housing

The funnel-shaped was obtained by initial DRIE and subsequently anisotropic TMAH etching of silicon, (TMAH stands for TetraMethylAmmonium Hydroxide) a wet etching solution whose rate is governed by silicon crystal plane orientation and so it is suitable for creating the funnel-shaped housing. During TMAH etching, the DRIE etched silicon walls have been masked by thermal oxide, some residues of which are visible in the SEM image. In this quite exotic process, the patterned nitride, which is not easily oxidized even in wet environment and at high temperatures, is used to prevent the oxidation of selected regions that have to be exposed to TMAH in the subsequent etching process. In this way, once the nitride mask is removed by RIE etching, all the surface of the DRIE micromachined wafer is passivated by oxide and consequently protected from TMAH, except for the areas previously covered by nitride that, on the contrary, are supposed to be exposed to the etching solution.

The described process was tested successfully, but as the first fiber insertion attempts pointed out that the optical fibers could be inserted into their micromachined housings rather easily, by using a stereoscope and an XYZ micrometric controller, even without funnel-shaped cavities, this solution was abandoned and the fabrication process simplified accordingly.

A few examples of MOMS devices obtained with the final process flow will be reported in the following, in order to show the miniaturization levels reached. In Fig. 4.6 (left), a highly miniaturized detector is reported; as may be observed, the diameter of the MOMS interferometer is only 250 µm. On the right side of the same figure, a really minimally invasive array can be observed. Such structure requires the use of a 4-core fiber, resulting in a small size device constituted by four sensors with and overall diameter of only 400 µm.

Fig. 4.6. Optical image of backside silicon micromachining

Coming back for a moment to the fabrication process, it can be seen from the flow presented earlier that the small geometries on silicon membrane are covered by silicon oxide (the second mask layer) during the first DRIE. This depends on the fact that the new masks designed for the triple depth fabrication process were initially conceived to fabricate emitters and detectors on the same wafer by double depth silicon etching, reducing to 200 µm the dimensional gap between the largest and smallest structures. Quite unluckily, only after the initial design of the new mask set the measurements of silicon etching rates on very deep features, as previously discussed, pointed out the inadequacy of the proposed solution and the necessity to design an additional mask to start the backside DRIE only on the smaller geometries (a solution that actually correspond to the triple depth silicon etching discussed in the process flow). In order to keep the compatibility with the old masks, but allowing the silicon membrane thinning on the smaller devices, the thickness of the second LTO layer used in the backside hard mask was appropriately chosen in order to be completely removed during the 45 minutes silicon etching performed in the first two steps of the backside micromachining and to allow the completion of the desired structures during the third DRIE step. However, as can be observed in Fig. 4.7, the removal of silicon dioxide by SF_6 plasma generated a not negligible roughness on the etched surface that is only partially attenuated during the prolonged etching process.

An optical image of the front side of the wafer after the second aluminum evaporation is shown in Fig. 4.8, where an array of three 240 µm large emitters and two detectors (140 µm diameter) is visible. As described in the process flow, different procedures can be employed to etch the second level aluminum. In order not to negatively affect the process yield, the quite delicate solution based on positive resist removal by post-etching exposure and development was not considered, preferring a more careful aluminum patterning performed by covering the Fabry-Perot with a further SU-8 layer on one of the two process wafers, and leaving the Al layer everywhere on the other. The second solution simplifies the processing and may also be interesting to enhance performances, since the Al film left on the emitters could allow for the use of thinner carbon films (up to few hundreds of nanometers), which could be obtained by oxygen plasma etching or carbonization of a thinner resist layer. This could be possible because, in the presence of the thick Al film on carbon, the optical power not absorbed during the forward propagation of the laser beam, would be back reflected and totally absorbed during its backward propagation. As a consequence of that, the

thermoelastic generation could be improved by the higher temperature increase reached in the carbon film by dissipation of roughly the same amount of power in a smaller volume.
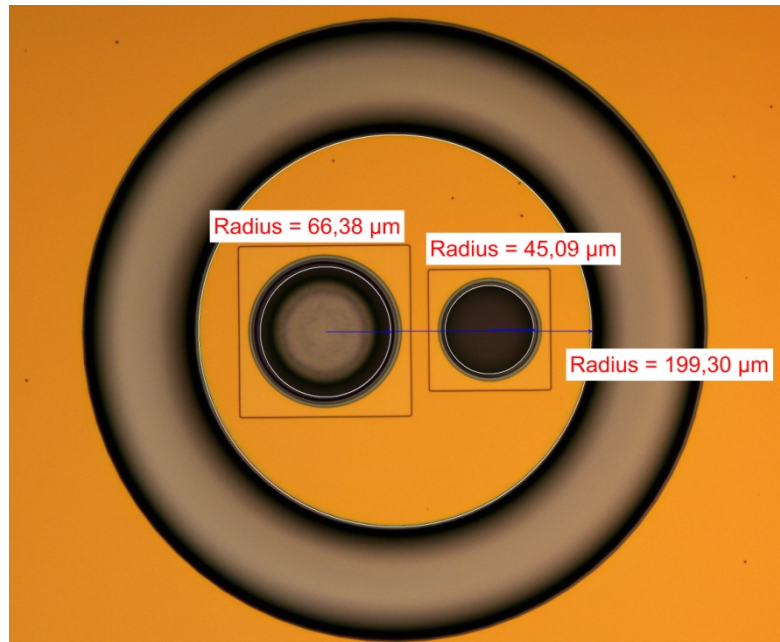
Fig. 4.7. MOMS-based array. Superficial roughness is visible on the left emitter, due to full removal of mask layer during the silicon DRIE
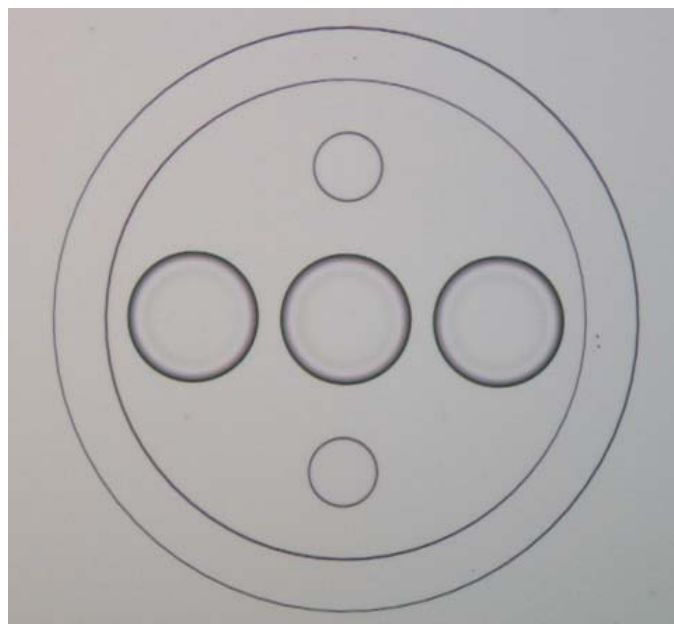
Fig. 4.8 Front side view of a processed sample after the 60 nm thick Al evaporation

A completed device is also shown in Fig. 4.9 observed after the aluminum removal and the conclusive backside silicon deep reactive ion etching. As may be seen in the reported image, thanks to triple depth etching silicon has been completely removed under the dielectric membrane, so that the light coming from the backside illumination of the microscope clearly penetrates through some areas of the structure. The smaller donut shape visible in figure around the structure delimits the region in which nitride has been removed from the front side, and a plain LTO membrane is present in order to ease mechanical dicing of the MOMS. Such suspension membrane, in other structures, has been extended to all the surrounding large donut region visible in the picture in order to investigate its impact on the dicing procedure. As can be observed in Fig. 4.10, in which the front illumination has been switched off in the microscope, the visible light coming from the backside illumination is totally absorbed by the carbon film. Other examples of individual acoustic devices are shown in Fig. 4.11. In this figure, a highly miniaturized emitter realized on silicon membrane is visible on the left. Its diameter is less than 300 µm, and it presents a micromachined housing suitable for a 125 µm multimode fiber with 60 µm core diameter.
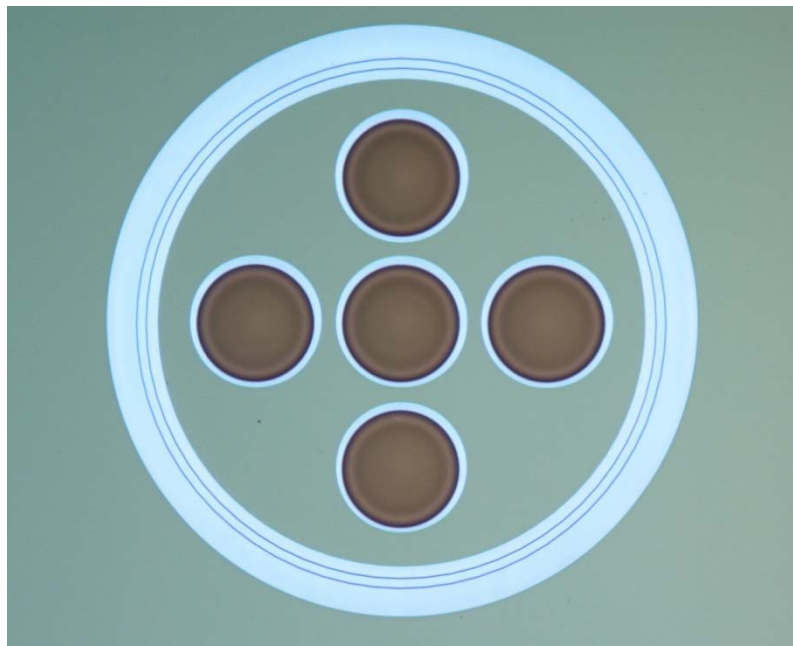
Fig. 4.9. Front side view of an array of 5 emitters

In this respect it must be said that, in designing these prototypes, particular attention has been devoted to the choice of the cavity diameter. In order to maximize the optoacoustic

conversion, the fiber housing should actually be slightly larger than its cladding in order to assure an easy insertion of the fiber and, at the same time, an efficient optical coupling with the active part of the sensor. Since an incidence of the laser beam too far from the normal direction with respect to the MOMS membrane would results in a considerable reduction of such coupling, particularly on the detectors, the size of the cavity should be only slightly larger than the fiber.

Fig. 4.10. Optical image of MOMS emitter without illuminating the frontside

This design rule has been considered on both emitters and receivers, such as the one reported on the right side of Fig. 4.11, in which the aluminum boundaries appear slightly notched because of some under etching taking place during the patterning of the thicker Al layer of the interferometers.
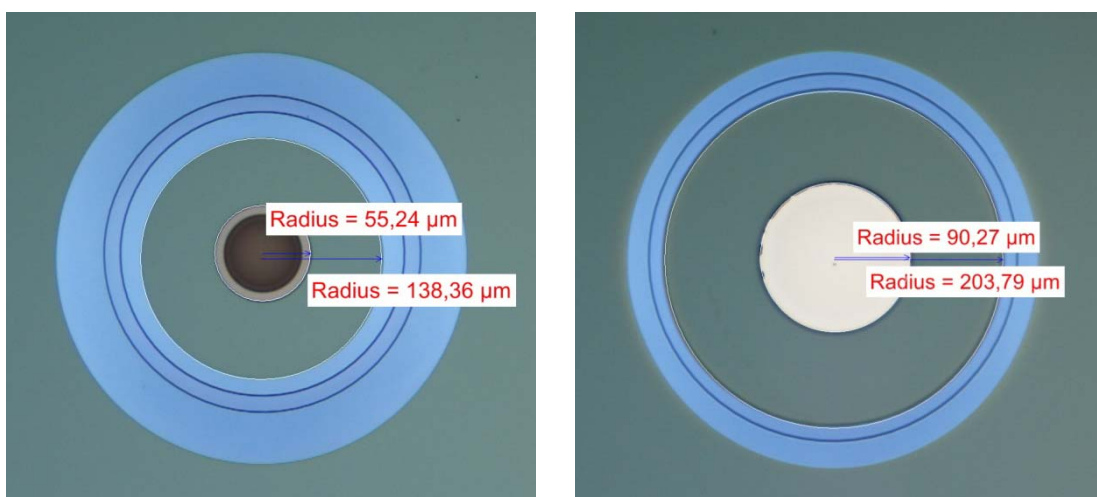
Fig. 4.11. Emitter (left) and detector (right) realized respectively on silicon and dielectric membranes

An array of five detectors, realized on dielectric membrane and suitable for use with a fiber bundle, is also shown in Fig. 4.11. In this case, as seen before for carbon, the backside light does not cross the thick aluminum and, consequently, the Fabry-Perot appears dark when the front side is not illuminated.
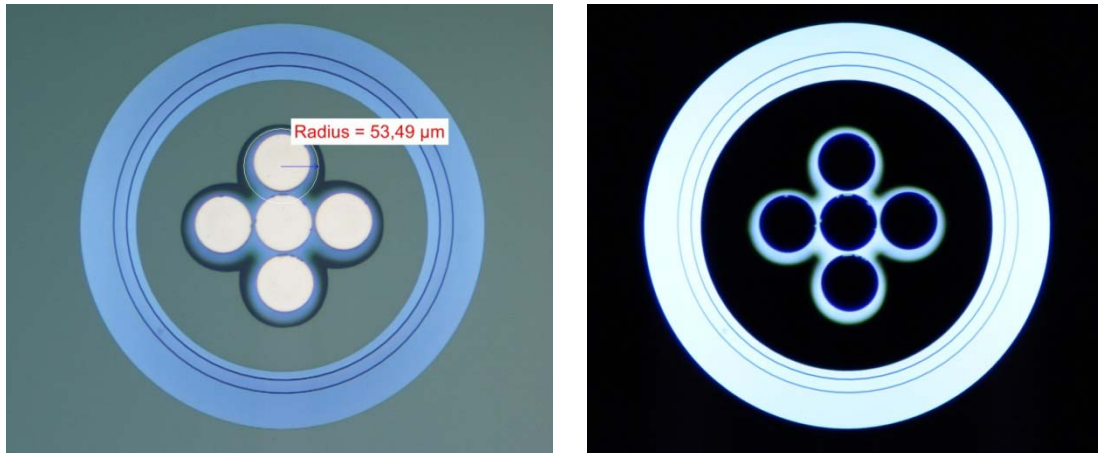
Fig. 4.11. Front side views of a MOMS array of five receivers, without illuminating the front side on the right acquisition

An example of emitters-detectors integration is finally shown in Fig. 4.12, reporting the optical image of a MOMS array in which the central emitter could be employed to generate the acoustic wave and the four detectors around it used to receive the signal reflected from the material or biological tissue under inspection. Since, as discussed before in this thesis, the detection of ultrasonic signals generated by direct photoacoustic emission from biological tissues is widely studied and has provided very promising results for medical diagnostics, MOMS-based devices that allow the detection of ultrasonic signals together with the direct laser irradiation of tissues have also been fabricated with the integrated process. For example, an array of 4 receivers, suitable for photoacoustic imaging, is shown in Fig. 4.13, in which the central fiber housing can be used to deliver a pulsed laser beam to the tissue, maintaining the light source at a well-defined distance for the detector array and simplifying the subsequent signal processing needed for imaging.

In a visionary perspective, such structure, if equipped with an adequate number of detectors, could be possibly used to locate a colony of cancerous cells by photoacoustic imaging and thermally destroy them heating the tissue in a controlled way by applying laser pulses with high repetition frequency. In doing this, photoacoustic imaging could be also exploited to perform a sort of thermography of the tissue during the thermal treatment, in

order to avoid necrosis phenomena due to excessive heating. Moreover, in this vision, the tissue ablation could be highly confined to the cancerous region, significantly improving the minimal invasiveness of the therapy.
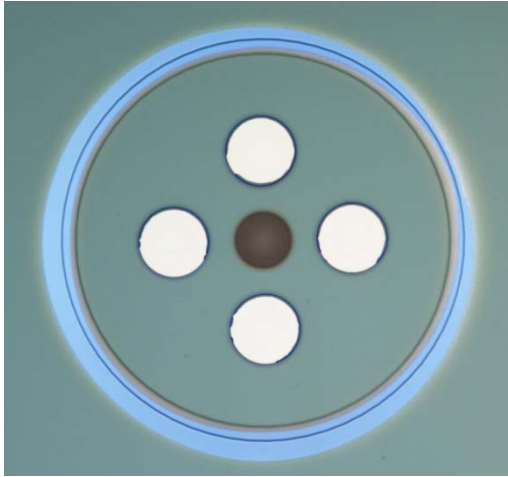
Fig. 4.12.Front side view of 1x4 emitter/receiver array realized on silicon membrane
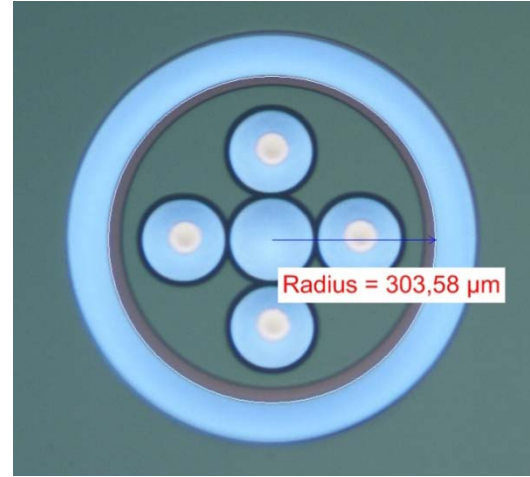
Fig.4.13.MOMS array suitable for photoacoustic application. The ultrasonic emission is realized by the material under inspection

Some other interesting optical images of devices realized on the wafer completed without the etching of the final aluminum layer are shown in the following, in which the buckling of the plain LTO supporting membrane in the MOMS can be appreciated (Figs. 4.14, 4.15 reporting backside and frontside views respectively). In Fig. 4.15, in particular, two acoustic probes constituted by an emitter and a receiver can be observed, where the emitter on the right has been designed with a square shape. Such emitter-receiver modules could be of concern for the "virtual biopsy" analysis previously introduced. The overall diameter of these MOMS is in fact less than 400 µm and would allow their insertion into syringe needles or catheters for minimally invasive diagnostic applications.

As may be observed in both figures, shadowing phenomena resembling stationary waves appear on the LTO donut shaped membrane located all around the circular devices due to the uncompensated compressive stress in this material. Such effect does not show on the compensated membranes constituting the actual devices, which indeed appear completely flat, thanks to the presence of the tensile Si_3N_4 layer in them.
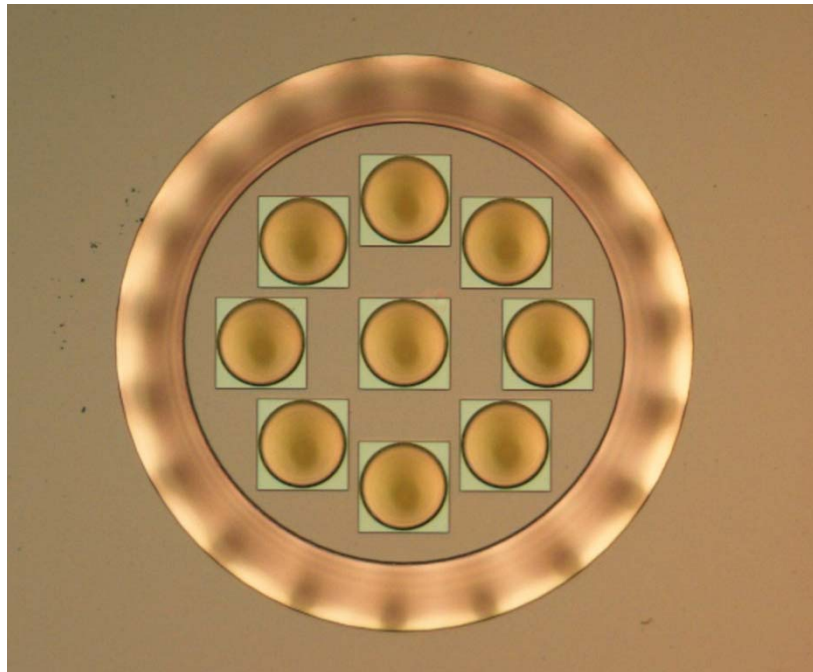
Fig. 4.14 Back side view of 9 receivers array realized on dielectric membrane (without aluminum patterning)

On the peripheral region of the MOMS, it was decided to remove the silicon nitride, despite the residual stress effects described, in order to ease the mechanical dicing of the devices. The reason beyond this was the fact that the dielectric membranes containing nitride are very tough mechanically and might be difficult to break on the dicing region. Therefore, a relatively thick LTO layer was chosen to anchor the devices to the substrate, which is much less resistant than the compensated membrane and can be easily broken by applying a slight mechanical pressure to the MOMS. Actually, when the fibers are appropriately inserted into the device, and glued on it, it is sufficient to lift the fiber slightly to release the device from the wafer. Despite this easiness in dicing, the low compressive stress of LTO (around 100 MPa) and its considerable thickness allowed it for having a sufficient mechanical stability to effectively support the devices during the whole backside DRIE release process without breaking, except for some isolated cracks appearing on the largest prototypes designed on the wafer, which however did not affect the process yield.
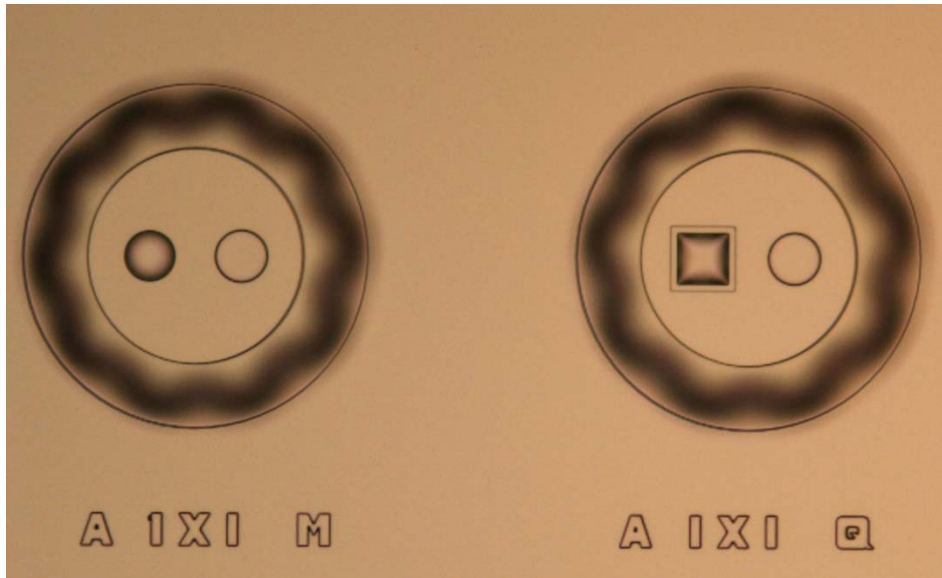
Fig. 4.15. Optical image of wafer front side (without aluminum patterning)

4.5 Fiber Insertion

As described in the former chapter, fiber insertion in the MOMS requires the use a micrometric position controller operated with the aid of a stereoscopic microscope. Using this technique, it is possible to insert the fiber into its housing directly operating on the wafer, but considering the fragility of the fabricated structures, a different technique was preferred in the tests described here. Namely, the MOMS were released from the wafer by using a piece of adhesive blue foil, of the type commonly used in wafer sawing. The blue foil was put in contact with the region of interest on the front side of the wafer and gently pressed in order to adhere to the desired MOMS, which were then removed by the substrate by slowly stripping the foil, remaining on it. In this way, the insertion of the fiber could be even carried out by working on an individual device by properly implementing the blue foil stripping procedure described. This was useful in the experiments because the glue deposition was made by hand, and working on a single MOMS allowed to avoid wetting the adjacent devices with the excessively large glue drops that were sometimes transferred on the bonded device.

When the insertion was realized at wafer level, as for the devices described in the two previous chapters, a mirror was employed to observe the front of the wafer during this

operation and detect the slight dielectric membrane deflection that took place when the fiber tip touched the bottom of cavity. This useful expedient (only utilized on devices realized on dielectric membrane) assured to place the fiber in contact with the sensor membrane and prevented an eventual damage of the MOMS by possible excessive pressure exerted on the dielectric membranes in the monolithic devices. This solution demonstrated to be no more necessary on the self standing devices, because a slight displacement of the blue foil surface was noticeable when the bottom of the cavity was reached, and this was sufficient to tailor the height of the fiber during positioning.

In Fig. 4.16, an array composed by three emitters and two detectors after release from the wafer by blue foil is reported by way of example. As may be observed, the boundary of the mechanically broken LTO oxide do no present a perfectly smooth geometry, but smoother shapes are achievable by using of the narrower donut regions described earlier.
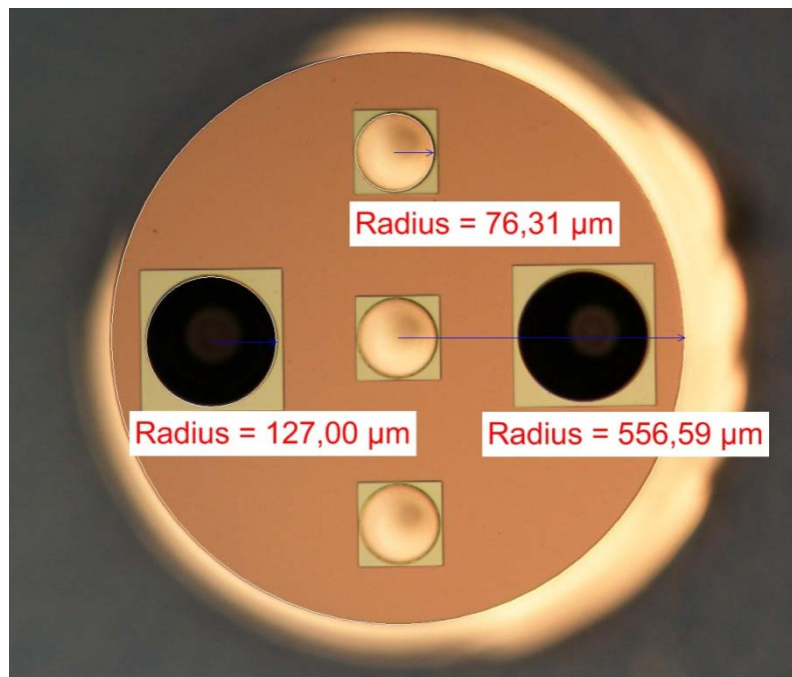
Fig. 4.16. Back side view of a MOMS array released from the wafer

A SEM image of an array of MOMS-based devices on blue foil, released from the wafer by applying a slight pressure on a whole die, is finally shown in Fig. 4.17. In this panoramic view, the fiber housings are clearly visible and, in particular, on the top of the figure acoustic

structures suitable for minimally invasive applications, constituted by coupled emitters and detectors of overall diameter less than 400 µm, can be observed.

Once removed the devices from the wafer with the blue foil, the optical fibers can be inserted into the cavities, as illustrated in Fig. 4.18. In doing this, the use of cyanoacrylate glue was preferred in the structures where the integration of several emitters and detectors was pursued. This decision was made because, as seen before, the Torr-Seal glue tends to invade the region surrounding the glued fiber and consequently limits the maximum integration reachable.
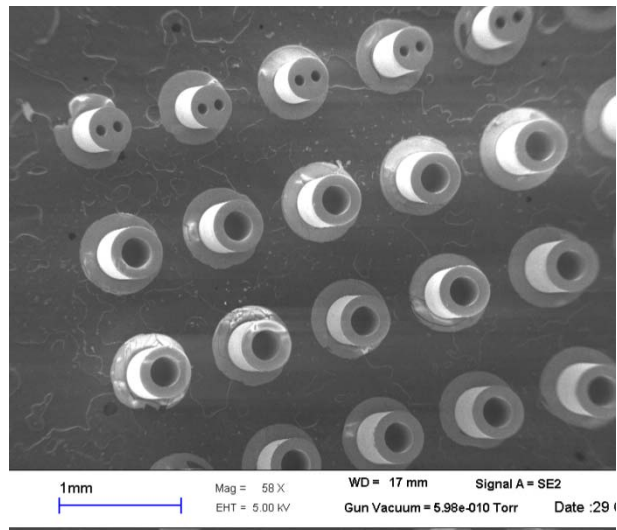
Fig. 4.17. Self standing devices released from the wafer
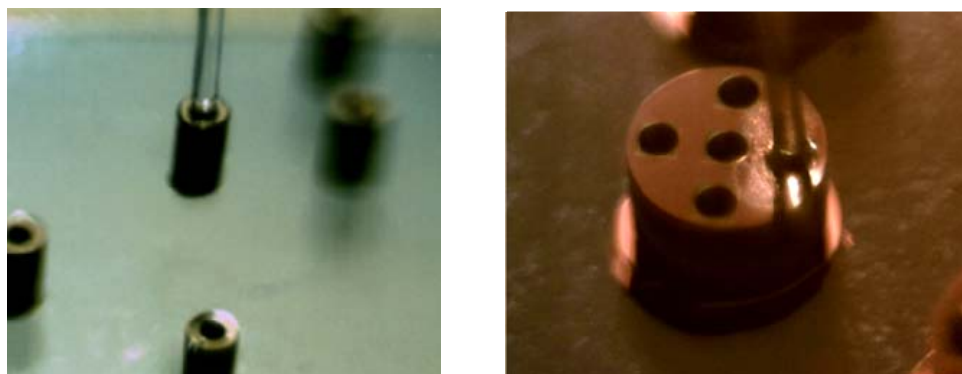
Fig. 4.18. Fiber insertion of self-standing MOMS devices on optical fiber

Once dried the glue, the MOMS device can be finally separated from the blue foil. In doing this, it is sufficient to exploit the micrometric positioning system to lift the fiber and detach the ultrasonic device.

In the following, a few examples of freestanding devices mounted on optical fibers with the described technique will be shown, in order to demonstrate the capabilities of the developed technology in terms of miniaturization and integration of several emitter and/or detector devices on the same probe. In Fig. 4.19, in particular, an ultrasonic detector with diameter smaller than 250 µm is shown, in which a 125 µm single-mode fiber was employed. Two examples of complete MOMS-based ultrasonic probes, containing both emitters and detectors, are instead depicted in the Figs. 4.20 and 4.21. In these devices, three emitters and two detectors are realized on the same device proving the possibility to integrate several ultrasonic emitters and detectors without significantly increasing the probe invasiveness.
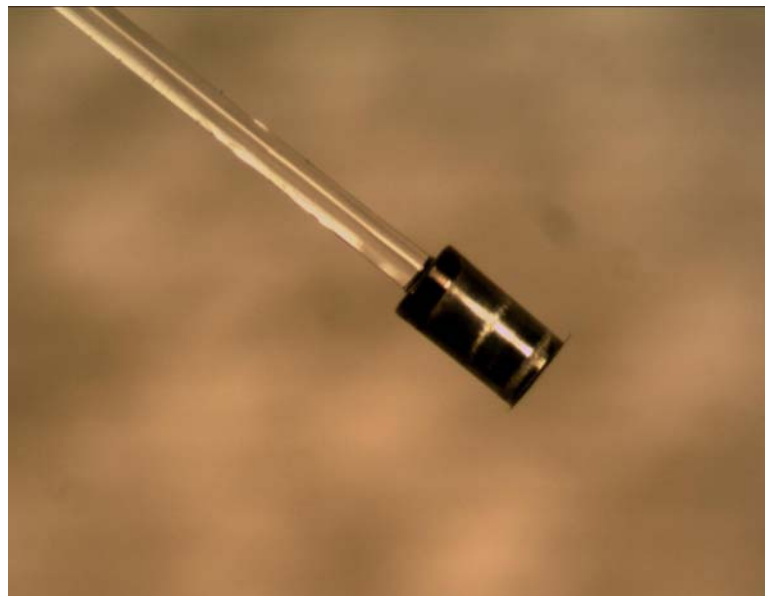
Fig. 4.19. Self-standing MOMS detector on optical fiber
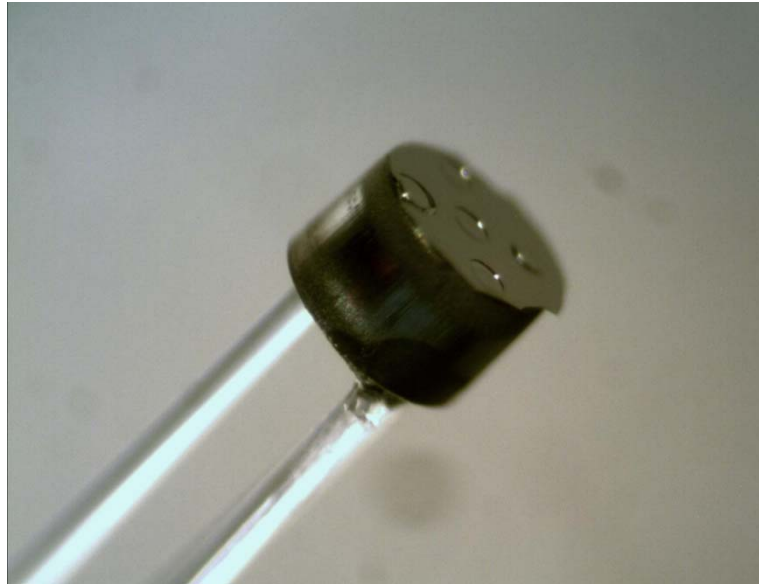
Fig. 4.20. Array of MOMS-based emitters and detectors

The fabricated array shown in the figures has actually a diameter of approximately 500 µm, sufficiently small to allow its insertion into a syringe needle or a catheter. In must be said, however, that, as mentioned before, the miniaturization level presented here does not represent the ultimate limit of the proposed technology. The opto-acoustic MOMS devices presented in this thesis, in fact, have been conceived to verify their possible use in high frequency ultrasonic applications, and consequently their design has been performed aimed at simplifying their acoustic characterization rather than pushing the integration level to the limit. In this respect, the use of multicore fibers, especially in the detectors where the active part of the device is limited to the few square microns corresponding to the fiber core diameter, would increase considerably the pixel density. In this way, the small MOMS could contain a large number of sensors, considerably improving the spatial resolution of the ultrasonic probe.
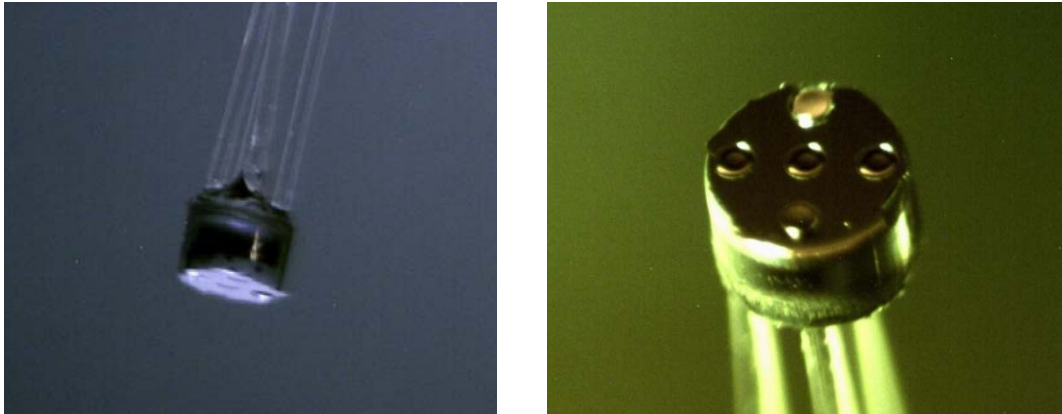
Fig. 4.21. Several views of MOMS-based emitters and detectors array

4.6 Acoustic Characterization

The acoustic performances of the self-standing microfabricated devices on optical fiber were finally characterized by measuring both emitters and detectors. The characterization of the freestanding detectors did not yield remarkably different results that the devices measured on chip and presented in chapter 3, so it will not be described here. However, the freestanding detectors were functional as the previously presented devices and provided similar performances. On the contrary, the ultrasonic field generated by the self-standing MOMS emitter on optical fiber was obtained using a smaller fiber with respect to the earlier acquisitions (230 µm instead of 630 µm) and consequently different results have been obtained.

The acoustic field generated by a freestanding emitter, realized on silicon membrane (with a diameter of 300 µm) and measured using the technique described in Chapter 2, is reported in Fig. 4.23. A multimode fiber (with 230 µm cladding) was employed for guiding the pulsed laser beam to the absorbing film. A needle PVDF hydrophone (SN1614) was, in this case, exploited to detect the laser generated ultrasound. In this experiment, a smaller size sensor (approximately 0.2 mm of diameter) was preferred in order to overcome the problem encountered during the characterization of the 700 µm emitters where the detector size (a membrane hydrophone) was quite comparable to the area hit by the generated acoustic field. As may be observed in the figure, most of the acoustic power is concentrated in a region much smaller than 1 mm^2, confirming the high spatial resolution reachable by the developed technology.
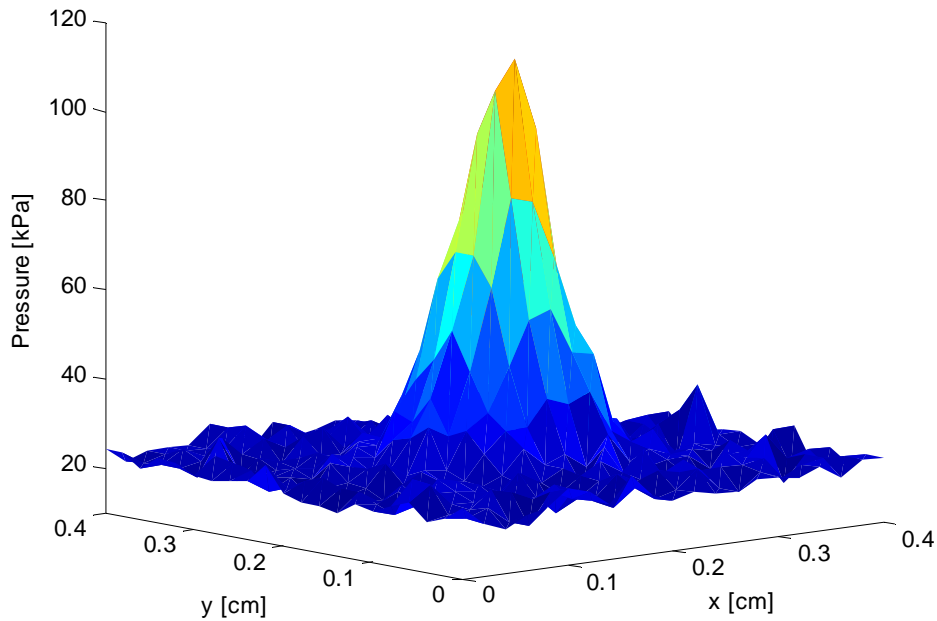
Fig. 4.22. Acoustic field measured by a PVDF hydrophone (at 8 mm far from the MOMS emitter)

The pressure measured, at a distance of 8 mm from the source, is roughly 110 kPa in the XY point of maximum intensity against the 0.5 MPa previously derived at the same distance for the large emitter. However, it must to be observed that such value might depend on the narrow bandwidth of the sensor employed, that cannot measure the pressure harmonics resulting from the high frequency components of the ultrasonic signal. The PVFD hydrophone is, in fact, calibrated by the constructor up to 20 MHz and the real bandwidth is actually unknown without a more accurate characterization. However, the considerable spatial focalization of the acoustic field made the use of the larger bandwidth membrane hydrophone available in the setup not appropriate in the measurements, because the amplitude of the acoustic waves would be sensibly reduced by the spatial average induced by the large active area of the sensor.

According to theoretical expectations, the pressure generated by the minimally invasive emitter should be larger than that generated by using the larger device. As seen by the simulations, actually, the temperature peak due to optical absorption in carbon is strongly dependent on the intensity I_0 of the laser source. As a consequence of that, the use of a smaller fiber should assure a higher optical power per unit area, provided that the same

amount of laser power is driven into the fiber. However, the coupling system from the laser beam to the optical fiber, usually realized by an optical coupler, is quite delicate and can lead to a remarkable reduction of the power transmitted to the fiber when smaller core sizes are utilized. This could explain the observed discrepancy between theory and experiments in the characterized device.

The acoustic wave measured at roughly 4 mm from the source and its Fast Fourier transform are reported in Figs. 4.23 and 4.24 respectively. As can be seen, the PVDF sensor presents a cutoff frequency that does not allow appreciating the actual bandwidth of the generated signal. In fact, if this spectrum is compared to the one calculated from the measured signal obtained with the membrane hydrophone (for the 700 μm large emitter), the damping of the high frequency components is evident. This should be due to the low sensitivity of the sensor employed at such frequencies and most probably not imputable to the bandwidth of the laser generated ultrasounds.
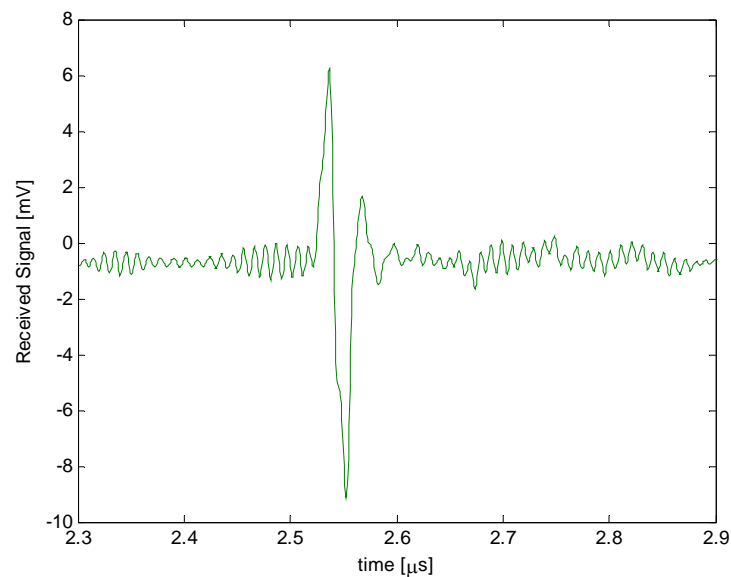
Fig. 4.23. Acoustic wave acquired at 4 mm far from the MOMS emitter
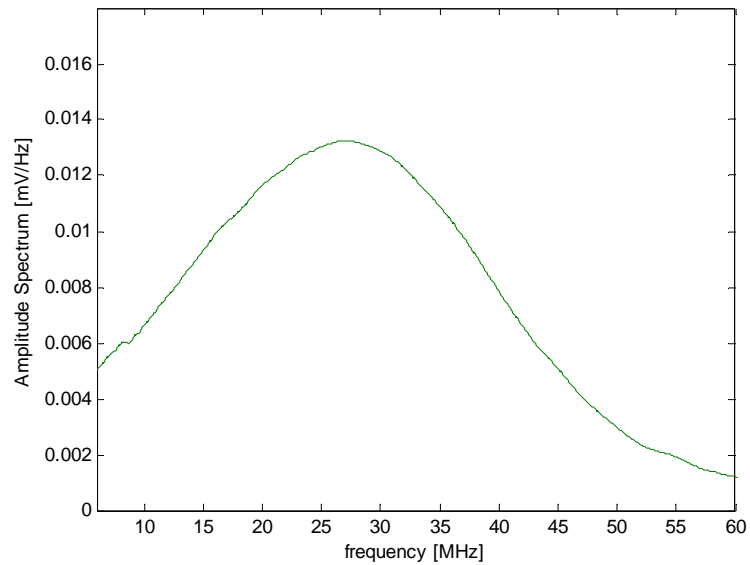
Fig. 4.24. Amplitude Spectrum of the voltage signal acquired at 4 mm from the MOMS emitter

The accurate derivation of the acoustic pressure from the measurements requires the use of the PVDF sensor sensitivity as a function of frequency, as reported below:

$$p(t) = \mathfrak{F}^{-1}\left\{\frac{V(f)}{S(f)}\right\}$$

where *V(f)* is the Fourier transform of voltage signal measured, *S* the sensitivity of the sensor and $\mathfrak{F}^{-1}$ the inverse Fourier transform. The needle PVDF hydrophone frequency response is shown in Fig. 4.25.
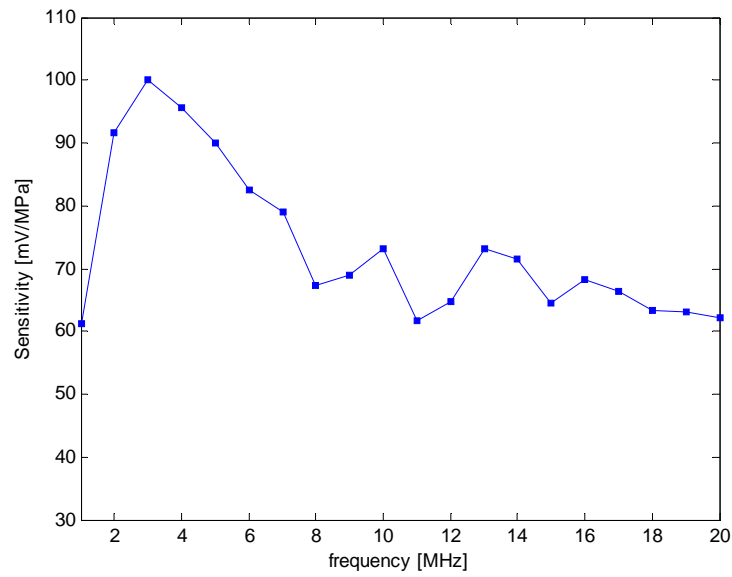
Fig. 4.25. Frequency response of the needle PVDF hydrophone (SN 1614), including the preamplifier stage

The acoustic pressure, calculated by fast FFT algorithm can be finally plotted (Fig. 4.26). In this procedure, the unknown high frequency sensitivity was considered equal to the last value provided by the sensor data sheet, most probably leading to a considerable estimation error.
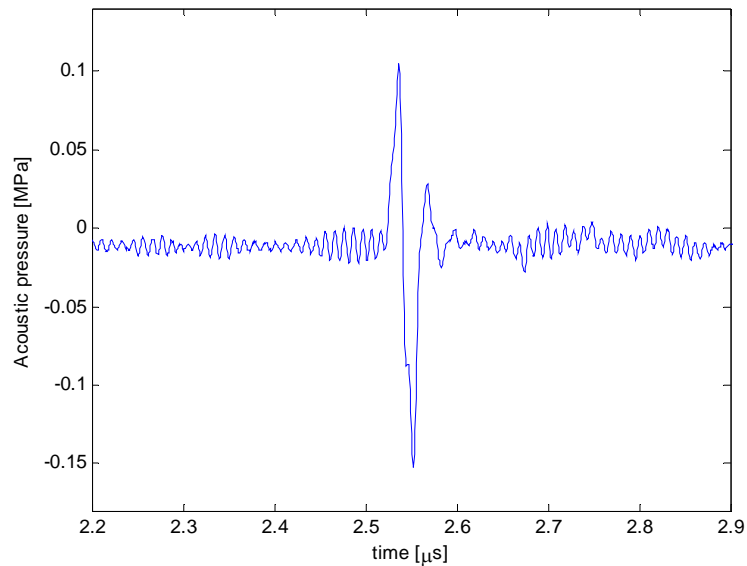
Fig. 4.26. Acoustic wave generated by the highly miniaturized emitter (250 kPa peak-to-peak amplitude)

133

In order to complete this preliminary characterization, the acoustic field generated by thermoelastic effect should be detected by the Fabry-Perot interferometer, in order to measure the real bandwidth of the signals emitted and received by the MOMS-based acoustic probes and further investigate the advantages and possible drawbacks of the developed technology. Such investigation was not possible in the framework of this thesis for the lack of a measurements setup suited to this particular measurements, and had to be delayed to future developments.

Conclusions

5

A Micro-opto-mechanical systems (MOMS) based technology for the fabrication of ultrasonic probes on optical fiber has been presented in this thesis. Thanks to the high miniaturization level reached, the realization of an ultrasonic system constituted by ultrasonic generating and detecting elements, suitable for minimally invasive applications or Non Destructive Evaluation (NDE) of materials at high resolution, has been demonstrated. The ultrasonic generation has been realized by irradiating a highly absorbing carbon film patterned on silicon micromachined structures with a nanosecond pulsed laser source, generating a mechanical shock wave due to the thermal expansion of the film induced by optical energy conversion into heat. The short duration of the pulsed laser, together with an appropriate emitter design, assure high frequency and wide band ultrasonic generation. The acoustic detection has been also realized on a MOMS device using an interferometric receiver, fabricated with a Fabry-Perot optical cavity realized by means of a patterned SU-8 and two Al metallization levels. In order to detect the ultrasonic waves, the cavity has been interrogated by a laser beam measuring the reflected power with a photodiode.

Various issues related to the design and fabrication of these acoustic probes have been investigated in this thesis. First, theoretical models have been developed to characterize the opto-acoustic behavior of the devices and estimate their expected acoustic performances. Tests structures have been realized to derive the relevant physical parameters of the materials constituting the MOMS devices and determine the conditions theoretically assuring the best acoustic emission and detection performances.

Moreover, by exploiting the models and the theoretical results, prototypes of acoustic probes have been designed and their fabrication process developed by means of an extended experimental activity. As a result of this work, self standing MOMS devices on optical fiber have been obtained with a minimum diameter smaller than 250 μm, matching the geometrical constraints required in minimally invasive applications. Thanks to the use of microfabrication techniques, arrays of detectors and receivers have also been realized on highly miniaturized MOMS devices with a good integration density. Different geometries have been considered and proper technological solutions have been assessed to permit the simultaneous fabrication of devices targeted for use with optical fibers with different size and allow the development of MOMS acoustic probes on both silicon and dielectric membranes, using a triple depth silicon Deep Reactive Ion Etching process. An acoustic sensitivity of 200 mV/MPa has been obtained using a MOMS interferometer interrogated with a 4mW laser source. The performances of the Fabry-Perot interferometers presented and their small size (with active sensor area smaller than 10 μm in diameter) make such devices suitable for high performance applications, overcoming the limitations of the piezoelectric transducers arrays in terms of trade-off between operation frequency and sensitivity and those of bulk optoacoustic systems related to miniaturization.

Concerning emitters, a pressure of 1 MPa amplitude and bandwidth extended beyond 50 MHz has been measured by a membrane hydrophone at a distance of 2 mm from a MOMS emitter with diameter of 700 μm and obtained on a 100 μm thick silicon membrane, mounted on a 630 μm multimode fiber. A pressure of 250 kPa has been instead detected at a distance of 4 mm from a 300 μm emitter operated on a 230 μm multimode fiber, but using a needle PVDF hydrophone with lower cutoff frequency and with an imperfect coupling between the laser beam and the fiber.

Acknowledgments